DIEDERIK J. GROOTENDORST

DETECTION OF LYMPH NODE METASTASES BY PHOTOACOUSTIC IMAGING

DETECTION OF LYMPH NODE METASTASES BY PHOTOACOUSTIC IMAGING

DIEDERIK JOHANNES GROOTENDORST

Thesis committee members:

Prof. dr.	Gerard van der Steenhoven	University of Twente (Chairman)
Prof. dr.	Theo J.M. Ruers	University of Twente (Promotor)
Prof. dr.	Wiendelt Steenbergen	University of Twente (Promotor)
Dr.	Srirang Manohar	University of Twente (Assistant-Promotor)
Prof. dr.	Ivo Broeders	University of Twente
Prof. dr.	Ton van Leeuwen	University of Twente / AMC
Prof. dr.	Martin Frenz	University of Bern
Dr.	Bennie ten Haken	University of Twente
Dr.	Joost Klaase	Medisch Spectrum Twente

The work described in this thesis was performed at the Biomedical Photonic Imaging (BMPI) Group, MIRA institute for Biomedical Technology and Technical Medicine, Faculty of Science and Technology, University of Twente, P.O. box 217, 7500 AE, Enschede, and The Netherlands Cancer Institute – Antoni van Leeuwenhoek (NKI-AVL), Surgical Oncology, Plesmanlaan 121, 1066 CX, Amsterdam.

This research is funded by the MIRA Institute for Biomedical Technology and Technical Medicine of the University of Twente. We thank the Stichting van Kampen Wassenaar for their financial support of the clinical melanoma studies.

ISBN: 978-90-365-3510-6
DOI: 10.3990/1.9789036535106

Author email address: d.j.grootendorst@gmail.com

DETECTION OF LYMPH NODE METASTASES BY PHOTOACOUSTIC IMAGING

DISSERTATION

to obtain
the degree of doctor at the University of Twente,
on the authority of the rector magnificus,
Prof. dr. H. Brinksma,
on account of the decision of the graduation committee,
to be publicly defended
on Wednesday the 17th of April 2013 at 16.45

by

Diederik Johannes Grootendorst

Born on the 1st of October, 1985
In Amsterdam, The Netherlands

This thesis has been approved by:

Prof. dr.	Theo J.M. Ruers	(promotor)
Prof. dr.	Wiendelt Steenbergen	(promotor)
Dr.	Srirang Manohar	(assistant-promotor)

TO MY MOTHER

CONTENTS

SUMMARY

SAMENVATTING

1. **CHAPTER 1**: OPTICAL TECHNIQUES FOR THE INTRA-OPERATIVE ASSESSMENT OF NODAL STATUS 1
   - 1.1. INTRODUCTION 2
   - 1.2. OPTICAL COHERENCE TOMOGRAPHY 5
   - 1.3. ELASTIC SCATTERING SPECTROSCOPY 6
   - 1.4. FOURIER TRANSFORM INFRARED SPECTROSCOPY 8
   - 1.5. DIFFUSE REFLECTANCE SPECTROSCOPY 9
   - 1.6. RAMAN SPECTROSCOPY 10
   - 1.7. NEAR INFRARED FLUORESCENCE IMAGING 12
   - 1.8. PHOTOACOUSTIC IMAGING 14
   - 1.9. FUTURE PERSPECTIVE 16
   - 1.10. REFERENCES 18

   AIM OF RESEARCH 24

2. **CHAPTER 2:** INITIAL RESULTS OF IMAGING MELANOMA METASTASIS IN RESECTED HUMAN LYMPH NODES USING PHOTOACOUSTIC COMPUTED TOMOGRAPHY 25
   - 2.1. INTRODUCTION 26
   - 2.2. MATERIALS AND METHODS 28
   - 2.3. RESULTS AND DISCUSSION 29
   - 2.4. SUMMARY 31
   - 2.5. REFERENCES 32

3. **CHAPTER 3:** FIRST EXPERIENCES OF PHOTOACOUSTIC IMAGING FOR DETECTION OF MELANOMA METASTASES IN RESECTED HUMAN LYMPH NODES
   - 3.1. INTRODUCTION 36
   - 3.2. MATERIALS AND METHODS 37
     - 3.2.1. RESEARCH PROTOCOL 37
     - 3.2.2. SETUP 38
     - 3.2.3. IMAGING 38
   - 3.3 RESULTS 39
     - 3.3.1. IMAGING MALIGNANT LYMPH NODES 39
     - 3.3.2. IMAGING BENIGN LYMPH NODES 43
     - 3.3.3. MULTISPECTRAL ANALYSIS 44
   - 3.4. DISCUSSION AND CONCLUSIONS 46
   - 3.5. REFERENCES 48

4. **CHAPTER 4:** EVALUATION OF SUPERPARAMAGNETIC IRON OXIDE NANOPARTICLES (ENDOREM®) AS A PHOTOACOUSTIC CONTRAST AGENT FOR INTRA-OPERATIVE NODAL STAGING 51
   4.1. INTRODUCTION 52
   4.2. MATERIALS AND METHODS 53
      4.2.1. IRON OXIDE NANOPARTICLES..... 53
      4.2.2. ANIMALS..... 54
      4.2.3. PA IMAGING 55
      4.2.4. MAGNETIC RESONANCE IMAGING 56
      4.2.5. VIBRATING SAMPLE MAGNETOMETRY 57
      4.2.6. OPTICAL PROPERTY ESTIMATION 57
      4.2.7. HISTOLOGY 58
   4.3 RESULTS 58
   4.4. DISCUSSION AND CONCLUSIONS 61
   4.5. CONCLUSION 64
   4.6. REFERENCES 65

5. **CHAPTER 5:** INTRA-OPERATIVE EX VIVO PHOTOACOUSTIC NODAL STAGING IN A RAT MODEL USING A CLINICAL SUPERPARAMAGNETIC IRON OXIDE NANOPARTICLE DISPERSION 69
   5.1. INTRODUCTION 70
   5.2. MATERIALS AND METHODS 72
      5.2.1. ANIMAL MODEL AND TUMOR CELL LINE 72
      5.2.2. PHOTOACOUSTIC IMAGING SETUP 74
      5.2.3. MAGNETIC RESONANCE IMAGING 75
      5.2.4. CONTRAST QUANTIFICATION 76
   5.3 RESULTS 76
   5.4. DISCUSSION 82
   5.5. CONCLUSION 85
   5.6. REFERENCES 85

6. **CHAPTER 6:** APPLICATION OF CARBON NANOPARTICLES FOR PHOTOACOUSTIC DETECTION OF LYMPH NODE METASTASES..... 89
   6.1. INTRODUCTION 90
   6.2. MATERIALS AND METHODS 92
      6.2.1. ANIMAL PROTOCOL 92
      6.2.2. PHOTOACOUSTIC IMAGING 92
   6.3 RESULTS 93
   6.4. DISCUSSION 97
   6.5. CONCLUSIONS 99
   6.6. REFERENCES 99

7. **CHAPTER 7:** COMPARISON BETWEEN I*N VIVO, IN TOTO* AND *EX VIVO* PHOTOACOUSTIC DETECTION OF NODAL METASTASES USING A NEW CLINICAL GRADE SPIO DISPERSION (SIENNA+) 103
7.1. INTRODUCTION 105
7.2. MATERIALS AND METHODS 106
7.2.1. RESEARCH PROTOCOL 106
7.2.2. ADDITIONAL ANALYSIS 107
7.2.3. PHOTOACOUSTIC SETUP 108
7.2.4. PHOTOACOUSTIC IMAGING 108
7.3 RESULTS 108
7.4. DISCUSSION AND CONCLUSIONS 114
7.5 REFERENCES 117

8. **CHAPTER 8:** CONCLUSIONS AND OUTLOOK 119

ACKNOWLEDGEMENTS

ABOUT THE AUTHOR

LIST OF PUBLICATIONS

SUMMARY

This thesis describes the development of fast and non-destructive methods to detect lymph node metastases intra-operatively using photoacoustic (PA) imaging. The work can grossly be divided into two different approaches of which one is aimed at the differentiation between benign and metastatic nodes using endogeneous chromophores where the other makes use of the exogenenous contrast of iron oxide nanoparticles for differentiation.

Chapter 1 provides an overview of the application of different optical techniques to enable lymph node staging during surgical resection. The disadvantages of conventional medical imaging techniques are being discussed including their low sensitivity and poor intra-operative applicability. We present several optical techniques capable of nodal staging and discuss their limitations and future potential. Next to purely optical techniques like optical coherence tomography (OCT) and reflectance spectroscopy, we summarize the progress that has been made with PA imaging in this field and discuss its main advantages.

Our initial verification of the possibility to detect melanoma cells in lymph nodes is discussed in **Chapter 2**. A pig lymph node containing different concentrations of melanoma cells is photoacoustically imaged and the outline of the melanoma lesion can be accurately traced within the nodal volume. In addition, PA imaging of a resected human lymph node containing metastatic melanoma cells displays an increased intensity at locations were viable melanoma cells can be found according to histology. Our results suggest that PA has the potential to develop into an intra-operative imaging method to detect melanoma metastases in (sentinel) lymph nodes.

The continuation of this work is discussed in **Chapter 3**, where we evaluated the PA imaging results from a larger amount of resected lymph nodes from melanoma patients both benign and metastatic lymph nodes. Next to single wavelength imaging we also image the nodes using multiple excitation wavelengths. We demonstrate that the metastatic nodes showed a higher PA response and responded differently to an increase in excitation wavelength than benign nodes. In addition, differences in anatomical features between the two groups could also be detected. However, it remained preliminary to designate a highly accurate parameter to distinguish between malignant and benign nodes, mainly because blood related absorption also induces high PA responses in benign lymph nodes.

The absence of production of endogenous chromophores in many other malignancies spreading to the lymphatics, limits the applicability of the approach discussed in Chapter 1-

4 to the detection of melanoma metastases. In order to intra-operatively stage lymph nodes which are possibly affected by metastases related to other primary tumour types, we look into the applicability of superparamagnetic iron oxide (SPIO) nanoparticles in **Chapter 4.** We show that subcutaneous injection of SPIOs in healthy rodents primarily leads to uptake of the particles in the peripheral sinusoidal zone of the popliteal lymph nodes. PA imaging of the resected nodes display ring-like contrast patterns corresponding with iron deposition in this zone which is in accordance with the results from MRI and histology. The distribution of the particles could still be accurately mapped at SPIO amounts as low as ± 11 µg. Results indicate that PA imaging is able to map the SPIO distribution within lymph nodes with an accuracy which could enable the detection of metastasis once they influence this distribution.

Chapter 5 therefore focuses on the distinctive potential of SPIO nanoparticles for staging of resected lymph nodes obtained from a metastatic animal model. PA images of both metastatic and benign lymph nodes show that lymph nodes containing metastases display a heterogeneous SPIO distribution with absence of SPIOs at several locations within the peripheral zone. In benign lymph nodes on the other hand the SPIOs are homogeneously distributed and a higher PA response is measured throughout the nodes. Results correlate with those of MRI and immunohistochemistry which demonstrates that accurate intra-operative nodal staging after subcutenous SPIO injection is feasible.

In order to decrease the costs of the nanoparticle agent while increasing its PA response, lymph node staging with the help of carbon nanoparticles is investigated in **Chapter 6**. It is shown that the same PA differences between resected benign and metastatic nodes can be detected as with the SPIO particles, both with the tomographic PA system as the hand-held commercial system. In addition, PA response seems to be higher although a distinction between metastatic and benign lymph nodes within the animal remains challenging. We conclude that carbon nanoparticles like SPIOs could facilitate nodal staging, however its *in vivo* potential still requires further investigation.

To conclude our investigations we look into the *in vivo* potential of a newly available SPIO dispersion in **Chapter 7** and compare the results with PA distribution maps obtained within non-living animals and *ex vivo* animal lymph nodes. Successful staging of lymph nodes is prevented because of the PA influence of nearby vessels obfuscating the low PA signal produced by the SPIO nanoparticles. Comparison with *ex vivo* lymph nodes shows that a distinction between benign and malignant nodes can again be made once the nodes are resected.

In **Chapter 8** the conclusion of the thesis is discussed and an outlook is given with respect to future work.

SAMENVATTING

Dit proefschrift beschrijft de ontwikkeling van een techniek waarmee lymfeklier metastasen snel en zonder weefselschade kunnen worden opgespoord gedurende een chirurgische ingreep, met behulp van fotoakoestiek (FA). Het proefschrift kan worden ingedeeld aan de hand van twee verschillende benaderingen. De eerste betreft een onderscheid tussen goedaardige en gemetastaseerde lymfeklieren op basis van een natuurlijk aanwezig kleurstof, de andere op basis van een contrastmiddel bestaande uit ijzer oxide nanodeeltjes.

Hoofdstuk 1 geeft een overzicht van de verschillende optische technieken die worden ontwikkeld om lymfeklieren te kunnen stadiëren tijdens een chirurgische ingreep. De nadelen van conventionele medische afbeeldingstechnieken worden besproken, waaronder een lage sensitiviteit en een verminderende toepasbaarheid binnen de operatiekamer. Daarnaast brengen we verschillende optische technieken naar voren die hier verbetering in zouden kunnen aanbrengen en bediscussiëren hun beperkingen. Naast technieken als optische coherentie tomografie (OCT) en Raman spectroscopie, vatten we de ontwikkeling binnen het fotoakoestische werkveld samen en beschrijven de belangrijkste voordelen van deze techniek.

De resultaten van onze initiële experimenten om melanoom cellen in lymfeklieren aan te tonen worden beschreven in **Hoofdstuk 2**. Een varkens lymfeklier met daarin verschillende concentraties melanoomcellen beelden we fotoakoestisch af en we tonen aan dat melanoom laesies goed te traceren zijn met deze techniek. Daarnaast, laten afbeeldingen van een menselijke lymfeklier zien dat locaties die correleren met de aanwezigheid van melanoomcellen een verhoogde signaal intensiteit bevatten. Deze resultaten suggereren dat FA mogelijk verder ontwikkeld kan worden om melanoom metastasen in (schildwacht) klieren gedurende de operatie te visualiseren.

We continueren dit werk in **Hoofdstuk 3**, waar we de fotoakoestische resultaten bespreken van een grotere groep humane lymfeklieren. In deze groep zijn zowel gezonde als gemetastaseerde lymfeklieren opgenomen. Naast beeldvorming met behulp van een enkele golflengte maken we hier ook gebruik van meerdere golflengtes om de klieren te scannen. We laten zien dat gemetastaseerde klieren een hoger FA signaal geven en daarnaast anders reageren als ze belicht worden met laserlicht dat hogere golflengten bevat. Tot slot definiëren we anatomische variaties die de FA afbeeldingen laten zien tussen de twee lymfeklier groepen. Ondanks deze bevindingen blijken we nog niet in staat één specifieke parameter te definiëren waarmee gezonde van gemetastaseerde klieren kunnen worden

onderscheiden. Dit blijkt voornamelijk te komen doordat de optische absorptie van bloed gerelateerde componenten ook zorgt voor hoge FA signalen.

De afwezigheid van natuurlijk kleurstoffen in vele andere lymfatische metastaserende tumoren beperkt de toepasbaarheid van de techniek die we besproken hebben in de Hoofdstukken 1-4 tot de detectie van melanoom metastasen. Om dit te ondervangen en de techniek ook te kunnen gebruiken voor de inter-operatieve stadiering van andere tumor typen, onderzoeken we de toepasbaarheid van super paramagnetische ijzeroxide (SPIO) nanodeeltjes in **Hoofdstuk 4**. We tonen aan dat een subcutane injectie van SPIO nanodeeltjes in de achterpoot van gezonde ratten leidt tot opname van deze deeltjes in het perifere sinusoidale gebied van de popliteale klieren. Fotoakoestische beeldvorming van deze klieren laat ring-vormige contrast partronen zien wat wijst op ijzer depositie in deze gebieden. Dit bevestigen we met behulp van MRI en (immuno)histopathologie. De distributie van de nanodeeltjes kan accuraat worden weergegeven met FA tot een SPIO hoeveelheid van ± 11 µg. Deze resultaten laten zien dat FA in staat is om de distributie van SPIO nanodeeltjes in lymfeklieren accuraat weer te geven, wat mogelijk gebruikt zou kunnen worden om de aanwezigheid van metastasen aan te tonen.

Hoofdstuk 5 gaat daarom dieper in op het vermogen van deze SPIO nanodeeltjes om onderscheid te maken tussen gezonde en gemetastaseerde lymfeklieren. Hiervoor maken we gebruik van een tumor diermodel. De FA afbeeldingen laten zien dat onder invloed van metastasen de SPIO nanodeeltjes distributie veranderd van homogeen naar heterogeen, waarbij er sprake is van de afwezigheid van contrast op verschillende locaties binnen de perifere zone. Daarnaast verminderd de intensiteit van het FA signaal. Deze bevindingen correleren met die van MRI en immunohistopathologie. Hieruit kan worden geconcludeerd dat fotoakoestische stadiering van lymfeklieren met behulp van subcutane injectie van SPIO nanodeeltjes mogelijk ook toegepast kan worden op andere maligniteiten.

Om de kosten van het gebruik van nanodeeltjes verder te verlagen en tegelijkertijd de fotoakoestische signaal opbrengst te verhogen, onderzoeken we in **Hoofdstuk 6** de toepassing van koolstof nanodeeltjes. We bewijzen dat deze deeltjes op een vergelijkbare manier onderscheid kunnen maken tussen gezonde en gemetastaseerde lymfeklieren, zowel door afbeeldingen te vergaren met een tomografisch als met een hand-held FA systeem. Bovendien lijkt de FA signaal opbrengst inderdaad hoger te liggen. Zolang afbeeldingen van de lymfeklieren worden gemaakt door de huid heen blijkt het onderscheid tussen gezonde en gemetastaseerde klieren echter moeilijker te maken. Uit deze gegevens concluderen wij dat koolstof nanodeeltjes, net als SPIOs, de stadiëring van lymfeklieren zouden kunnen vergemakkelijken, hoewel het gebruik van de deeltjes *in vivo* nog verder onderzoek verreist.

Tot slot hebben we in **Hoofdstuk 7** nader onderzoek gedaan naar de mogelijkheden van het gebruik van SPIO nanodeeltjes *in vivo*. Deze resultaten hebben we vervolgens vergeleken

met FA afbeeldingen van intacte maar overleden dieren en uitgesneden *ex vivo* klieren. *In vivo* stadiering blijkt bemoeilijkt te worden door FA invloeden van nabij gelegen bloedvaten welke het lagere signaal afkomstig van SPIO nanodeeltjes overschaduwen. Een vergelijking met de *ex vivo* klieren laat zien dat onderscheid tussen gezonde en metastase bevattende klieren wel weer gemaakt kan worden als deze klieren worden uitgesneden.

In **Hoofdstuk 8** trekken we algemene conclusies over de gehele thesis en schetsen we een vooruitzicht voor de toekomst.

CHAPTER 1

OPTICAL TECHNIQUES FOR THE INTRA-OPERATIVE ASSESSMENT OF NODAL STATUS*

The lymphatic system is an important pathway in the metastatic spread of many malignancies and a key prognostic indicator. Non-destructive assessment of the nodal status during surgery could limit the amount of lymph nodes to be resected and allow for immediate regional lymphadenectomy during sentinel lymph node biopsy procedures. We look into the possibilities of conventional medical imaging methods capable of intra-operative nodal assessment and discuss multiple newly developed optical techniques. The physical background behind these techniques is reviewed and a concise overview of their main advantages and disadvantages is produced. These recent innovations show that while the application of optical modalities for intra-operative nodal staging is not yet applied routinely, there is reason enough to expect their introduction in the near future.

* This chapter has been communicated as: D. J. Grootendorst, W. Steenbergen, S. Manohar, T. J. M. Ruers, "Optical techniques for the intra-operative assessment of nodal status " to Future Oncology.

1.1 Introduction

The lymphatic system is an important pathway in the metastatic spread of many malignancies. The presence of metastatic deposits in lymph nodes determines both the prognosis and therapeutic regimen of individual patients. Research has shown that lymph node involvement is one of the most prognostic indicators for a variety of cancer types such as invasive breast carcinoma (1), malignant melanoma (2) and prostate carcinoma (3), hence its inclusion in the international staging system.

For the lymphatic spread of most malignancies it is presumed that metastatic cells initially travel to the lymph node(s) primarily draining the area in which the primary tumor is located. These first draining lymph nodes are the so called Sentinel Lymph Nodes (SLN) and accurate analysis of their content provides a clear indication of lymphatic involvement. The introduction of the Sentinel Lymph Node Biopsy (SLNB) was therefore able to limit the amount of lymph nodes to be removed and reduce the invasiveness of the procedure (4), provided that metastatic involvement was verified by both conventional histology and immunohistochemistry. Identification of the so called ''sentinel'' nodes is done by lymphoscintigraphy and/or blue dye injection after which the resected nodes have to be fixated, sectioned, stained and reviewed by an expert pathologist. The sectioning and staining procedure of the SLN is known to vary between clinical centers but generally takes up several days (5). Although the therapeutic benefit of the procedure is not universally accepted with regard to an improvement of overall long term survival (6), SLNB is nowadays routinely performed for breast malignancies and malignant melanomas. Once metastatic involvement of the lymphatic system has been verified by SLNB, further resection of the local lymph node basin is generally considered.

Next to mentioned advantages of the SLNB, especially the reduction of post-operative morbidity, the procedure still contains a significant disadvantage with regard to direct nodal assessment. Due to the required histopathological assessment, accurate diagnostic information is not available during surgery, so no treatment decision can be made while the SLNB is performed. Therefore, the patient needs to return for a second surgical procedure once the pathology results require the removal of additional nodes. Beside serious patient discomfort, the present logistic process results in additional costs that are estimated to be around £1368 per patient (7). In addition, as it is known that the total number of positive lymph nodes detected during additional lymphadenectomy has a prognostic significance (8), real-time assessment of the lymph nodes could limit of the amount of lymph nodes removed. This would decrease the chance of lymphedema development after regional lymphadenectomy, while additional therapy can be initiated faster because diagnosis would be available during surgery.

So, an imaging technique capable of assessing lymph node status during surgery inside the operation room (OR) could not only improve decision making related to the SNB procedure, but could also significantly limit the morbidity of lymphadenctomy procedures.

Non-destructive imaging would have the additional advantage that tissue would still be available for histological analysis after surgery and no extensive preparation has to be performed in the OR. To provide a solution for this problem, frozen section analysis (FSA) was introduced in the early 20th century and found to be logistically helpful in an intra-operative setting. However, its low sensitivity for detecting metastases in especially melanoma patients (47%) has labeled the technique unsuitable for sentinel lymph node analysis (9). The more recently introduced, intra-operative touch preparation cytology (IOTPC) or "imprint cytology" which requires the imprinting of fresh tissue on a thin glass plate after which microscopic examination can commence, has shown comparable low sensitivity results for melanoma patients (33%) (10). In addition this techniques requires an expert cytopathologist to be present during the surgical procedure to obtain intra-operative diagnostic results which is time consuming and expensive.

Next to these techniques, conventional medical imaging techniques, including ultrasound, positron emission tomography (PET) and Magnetic Resonance Imaging (MRI) have been analyzed with respect to their nodal staging capabilities pre-operatively. These results give some indication of their applicability during surgery. For ultrasound for example, highly variable accuracy rates across clinical studies and types of malignancies are reported (11,12). However, most larger clinical studies for malignant melanoma and breast malignancies show a relatively low sensitivity (25-60%) combined with a higher specificity (70-100%) . This low sensitivity of ultrasound can be explained by the fact that the median cross-sectional area of metastatic deposits may be as small as 0.39 mm^2 (12). Such small metastases are not expected to produce physical changes within the node which can be visualized using ultrasound. Therefore, such small deposits may remain below the detection limit of the technique even with the introduction of higher frequency transducers.

A variable accuracy is also noted in several clinical studies for lymph nodes staging by fludeoxyglucose-PET (FDG-PET). Best quality studies showed a sensitivity and specificity of around 80%, whereas in the poorer quality studies, the diagnostic accuracy was higher. In a recent meta-analysis of 25 studies related to breast cancer (13), an overall sensitivity of 37 to 85% was noted, together with a specificity of 84 to 100%. It was stated that the sensitivity of PET is not sufficient to detect small metastatic deposits. A meta-analysis with respect to lymph node staging for melanoma revealed a sensitivity of 87% together with a specificity of 98% (14) . Overall the sensitivity and specificity of FDG-PET is comparable to that of ultrasound due to their poor spatial resolution and/or low target-to-background signal unless it is combined with additional methods like MRI or CT.

The accuracy of pre-operative nodal staging using MRI is mainly dependent on whether a contrast agent is being applied. Contrast enhanced MRI studies show sensitivities ranging from 63 to 100% and specificities of 56% to 100% (15) which overall are higher than those reported in unenhanced studies. Again the cases in which metastases are missed involve the small metastatic lesions which are only detected after extensive histopathological analysis.

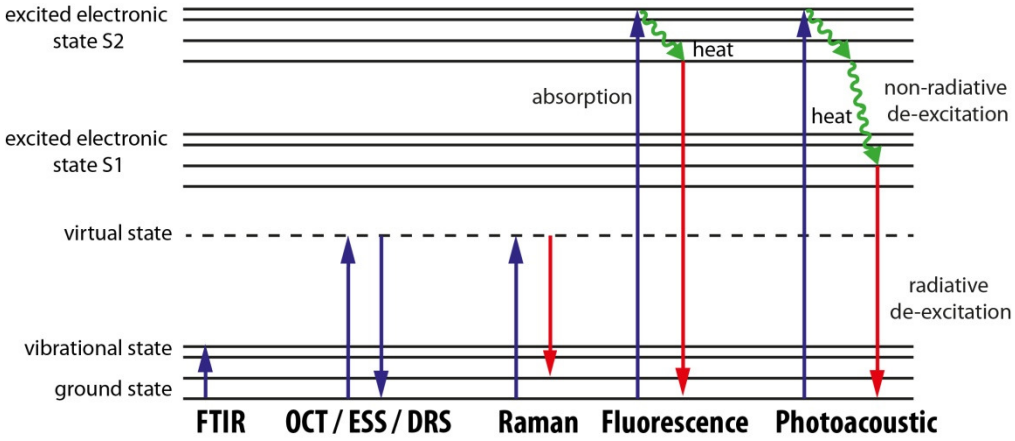

Fig. 1. Jablonski diagram of the physical principles behind different optical techniques

In general, clinical evaluations of these conventional medical imaging technologies still reveal serious limitations regarding the sensitivity and therefore ability of detecting smaller metastastic deposits. Other disadvantages, inherent to these techniques, like the size of the equipment, radiation or the presence of a magnetic field, can also be taken into account. Although the technical evolution of these techniques will most certainly improve their accuracy, the recent lack of sensitivity also leaves room for techniques which are better suited for the visualization of smaller structures. This is where optical modalities might play an important role in the near future.

The advantages of optical imaging compared with other imaging modalities include high resolution, high instrument sensitivity, high instrument mobility and fast imaging capabilities enabling real-time acquisition of functional information. In the following sections we will review various optical imaging modalities which are less frequently applied in a clinical setting but show the potential for improving nodal staging in an intra-operative setting. The fact that these techniques are able to base their analyses on freshly resected samples or easy to acquire tissue sections makes them especially compatible with the limited time available during surgery. In addition, most optical modalities do not have excessive space requirements and are compatible with an operation theatre full of metal instruments and electronic equipment. Given the recent international research interest regarding this topic, it could well be that some of these techniques find their way to the operation theatre very soon.

1.2 Optical Coherence Tomography

The main physical process behind Optical Coherence Tomography (OCT) is comparable with that of ultrasound, although OCT is based in light instead of sound, namely the reflection of incident waves. The physical principle behind this so called back scattering is

schematically displayed in Figure 1. Optical reflection within tissue occurs when the index mismatch between two tissue types is increased, the higher the mismatch the larger the amount of backscattered photons. However, most of the light scatters and only a tiny portion of the incident light reflects from subsurface features. This reflected portion travels back and interacts with the original broadband light source which results in either intensification or diminishing of the intensity depending on the optical interaction of the sample (16). Via this principle depth sensitive optical reflection can be measured, providing spatial information about the tissue microstructure (17).

Current OCT modalities are able to obtain axial resolutions ranging from 1 to 15 µm which is almost 10 times better than clinical ultrasound, making the detection of smaller metastatic deposits possible. All systems employ optical powers well below the maximum safety level while reflected signals as small as 10^{-10} of the incident light power can be detected with help of optical heterodyne detection (19). To permit the intra-operative staging of lymph nodes, it is of vital importance that imaging can be performed within a time period of several minutes. Recent reports regarding lymph node assessment with OCT, show an image capture time of 0.4 s per cross-sectional scan resulting in an acquisition time of 160 seconds for a 3-D OCT data set containing 300 images (18). The physical disadvantage of OCT, as for many optical techniques, lies in the relatively shallow penetration depth of around 2-3 mm depending on the tissue (20) which impedes the visualization of the entire nodal specimen. However, by miniaturizing and encasing the OCT probe in a medical needle as suggested by Iftimia *et al* (21), the complete nodal volume could be probed. Such an approach

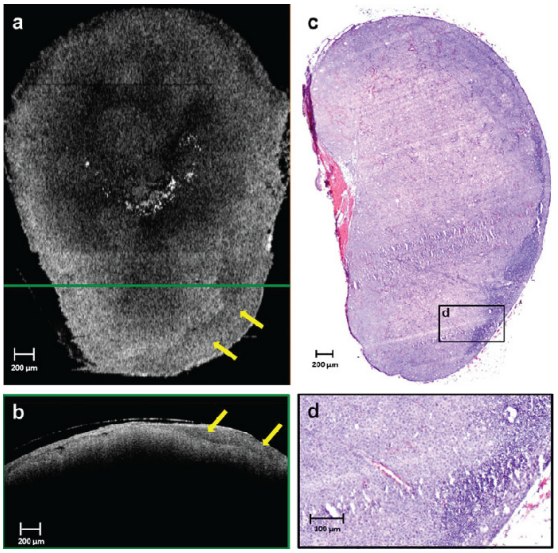

Fig. 2. A rat lymph node imaged after 9 days of tumor inoculation. OCT reveals a relatively homogeneous scattering pattern across the lymph node in both x-y (**a**) and x-z planar (**b**) images, due to near-total effacement of normal nodal architecture, as shown in the corresponding histological section in (**c**). A thick low-scattering layer in the capsular and subcapsular region (yellow arrows) can be seen in the x-y (**a**) and x-z planar (**b**) OCT images, resulting from metastatic tumor invasion. This correlates with regions in the histology that show only few remaining lymphocytes in the node (**d**). The green-framed x-z planar OCT image in (**b**) was extracted from the location of the horizontal green line shown on the x-y planar image in (**a**). The magnified histological region in (d) is from the blackframed region in (**c**). *Reproduced from (18) with kind permission from Springer Science and Business.*

remains however limited to a certain amount of probed locations within the intra-operative time span, losing some sensitivity especially if micro-metastastes are involved.
Possible application of OCT for nodal screening was initially investigated by *in vivo* and *in vitro* lymph node scanning in six Sprague-Dawley rats injected with *N*-methyl-*N*-nitrosourea. It was verified that the 3-D nodal structure could be displayed with an axial resolution of 2 µm. In addition, internal structures could be identified including the lymphoid follicles, the cortex, the capsule, and the medullary sinuses (22).
In 2010, McLaughlin *et al* (23) used OCT for depicting the morphology of thirty human lymph nodes and distinguishing lower backscattering cortical areas from highly backscattering tumor-permeated tissue. However, because appearance within the OCT image varies with depth, healthy and malignant tissue varied in appearance depending on location. To compensate for this phenomenon, an algorithm was designed to allocate the intensity of each pixel to the tissue's attenuation coefficient across a subset of the A-scans. OCT Scans of the auxiliary lymph nodes of two breast cancer patients verified that such parametric images provided improved tissue contrast (24).
Recently, a study on ten MAT-B III inoculated Female Fischer F344 rats was performed to pinpoint optical biomarkers associated with various stages of metastastic involvement (18). Markers included uniform high-scattering regions due to disruption of normal lymph node structure (Fig. 2) and low scattering regions in the precortical regions due to the infiltration of metastatic cells and macrophages. Such markers could possibly function as an atlas for comparison with images acquired during surgical interventions in the future.

From these studies we can conclude that OCT imaging is able to produce a highly accurate map of the nodal morphology and capable of pinpointing biomarkers for metastatic involvement. However, clinical sensitivity and specificity ratios remain to be produced and its limited penetration depth might make it challenging to accurately map larger samples within a limited time span.

1.3 Elastic scattering spectroscopy

As mentioned in the introduction, imprint cytology is experimentally being employed for the examination of (sentinel) lymph nodes with varying results (25) . The method is quick and easy although an expert cytopathologist has to be present during the operation to provide the diagnostic results. In order to overcome this disadvantage while obtaining higher sensitivity ratios, research into the use of spectroscopic methods for automated analysis of the imprint sections has been initialized in recent years. One of these methods employs elastic scattering spectroscopy (ESS) for the real-time discrimination of benign and malignant tissue.

In contrast with for example fluorescence, ESS does not involve photon absorption and the atoms involved do not make a transition to an excited state before the scattering process takes place (27). Since the process is elastic and does not involve absorption, as schematically displayed in Figure 1 , the scattered light has the same frequency as the incident light. By measuring the magnitude, phase, and the angular- or wavelength-dependence of the scattered far field, one can retrieve information about the scattering (28). In this way the technique is sensitive to the sizes, indices of refraction, and structures of the

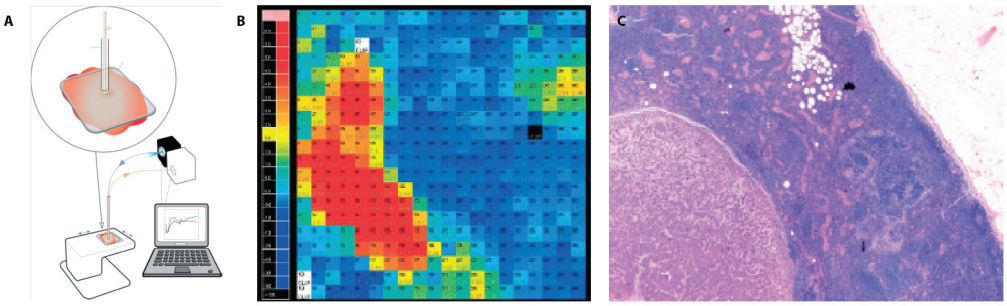

Fig. 3. A. Schematic diagram of elastic scattering spectroscopy (ESS) system. The node is scanned through a fibreoptic plate by moving it on a stage under a fixed probe. **B.** False colour-coded map of a node showing a single metastasis in the left lower quadrant. Colours are based on the canonical score for each pixel, obtained through principle component analysis and linear discriminant analysis of the ESS spectra, from blue (low score, indicates normal node) to red (high score, indicates metastasis). The cut-off chosen to discriminate between normal and cancer for individual pixels is where the colour changes from pale green to yellow. **C.** Histology image showing the junction of a metastasis (lower left) with normal lymphatic tissue (upper right) (haematoxylin and eosin stain, original magnification ×400). *Reproduced from (26) with kind permission of John Wiley & Sons, Ltd.*

subcellular components like, nucleus, nucleolus, and mitochondria that change with malignant transformation. Changes in wavelength dependent light scattering, resulting from malignant transformation, can be modeled using Mie theory (29,30) and finite-difference time domain methods (31). Multivariate statistical analysis can then be used to recognize patterns within these spectra. With appropriate diagnostic algorithms these spectra can then be used to discriminate between benign and malignant tissue within samples, no longer requiring the expertise of a cytopathologist. A general ESS setup requires relatively simple instrumentation including a pulsed xenon arc lamp, an optical probe, and a spectrometer (Fig. 3A). By scanning a probe with an input and output optical fiber over the tissue, spectroscopic data can be obtained within minutes. Despite these advantages, the limited sample volume of the fibers requires large samples, e.g. lymph nodes, to be scanned iteratively or at specific locations which could result in smaller metastases to be missed.

A study with regard to the detection of cervical intranodal metastasis in oral cancer was already published in 2003 (32), where ESS spectra were obtained from formalin fixed neck dissection specimens. These spectra were then compared at 4 different wavelengths: 360,

450, 630 and 690 nm. In 13 patients a sensitivity and specificity of respectively 98% and 68% was obtained. In 2004, a study on 139 freshly excised nodes showed a sensitivity of 84% and a specificity of 91% for ESS if the nodes were normal or completely replaced by breast cancer (33). The accuracy of the technique dropped to respectively 75% and 89% once the nodes contained smaller metastatic deposits which however still proved to be comparable to the accuracy of regular imprint cytology. In 2010, a raster scanning ESS setup was employed to obtain spectra from 128 intact sentinel lymph nodes of breast cancer patients and create a map of cancer risk across the nodal surface (Fig. 3B). Risk was classified by extracting spectral features using principal component analysis (PCA) and discriminating between classes by linear discriminant analysis (LDA). By projecting the spectral vector onto the axis of maximum discrimination, a canonical score was derived which could be used as a predictive measure. The freshly resected lymph node was fixated with an optical plate (Fig. 3A) which enabled the scanning of the entire nodal surface. The pixel risk maps were then converted into a metastatic probability for the node using a so called "clump counting" method which resulted in a sensitivity of 69% and a specificity of 96% (26,34). This rasterscan approach enabled the complete analysis of larger tissue samples thereby eliminating one of the major disadvantages of the technique. It has to be noted however, that this approach required up to 20-25 minutes to scan 1 cm^2.

Based on the results of these different studies, it can be concluded that ESS could offer a cost-effective solution for imprint cytology analysis, although a lot of computational modeling and training is required to generate a relative accurate risk score for a specific tissue type. In addition, the limited penetration depth impedes rapid analysis of the entire nodal specimen which could result in metastases to be missed.

1.4 Fourier transform Infrared spectroscopy

Fourier transform infrared spectroscopy (FTIR) can be used to detect vibration in chemical bonds and, as such, has been used to sense the biochemical composition of tissues (35). Functional groups can be associated with characteristic absorption of the incident infrared light, resulting in the presence of specific absorption peaks in the recorded spectrum coming out of the tissue. Although incapable of detecting specific molecules because many bond vibrations are shared among biomolecules, FTIR can be used to quantify classes of molecules (i.e. glycogen, protein, fat or nucleic acid) (36).

The technique possesses fast imaging potential and operates at a broad wavelength range of 250-2500 nm resulting in the possibility to scan samples with a regular FTIR setup up to a thickness of several µm's (37). A regular FTIR setup consists of an IR spectrophotometer, a white light source and a CCD camera which can be combined in a relatively small volume resulting in a handheld or tabletop design. The output and input fibers have to be placed in close proximity to the tissue to ensure the accurate acquisition of the spectra. Related to this, the relatively small sampling volume again proves to be one of the disadvantages,

although the greatest drawback lies in its inability to analyze fresh tissue. The strong absorption peak of water masks a major portion of the relevant chemical fingerprint in the tissue sample spectrum (38). This requires the samples to be sectioned and dried in some cases which takes up time and resources.

A study in 2011 comparing the FTIR spectra of 61 metastatic cervical lymph nodes with those of 123 non-metastatic nodes in the wavelength range of 2.5 µm to 10 µm revealed that the relative intensity ratios relating to protein and nucleic acid both increased in papillary thyroid carcinoma tissue while those of carbohydrates and lipids decreased, probably owing to the increased metabolism of the metastatic cells (39). Within the studied data a sensitivity of 80% and specificity of 92% was obtained for the detection of lymph node metastases. The authors claim no pre-treatment of the fresh tissue is required and sectioning of the samples only takes a maximum of 3 minutes. With regard to the analysis of touch imprint cytology data , FTIR imaging of lymph nodes in mid-IR range (800 to 2000 cm^{-1}) has also been employed. A pilot study in 2004 showed that without fixation or staining of the tissue, the absorption spectra of lymph nodes display strong lipid peaks and sufficient information is present to distinguish nodal tissue from thyroid tissue (40). The next step should confirm if such differences are also present between benign and malignant nodes.

We can conclude that FTIR might prove to be an inexpensive and accurate technique to perform intra-operative staging in the future due to its possibility to analyze biochemical composition. However, research on human nodal tissue is still limited and difficulties with regard to fresh tissue analysis might impede intra-operative applicability. Furthermore most systems still rely on point measurements and together with the limited optical penetration depth this significantly limits screening of larger tissue samples like lymph nodes.

1.5 Diffuse reflectance spectroscopy

Diffuse reflectance spectroscopy (DRS), utilizes visible-near infrared light to acquire information about the wavelength-dependent optical absorption and scattering to allow for an estimation of physiological tissue parameters. DRS relies mostly on elastic scattering as schematically displayed in Figure 1, however the reflectance spectrum is the resultant of both absorption and scattering. The intensity of reflected light after being scattered or absorbed as a function of the wavelength defines the reflectance spectrum and results from molecular differences between tissues. Changes in human tissue associated with malignant transformation include alterations in cellular composition, metabolic rate, vascularity, intravascular oxygenation, and tissue morphologic characteristics which can all be of influence on the reflectance spectrum.

.

DRS has the advantage that it can be incorporated into a relatively small probe due to the fact that it can be performed with only one optical fiber with a diameter in the range of

200−400 µm (41), resulting in the possibility to perform *in vivo* analysis. In addition, it requires a relatively simple and affordable setup consisting of a spectrophotometer, a halogen light source and a single fiber. To allow for a quantitative comparison of the acquired absorption spectra, a mathematical model, which includes the absorption coefficient of all physiological relevant molecules in a specific tissue type, has to be implemented to accurately characterize the optical path length.

In order to investigate the physiology of mediastinal lymph nodes and evaluate the possibility of nodal staging in lung cancer such an algorithm was developed (41) and incorporated into an endoscopic DRS system (42,43). This customized system consists of an commercial endoscopic ultrasound system for fine needle biopsies in which a 320 µm fiber can be fed through the biopsy channel into a lymph node. Physiological parameter estimates could be performed within seconds and the biopsy procedures were extended by no longer than 5 minutes.

Based on earlier studies revealing the presence of aberrant vessels, displacement of vessels, and avascular areas in the center of metastatic lymph nodes, differentiation of metastatic from benign nodes was made on blood content and oxygen saturation levels. Initial comparison studies between malignant and benign nodes indeed revealed a lower blood volume fraction (5.6% versus 13.5%) and microvascular saturation (50% versus 84%) in malignant nodes for a study of 10 patients. The patient population was however restricted in terms of clinical suspicion to normal unenlarged, PET negative nodes and metastatic enlarged, PET positive nodes excluding nodes possibly containing smaller metastatic deposits. Furthermore, because the single fiber approach is not able to analyze the entire nodal volume, the probe has to be inserted in the tissue at a limited amount of locations (on average 5) possibly resulting in smaller metastases to be missed.
A similar reflectance spectroscopy concept utilizing three fibers inside an 1.3 mm biopsy needle was demonstrated by Evers *et al* (44) in the characterization of lung malignancies. A sensitivity of 78% and a specificity of 86% was reported in a 10 patient study and although no nodal characterization studies were performed, this concept could probably also be applied for the evaluation of freshly resected lymph nodes in an intra-operative setting.

Overall, these studies show that DRS is capable of differentiating benign from malignant tissue on the basis of different tissue characteristics which might give it a high sensitivity and specificity. However, limited studies have been performed on nodal tissue samples and the output of optical fibers restricts the size of the scanned volume to several mm^3.

1.6 Raman spectroscopy

Raman spectroscopy resolves around the inelastic scattering of photons, due to the chemical bonds of the tissue under investigation (45). The molecular bonds in the tissue, result in a small portion of the light to be inelastically scattered giving this part of the light a lower

energy thus a longer wavelength. The process leading to this inelastic scatter is termed the Raman effect and is schematically displayed in Figure 1. The shift in wavelength contains information about the different vibrational modes in the tissue, so the frequencies of the scattered photons contain information about the most Raman-active modes of vibration (46). The Raman bands in tissue generally arise from common cellular components, for example proteins (1660 cm^{-1}), nucleic acids
(1280 cm^{-1}), and lipids (2980 cm^{-1}) (47). Excitation wavelengths in the range of 700-1100 nm are generally used because absorption and autofluorescence by tissue and body fluids is minimal while the penetration depth is high. The advantage of Raman spectroscopy is its insensitivity to water, enabling *in vivo* imaging and its high spatial resolution (48). Disadvantages include the relatively expensive components and the limited penetration depth.

In 2008, a combined study of both infrared and Raman spectroscopy was performed in resected lymph nodes from patients suffering from head and neck cancer to identify biochemical and morphological changes taking place during carcinogenesis (49). By combining infrared and Raman maps with multivariate statistical analysis tools, 10 cancerous and 9 non-cancerous nodes were analyzed. The researchers showed that cancerous nodes displayed a higher nucleic acid and lower lipid and carbohydrate content compared to benign nodes which is indicative of increased cell proliferation and loss of differentiation (49). Their algorithm was able to differentiate between benign and malignant nodes in 94% of the cases.
A more extensive study on 103 lymph nodes from the head and neck region was performed in 2010 including nodal metastasis from squamous cell carcinomas, adenocarcinoma's and Hodgkin and Non-Hodgkin lymphomas. Compared to histopathology, Raman spectroscopy and principal component fed linear discriminant analysis were able to come up with the same diagnosis in 84% of the cases (50). More recently, a Raman study of 59 axillary lymph nodes of which 43 negative and 16 positive from 58 patients undergoing breast surgery was published revealing an overall sensitivity and specificity of 81% and 97% (51). In addition, the nodes could be assessed at 5 points within the volume within 9 minutes and even when the amount of measured points was doubled it could be done in under 20 minutes.
Recently a pen-size probe design was presented which specifically aimed at intra-operative assessment of lymph nodes by combining the benefit of Raman spectroscopy with the possibility of fluorescence imaging (52). Although the device has to be clinically evaluated, it showed a penetration depth of 5-10 mm and proved able to detect low levels of both Raman and fluorescent signal.

Overall these results show that Raman spectroscopy is able to differentiate between benign and malignant nodes on a molecular level and as such may be suitable for intra-operative use. In addition, multiple feasibility studies have been performed on human lymph node

samples. Whether the limited penetration depth and sampling area might restrict its clinical application requires further investigation.

1.7 Near Infrared Fluorescence Imaging

The NIR infrared wavelength range offers great potential for optical techniques due to the increased photon penetration. Near Infrared Fluorescence (NIRF) Imaging utilizes NIR excitation light to excite fluorescence particles within the tissue. After the absorption of optical energy within a fluorescent absorber the excited electron falls back to its ground state generating the emission of a photon at different frequency (54), as displayed in Figure 1. Because there is little NIR fluorescence contrast generated by most tissues, exogenous contrast agents have to be administered to increase the signal-to-background ratios. Exogenous contrast agents that emit light at the NIR region have the benefit of an increased penetration depth and lower nonspecific fluorescence due to lower absorption coefficients of tissues. These characteristics should result in a better signal-to-background compared to fluorophores in the visible wavelength ranges (55).

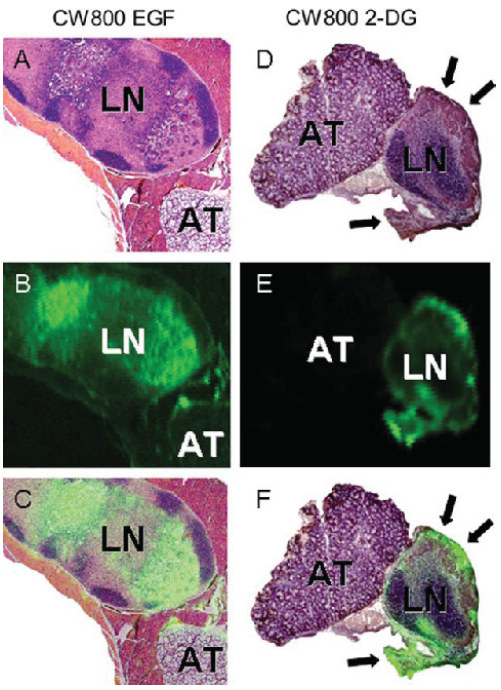

Fig. 4. Cervical lymph nodes with Oral Squamous Cell Carcinoma (OSCC) metastasis. **A.** Paraffin section of an OSCC-positive cervical lymph node (LN) surrounded by connective tissue and adipose tissue (AT). **B.** CW800 EGF fluoresence map of the OSCC-positive lymph node. **C.** Pseudocolored(green) fluorescence signal on paraffin section, notice the large resemblance with the metastatic distribution (A). **D.** Cryosection of a cervical lymph node demonstrating immunohistochemical coloring of humane OSCC cells in the border (black arrows). **E.** CW800 2-DG fluoresence map of the OSCC-positive cells. **F.** Tumorpositive areas correspond with pseudocolored (green) fluorescence signal (D). *Reproduced from (53) with kind permission of John Wiley & Sons, Ltd..*

The advantage of the technique lies in the possibility to image large areas in short amounts of time and detect small metastases with high accuracy due to the possibility of antigen labeling. The fact that only low amounts of photons can be detected from deeper tissue regions while an exogenous substance has also be administered, is less advantageous. In addition, these exogeneous substances have to be antigen coupled to target the various metastatic cells within the node more specifically.

Especially the administration exogenous contrast agent limits the clinical application of the technique due to the requirement to be approved for human use. At the moment, this confines the use of a fluorescence agent in clinical studies to Indocyanine green (ICG) which however does not offer the possibility of tumor specific antigen coupling. IRdye®800CW (CW800) (LI-Cor, Lincoln Nebraska, USA) which is on the brink of clinical approval does allow such coupling and therefore is one of the main research topics for the sensitive detection of metastases with NIR fluorescence imaging.

A study in athymic mice in 2008 using the CW800 dye coupled to the humanized anti-HER2 antibody showed that it proved possible to image the trafficking of the agent into axillary lymph nodes in real-time after subcutaneous administration in the footpads (56). In 2010, a similar agent was used to target highly metastatic breast cancer cells in mice. *Ex vivo* NIR fluorescence showed uptake in regions of lung, skin, skeletal muscle, and lymph nodes, which corresponded with the presence of cancer cells as confirmed by histologic hematoxylin and eosin stains (57). Research into the applicability of CW800 for the detection of oral nodal metastases using BALB/c mice bearing oral squamous cell carcinoma revealed that both the primary tumor as well as the cervical lymph node metastases could be imaged (53). Correlation of histopathology and fluorescent maps showed that the locations of metastases inside the lymph nodes could be pinpointed with great accuracy and resolution (Fig. 4). Coupling of the CW800 dye with radioactive tracers offers the possibility to compare the results of NIRF imaging with PET/CT. A recent study utilizing mice with prostate carcinoma enabled the visualization of nodal metastases with an antigen coupled CW800-^{64}CU complex for both microPET/CT and NIR fluorescence imaging. The authors showed that the percentage of nodal metastases detected was comparable for both techniques and emphasized the additional potential of NIR fluorescence imaging for image-guided nodal resection or staging (58). These results were confirmed by an almost similar study utilizing Panitumumab coupled CW800 to detect micrometastases in an orthotopic mouse model. A correlation with histopathology revealed the accurate detection of regional lymph node metastasis smaller than 1 mm (59). With regard to other near infrared fluorescence agents, there has also been some experience with the detection of nodal metastases using the enzyme activatable probe ProSense680 (VisEn Medical, Woburn, Massachusetts) and Cy5.5 (CyDye deoxynucleotides, GE Healthcare, Piscataway, New Jersey) showing similar accurate and high resolution correlation with histopathology in animal models (60,61). Till now, no clinical trial data has been published on the use of fluorescent dyes and NIRF imaging for intra-operative staging of lymph nodes although some research has been initiated. It is expected that once clinical research demonstrates the intra-operative benefit of NIRF, NIR dyes will be cleared by the regulatory authorities.

Overall, its penetration depth and image speed might make NIRF a suitable candidate for early intra-operative introduction, although this mainly depends on the clinical availability of fluorescent agents.

1.8 Photoacoustic imaging

In contrast to the preceding techniques which are optics based, photoacoustic imaging relies on ultrasound for image formation while photons are utilized for signal generation. Typically nanosecond lasers pulses, in the NIR or far-red wavelength range, are absorbed by optically absorbing components of the tissue under investigation. Absorption induces thermal expansion of these absorbing components (see Figure 1) generating a pressure wave in the MHz range which can be detected using ultrasound detectors. The benefit of this light/sound combination lies in an increased penetration depth, of up to several centimeters (63), where high spatial resolution is retained due to the low scattering of ultrasound waves. Further, contrast is generated based on optical absorption instead of scattering or transmission, providing an optical absorption map of the tissue under investigation. Because hemoglobin, melanin and multiple exogenous contrast substances, contain increased absorption characteristics, photoacoustics provides imaging possibilities in a wide range of clinical applications. The hybrid form of the technique also enables the use of ultrasound to provide more anatomical information. Disadvantages of the technique include the need for a coupling medium to permit sound waves to propagate and the difficulty in performing quantitative spectroscopy due to the unknown variance in optical fluence.

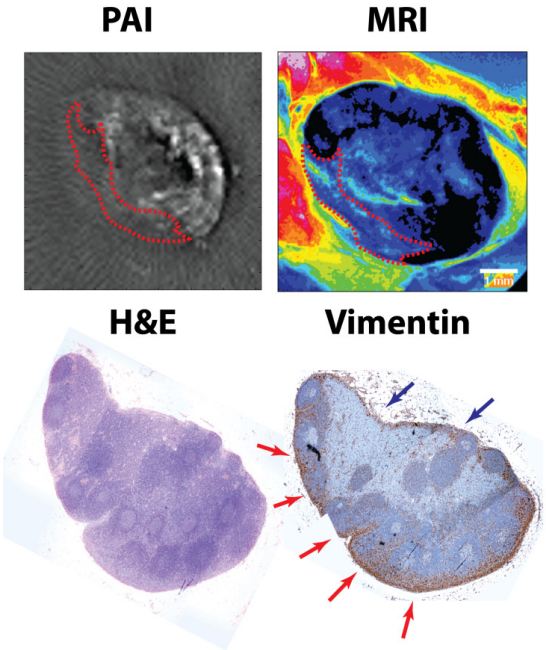

Fig. 5. Photoacoustic and MR image comparison of a resected metastatic lymph node after SPIO injection. The PA and MR images show a comparable SPIO distribution with an absence of particles in the lower left (red dotted line). Immunohistochemical staining shows the presence of the metastatic deposits predominately in the lower left. *Reproduced from (62) with permission of the journal.*

Most research in the field of nodal monitoring using photoacoustics has been performed with respect to SLN detection. Several groups have shown that SLNs can be detected non-

invasively using both clinically approved blue dyes (64,65) and other exogenous contrast agents (66,67) . However, the technique has been less frequently applied for the detection of nodal metastases. The fact that melanoma originative nodal metastases contain the natural optical absorber melanin, in most of the cases, makes the detection of these metastases possible using photoacoustics.
In 2009, McCormack *et al* showed that up to 500 melanoma cells could be photoacoustically detected inside excised animal lymph nodes although imaging could not be performed (68). Our group proved that excised human lymph nodes can be imaged and the location of melanoma metastases can be mapped. In addition, we showed that photoacoustic spectroscopy could possibly further improve the distinguishing power of the technique (69). A small study on 3 benign and 3 malignant human nodes showed that the amount of photoacoustic response and the presence or absence of specific anatomical features together with photoacoustic spectroscopic information, provided a ground for distinction (70). At the moment, work is being performed to improve the spectroscopic analysis method and implement it in a hand-held device for fast 3D intra-operative nodal staging.

With respect to tumors lacking a natural absorber, nodal metastases detection using photoacoustics could be facilitated through the addition of an exogenous contrast enhancing agent. Coupling of the agent with tumor specific antigens could further increase the sensitivity and specificity of such an approach as shown within the fluorescent field. However, in contrast to an applicable fluorescent agent, a photoacoustic agent has most to gain from a large absorption cross-section instead of an increased quantum yield, making most fluorescent agents unsuitable for photoacoustic contrast enhancement. Because PA imaging is a relatively new imaging field most concepts have been demonstrated in animal models instead of patient populations. Galanzha *et al*, for example, showed that approximately one hundred human breast cancer cells coupled to gold coated iron nanoparticles proved to be detectable for *in vivo* lymph nodes (71). These micro-metastases could furthermore be purged using the same application by applying high energy laser pulses. However, as is the situation for fluorescence, most contrast agents including goldnanoparticles, have not been cleared for human use. In order to circumvent these restrictions, our group is looking into the applicability of MR contrast dispersions for PA nodal assessment. SuperParamagnetic Iron Oxide (SPIO) nanoparticles, for example have been shown to contain a satisfactory safety profile and have therefore been cleared by European and American regulatory agencies. Several of these dispersions are for sale globally which have shown to improve MRI nodal staging for different metastatic malignancies (72). We injected Endorem® (Guerbet, Villepinte, France) in the hindpaw of several healthy animals and verified that the distribution of the deposits in the lymph nodes could be mapped with photoacoustic tomography. Results were correlated with 14T MRI images and histology. Recently, we demonstrated in a Copenhagen rat model in which popliteal nodal metastases were induced by subcutaneous MAT-lylu cell injection, that a

combination of PA and SPIO nanoparticles can be used to distinguish metastatic deposits within resected lymph nodes (Fig. 5) (62).

These new developments demonstrate that the increased penetration depth, high resolution and large sampling volume of PA imaging might facilitate intra-operative nodal analysis, although clinical validation of the sensitivity of the technique still has to be obtained.

1.9 Future Perspective

Optical techniques find themselves in an excellent position to improve the intra-operative workflow for nodal staging in the coming years. Not only do they provide the required resolution to potentially pick up smaller metastasis and offer the possibility to analyze freshly resected tissue but the amount of ongoing (clinical) research shows the additional potential they could offer with regard to time, costs and workload. An overview of the main characteristics of each technique is shown in Table 1, and offers some insight into the potential of each modality for intra-operative lymph node staging. Whether and which optical techniques might become part of standard clinical practice still remains to be debated, however as with all medical technologies, their utility will mostly be based on whether they can produce better results in terms of sensitivity and specificity, or comparable results at a lower price.

To our understanding, the availability of newly approved contrast particles will play a major role in the expansion of the position of techniques like NIRF and PA which show promising physical characteristics but lack clinical validation. Conjugation of these particles with clinically approved monoclonal antibodies like cetuximab or bevacizumab, could then further improve their sensitivity and specificity ratios. The still less than optimal accuracies reported in more elaborate clinical trials for spectroscopic techniques like ESS and FTIR might indicate that significant increases in the sensitivity of these techniques are not to be expected soon, although improvements in data processing techniques leave some room for advancement. Raman measurements on the other hand, require more time but might produce better accuracy ratios in the near future due to its abilities to differentiate between tissue types on a molecular level. Improvements in scanning speed might then follow quickly because of growing commercial interests. DRS has been shown to produce promising results in breast, lung and liver tissue (44), but lacks validation for lymph node metastases. Whether its small sample volume could be compensated with multiple measurement locations therefore remains unsure.

Table 1. Overview of the main characteristics of each optical technique

Technique	Penetration depth	Resolution	Underlying differentiation characteristic	Imaging time	Sensitivity / Specificity	Overall
OCT	2-3 mm	12 µm [18]	Optical index differences of tissue types	2-3 min (3D 300 images)	-	+/-
ESS	2-3 mm	365 µm [34] (fiber size)	Optical interactions of subcellular components	20 to 25 min to scan 1 cm^2	69% / 96% [26]	-
FTIR	2-3 mm	250-500 mm [39]	Chemical bond composition	2-3 min	80% / 92% [39]	+/-
DRS	2-3 mm	320 µm [42] (fiber size)	Optical interactions of subcellular components	± 5 min	-	+/-
Raman	5 -10 mm	10 µm [51]	Vibrational modes of molecules	10-20 min	81% / 97% [51]	++
NIRF	5 -10 mm	21-337 µm [53]	Differences in Fluorescent capability	Real time	-	+
PA	10 – 20 mm	125 µm [73]	Differences in optical absorption	1 min	-	+

A combination of optical techniques or a hybrid application utilizing conventional medical imaging solutions like ultrasound could further minimize some disadvantages of optical modalities while increasing overall detection rates. Because several of the discussed applications can be constructed of low prized components, the costs of such hybrid applications would only be marginally higher compared to the conventional imaging modality. In addition, technological progress will no doubt decrease the price of components for techniques like Raman making their assembly into a hybrid modality less costly. Hybridization of optical techniques with MRI or SPECT/CT remains more dependent on the availability of multi-modal contrast particles but should also not be ruled out, as shown in combination with photoacoustics (74).

In summary, after many years of basic research, recent innovations show that optical modalities reached the point of clinical translation. Intra-operative nodal staging is just one of the fields in which these techniques might prove to be beneficial and the relative minor influence on clinical workflow in this area might make an introduction even more feasible. More elaborate clinical trials are just starting to be initiated and hopefully result in more insight into which techniques are able to provide a real contribution to intra-operative decision making.

1.10 References

1. Krag D, Weaver D, Ashikaga T, Moffat F, Klimberg VS, Shriver C, Feldman S, Kusminsky R, Gadd M, Kuhn J, Harlow S, Beitsch P. The sentinel node in breast cancer--a multicenter validation study. N Engl J Med 1998; 339(14):941-946.
2. Balch CM, Soong SJ, Gershenwald JE, Thompson JF, Reintgen DS, Cascinelli N, Urist M, McMasters KM, Ross MI, Kirkwood JM, Atkins MB, Thompson JA, Coit DG, Byrd D, Desmond R, Zhang Y, Liu PY, Lyman GH, Morabito A. Prognostic factors analysis of 17,600 melanoma patients: validation of the American Joint Committee on Cancer melanoma staging system. J Clin Oncol 2001; 19(16):3622-3634.
3. von Bodman C, Godoy G, Chade DC, Cronin A, Tafe LJ, Fine SW, Laudone V, Scardino PT, Eastham JA. Predicting biochemical recurrence-free survival for patients with positive pelvic lymph nodes at radical prostatectomy. J Urol 2010; 184(1):143-148.
4. Balch CM, Morton DL, Gershenwald JE, McMasters KM, Nieweg OE, Powell B, Ross MI, Sondak VK, Thompson JF. Sentinel node biopsy and standard of care for melanoma. J Am Acad Dermatol 2009; 60(5):872-875.
5. van der Velde-Zimmermann D, Schipper ME, de Weger RA, Hennipman A, Borel Rinkes IH. Sentinel node biopsies in melanoma patients: a protocol for accurate, efficient, and cost-effective analysis by preselection for immunohistochemistry on the basis of Tyr-PCR. Ann Surg Oncol 2000; 7(1):51-54.
6. Balch CM, Soong S, Ross MI, Urist MM, Karakousis CP, Temple WJ, Mihm MC, Barnhill RL, Jewell WR, Wanebo HJ, Harrison R. Long-term results of a multi-institutional randomized trial comparing prognostic factors and surgical results for intermediate thickness melanomas (1.0 to 4.0 mm). Intergroup Melanoma Surgical Trial. Ann Surg Oncol 2000; 7(2):87-97.
7. Hadleigh C, Cawthorn S. Assay Project Rapid Intra-Operative Lymph Node Analysis for Breast Cancer Patient. North Trent Region, UK, 2009 North Trent Cancer Network, NHS; 2009.
8. Wrightson WR, Wong SL, Edwards MJ, Chao C, Reintgen DS, Ross MI, Noyes RD, Viar V, Cerrito PB, McMasters KM. Complications associated with sentinel lymph node biopsy for melanoma. Ann Surg Oncol 2003; 10(6):676-680.
9. Tanis PJ, Boom RP, Koops HS, Faneyte IF, Peterse JL, Nieweg OE, Rutgers EJ, Tiebosch AT, Kroon BB. Frozen section investigation of the sentinel node in malignant melanoma and breast cancer. Ann Surg Oncol 2001; 8(3):222-226.
10. Creager AJ, Shiver SA, Shen P, Geisinger KR, Levine EA. Intraoperative evaluation of sentinel lymph nodes for metastatic melanoma by imprint cytology. Cancer 2002; 94(11):3016-3022.
11. Alvarez S, Anorbe E, Alcorta P, Lopez F, Alonso I, Cortes J. Role of sonography in the diagnosis of axillary lymph node metastases in breast cancer: a systematic review. AJR Am J Roentgenol 2006; 186(5):1342-1348.
12. Thompson JF, Haydu LE, Sanki A, Uren RF. Ultrasound assessment of lymph nodes in the management of early-stage melanoma. J Surg Oncol 2011; 104(4):354-360.

13. Peare R, Staff RT, Heys SD. The use of FDG-PET in assessing axillary lymph node status in breast cancer: a systematic review and meta-analysis of the literature. Breast Cancer Res Treat 2010; 123(1):281-290.
14. Xing Y, Bronstein Y, Ross MI, Askew RL, Lee JE, Gershenwald JE, Royal R, Cormier JN. Contemporary diagnostic imaging modalities for the staging and surveillance of melanoma patients: a meta-analysis. J Natl Cancer Inst 2011; 103(2):129-142.
15. Gerber B, Heintze K, Stubert J, Dieterich M, Hartmann S, Stachs A, Reimer T. Axillary lymph node dissection in early-stage invasive breast cancer: is it still standard today? Breast Cancer Res Tr 2011; 128(3):613-624.
16. Serway RA, Jewett JW. Physics for scientists and engineers: Brooks/Cole Publishing Company. 2009.
17. Huang D, Swanson EA, Lin CP, Schuman JS, Stinson WG, Chang W, Hee MR, Flotte T, Gregory K, Puliafito CA. Optical coherence tomography: Massachusetts Institute of Technology, Whitaker College of Health Sciences and Technology; 1993.
18. John R, Adie SG, Chaney EJ, Marjanovic M, Tangella KV, Boppart SA. Three-dimensional Optical Coherence Tomography for Optical Biopsy of Lymph Nodes and Assessment of Metastatic Disease. Ann Surg Oncol 2012.
19. Davis AM, Choma MA, Izatt JA. Heterodyne swept-source optical coherence tomography for complete complex conjugate ambiguity removal. J Biomed Opt 2005; 10(6):064005.
20. Vakoc BJ, Fukumura D, Jain RK, Bouma BE. Cancer imaging by optical coherence tomography: preclinical progress and clinical potential. Nat Rev Cancer 2012; 12(5):363-368.
21. Iftimia NV, Mujat M, Ustun T, Ferguson RD, Danthu V, Hammer DX. Spectral-domain low coherence interferometry/optical coherence tomography system for fine needle breast biopsy guidance. Rev Sci Instrum 2009; 80(2):024302.
22. Luo W, Nguyen FT, Zysk AM, Ralston TS, Brockenbrough J, Marks DL, Oldenburg AL, Boppart SA. Optical biopsy of lymph node morphology using optical coherence tomography. Technol Cancer Res Treat 2005; 4(5):539-548.
23. McLaughlin RA, Scolaro L, Robbins P, Hamza S, Saunders C, Sampson DD. Imaging of human lymph nodes using optical coherence tomography: potential for staging cancer. Cancer Res 2010; 70(7):2579-2584.
24. McLaughlin RA, Scolaro L, Robbins P, Saunders C, Jacques SL, Sampson DD. Parametric imaging of cancer with optical coherence tomography. J Biomed Opt 2010; 15(4):046029.
25. Hakam A, Khin NN. Intraoperative imprint cytology in assessment of sentinel lymph nodes and lumpectomy surgical margins. Clin Lab Med 2005; 25(4):795-807, viii.
26. Keshtgar MR, Chicken DW, Austwick MR, Somasundaram SK, Mosse CA, Zhu Y, Bigio IJ, Bown SG. Optical scanning for rapid intraoperative diagnosis of sentinel node metastases in breast cancer. Br J Surg 2010; 97(8):1232-1239.
27. Boustany NN, Boppart SA, Backman V. Microscopic imaging and spectroscopy with scattered light. Annu Rev Biomed Eng 2010; 12:285-314.
28. Van de Hulst HC. Light Scattering by Small Particles. . John Wiley & Sons, New York 1957.

29. Perelman LT, Backman V, Wallace M, Zonios G, Manoharan R, Nusrat A, Shields S, Seiler M, Lima C, Hamano T, Itzkan I, Van Dam J, Crawford JM, Feld MS. Observation of periodic fine structure in reflectance from biological tissue: A new technique for measuring nuclear size distribution. Phys Rev Lett 1998; 80(3):627-630.
30. Mourant JR, Boyer J, Hielscher AH, Bigio IJ. Influence of the scattering phase function on light transport measurements in turbid media performed with small source-detector separations. Opt Lett 1996; 21(7):546-548.
31. Arifler D, Guillaud M, Carraro A, Malpica A, Follen M, Richards-Kortum R. Light scattering from normal and dysplastic cervical cells at different epithelial depths: finite-difference time-domain modeling with a perfectly matched layer boundary condition. J Biomed Opt 2003; 8(3):484-494.
32. Jerjes W, Swinson B, Pickard D, Thomas GJ, Hopper C. Detection of cervical intranodal metastasis in oral cancer using elastic scattering spectroscopy. Oral Oncol 2004; 40(7):673-678.
33. Johnson KS, Chicken DW, Pickard DC, Lee AC, Briggs G, Falzon M, Bigio IJ, Keshtgar MR, Bown SG. Elastic scattering spectroscopy for intraoperative determination of sentinel lymph node status in the breast. J Biomed Opt 2004; 9(6):1122-1128.
34. Austwick MR, Clark B, Mosse CA, Johnson K, Chicken DW, Somasundaram SK, Calabro KW, Zhu Y, Falzon M, Kocjan G, Fearn T, Bown SG, Bigio IJ, Keshtgar MR. Scanning elastic scattering spectroscopy detects metastatic breast cancer in sentinel lymph nodes. J Biomed Opt 2010; 15(4):047001.
35. Griffiths P, De Haseth JA. Fourier transform infrared spectrometry: Wiley-Interscience. 2007.
36. Berthomieu C, Hienerwadel R. Fourier transform infrared (FTIR) spectroscopy. Photosynth Res 2009; 101(2-3):157-170.
37. Diem M, Romeo M, Boydston-White S, Miljkovic M, Matthaus C. A decade of vibrational micro-spectroscopy of human cells and tissue (1994-2004). Analyst 2004; 129(10):880-885.
38. Brian CS. Fundamentals of Fourier Transform Infrared Spectroscopy: CRC Press, LLC, Florida. 1996.
39. Liu Y, Xu Y, Zhang Y, Wang D, Xiu D, Xu Z, Zhou X, Wu J, Ling X. Detection of cervical metastatic lymph nodes in papillary thyroid carcinoma by Fourier transform infrared spectroscopy. Br J Surg 2011; 98(3):380-384.
40. Das K, Kendall C, Isabelle M, Fowler C, Christie-Brown J, Stone N. FTIR of touch imprint cytology: a novel tissue diagnostic technique. J Photochem Photobiol B 2008; 92(3):160-164.
41. Kanick SC, Sterenborg HJ, Amelink A. Empirical model of the photon path length for a single fiber reflectance spectroscopy device. Opt Express 2009; 17(2):860-871.
42. Kanick SC, van der Leest C, Aerts JG, Hoogsteden HC, Kascakova S, Sterenborg HJ, Amelink A. Integration of single-fiber reflectance spectroscopy into ultrasound-guided endoscopic lung cancer staging of mediastinal lymph nodes. J Biomed Opt 2010; 15(1):017004.
43. Kanick SC, van der Leest C, Djamin RS, Janssens AM, Hoogsteden HC, Sterenborg HJ, Amelink A, Aerts JG. Characterization of mediastinal lymph node

physiology in vivo by optical spectroscopy during endoscopic ultrasound-guided fine needle aspiration. J Thorac Oncol 2010; 5(7):981-987.
44. Evers DJ, Nachabe R, Klomp HM, van Sandick JW, Wouters MW, Lucassen GW, Hendriks BH, Wesseling J, Ruers TJ. Diffuse Reflectance Spectroscopy: A New Guidance Tool for Improvement of Biopsy Procedures in Lung Malignancies. Clin Lung Cancer 2012.
45. Zavaleta CL, Kircher MF, Gambhir SS. Raman's "effect" on molecular imaging. J Nucl Med 2011; 52(12):1839-1844.
46. Stelling A, Salzer R, Kirsch M, Sobottka SB, Geiger K, Koch E, Schackert G, Steiner G. Intra-operative optical diagnostics with vibrational spectroscopy. Anal Bioanal Chem 2011; 400(9):2745-2753.
47. Kendall C, Isabelle M, Bazant-Hegemark F, Hutchings J, Orr L, Babrah J, Baker R, Stone N. Vibrational spectroscopy: a clinical tool for cancer diagnostics. Analyst 2009; 134(6):1029-1045.
48. Petibois C, Desbat B. Clinical application of FTIR imaging: new reasons for hope. Trends Biotechnol 2010; 28(10):495-500.
49. Isabelle M, Stone N, Barr H, Vipond M, Shepherd N, Rogers K. Lymph node pathology using optical spectroscopy in cancer diagnostics. Spectrosc-Int J 2008; 22(2-3):97-104.
50. Orr LE, Christie-Brown J, Hutchings JC, McCarthy K, Rose S, Thomas M, Stone N. Raman spectroscopy as a tool for the identification and differentiation of neoplasias contained within lymph nodes of the head and neck. Proc Spie 2010; 7548.
51. Horsnell JD, Smith JA, Sattlecker M, Sammon A, Christie-Brown J, Kendall C, Stone N. Raman spectroscopy - A potential new method for the intra-operative assessment of axillary lymph nodes. Surg-J R Coll Surg E 2012; 10(3):123-127.
52. Mohs AM, Mancini MC, Singhal S, Provenzale JM, Leyland-Jones B, Wang MD, Nie S. Hand-held Spectroscopic Device for In Vivo and Intraoperative Tumor Detection: Contrast Enhancement, Detection Sensitivity, and Tissue Penetration. Anal Chem 2010.
53. Keereweer S, Kerrebijn JD, Mol IM, Mieog JS, Van Driel PB, Baatenburg de Jong RJ, Vahrmeijer AL, Lowik CW. Optical imaging of oral squamous cell carcinoma and cervical lymph node metastasis. Head Neck 2012; 34(7):1002-1008.
54. Lakowicz JR. Principles of fluorescence spectroscopy: Springer. 2006.
55. Rasmussen JC, Kwon S, Sevick-Muraca EM, Cormier JN. The role of lymphatics in cancer as assessed by near-infrared fluorescence imaging. Ann Biomed Eng 2012; 40(2):408-421.
56. Sampath L, Wang W, Sevick-Muraca EM. Near infrared fluorescent optical imaging for nodal staging. Journal of biomedical optics 2008; 13:041312.
57. Sampath L, Kwon S, Hall MA, Price RE, Sevick-Muraca EM. Detection of Cancer Metastases with a Dual-labeled Near-Infrared/Positron Emission Tomography Imaging Agent. Transl Oncol 2010; 3(5):307-217.
58. Hall MA, Kwon S, Robinson H, Lachance PA, Azhdarinia A, Ranganathan R, Price RE, Chan W, Sevick-Muraca EM. Imaging prostate cancer lymph node metastases with a multimodality contrast agent. Prostate 2012; 72(2):129-146.

59. Heath CH, Deep NL, Sweeny L, Zinn KR, Rosenthal EL. Use of Panitumumab-IRDye800 to Image Microscopic Head and Neck Cancer in an Orthotopic Surgical Model. Ann Surg Oncol 2012.
60. Keereweer S, Mieog JS, Mol IM, Van Driel PB, Snoeks TJ, Baatenburg de Jong RJ, Vahrmeijer AL, Kerrebijn JD, Lowik CW. Detection of oral squamous cell carcinoma and cervical lymph node metastasis using activatable near-infrared fluorescence agents. Arch Otolaryngol Head Neck Surg 2011; 137(6):609-615.
61. Gleysteen JP, Newman JR, Chhieng D, Frost A, Zinn KR, Rosenthal EL. Fluorescent labeled anti-EGFR antibody for identification of regional and distant metastasis in a preclinical xenograft model. Head Neck 2008; 30(6):782-789.
62. Grootendorst DJ, Fratila RM, Visscher M, Ten Haken B, Van Wezel RJM, Rottenberg S, Steenbergen W, Manohar S, Ruers TJM. Intra-operative ex vivo photoacoustic nodal staging in a rat model using a clinical superparamagnetic iron oxide nanoparticle dispersion. J Biophotonics 2013; Ahead of Print.
63. Kim C, Erpelding TN, Jankovic L, Pashley MD, Wang LV. Deeply penetrating in vivo photoacoustic imaging using a clinical ultrasound array system. Biomed Opt Express 2010; 1(1):278-284.
64. Kim C, Erpelding TN, Jankovic L, Wang LV. Performance benchmarks of an array-based hand-held photoacoustic probe adapted from a clinical ultrasound system for non-invasive sentinel lymph node imaging. Philos Transact A Math Phys Eng Sci 2011; 369(1955):4644-4650.
65. Akers WJ, Edwards WB, Kim C, Xu B, Erpelding TN, Wang LV, Achilefu S. Multimodal sentinel lymph node mapping with single-photon emission computed tomography (SPECT)/computed tomography (CT) and photoacoustic tomography. Transl Res 2012; 159(3):175-181.
66. Akers WJ, Kim C, Berezin M, Guo K, Fuhrhop R, Lanza GM, Fischer GM, Daltrozzo E, Zumbusch A, Cai X, Wang LV, Achilefu S. Noninvasive photoacoustic and fluorescence sentinel lymph node identification using dye-loaded perfluorocarbon nanoparticles. ACS Nano 2011; 5(1):173-182.
67. Pan D, Cai X, Yalaz C, Senpan A, Omanakuttan K, Wickline SA, Wang LV, Lanza GM. Photoacoustic sentinel lymph node imaging with self-assembled copper neodecanoate nanoparticles. ACS Nano 2012; 6(2):1260-1267.
68. McCormack D, Al-Shaer M, Goldschmidt BS, Dale PS, Henry C, Papageorgio C, Bhattacharyya K, Viator JA. Photoacoustic Detection of Melanoma Micrometastasis in Sentinel Lymph Nodes. Journal of Biomechanical Engineering-Transactions of the Asme 2009; 131(7).
69. Jose J, Grootendorst DJ, Vijn TW, Wouters M, van Boven H, van Leeuwen TG, Steenbergen W, Ruers TJ, Manohar S. Initial results of imaging melanoma metastasis in resected human lymph nodes using photoacoustic computed tomography. J Biomed Opt 2011; 16(9):096021.
70. Grootendorst DJ, Jose J, Wouters MW, van Boven H, Van der Hage J, Van Leeuwen TG, Steenbergen W, Manohar S, Ruers TJ. First experiences of photoacoustic imaging for detection of melanoma metastases in resected human lymph nodes. Lasers Surg Med 2012; 44(7):541-549.
71. Galanzha EI, Kokoska MS, Shashkov EV, Kim JW, Tuchin VV, Zharov VP. In vivo fiber-based multicolor photoacoustic detection and photothermal purging of

metastasis in sentinel lymph nodes targeted by nanoparticles. J Biophotonics 2009; 2(8-9):528-539.
72. Will O, Purkayastha S, Chan C, Athanasiou T, Darzi AW, Gedroyc W, Tekkis PP. Diagnostic precision of nanoparticle-enhanced MRI for lymph-node metastases: a meta-analysis. Lancet Oncol 2006; 7(1):52-60.
73. Jose J, Willemink RG, Resink S, Piras D, van Hespen JC, Slump CH, Steenbergen W, van Leeuwen TG, Manohar S. Passive element enriched photoacoustic computed tomography (PER PACT) for simultaneous imaging of acoustic propagation properties and light absorption. Opt Express 2011; 19(3):2093-2104.
74. Grootendorst DJ, Jose J, Fratila RM, Visscher M, Velders AH, Ten Haken B, Van Leeuwen TG, Steenbergen W, Manohar S, Ruers TJM. Evaluation of superparamagnetic iron oxide nanoparticles (Endorem®) as a photoacoustic contrast agent for intra-operative nodal staging. Contrast Media & Molecular Imaging 2013; 8(1):83-91.

AIM OF RESEARCH

The following chapters provide an overview of our scientific achievements which were aimed at exploring the applicability of photoacoustic imaging for the staging of lymph nodes during surgical procedures. As described in Chapter 1, the intra-operative workflow for the analysis of (sentinel) lymph nodes could be significantly improved if a fast, accurate and surgical compatible imaging modality would find its way into the operation theatre. We hypothesized that photoacoustics might be such an imaging technique and aimed to look into the feasibility of such an approach. Because most melanoma metastases possess some amount of the endogenous absorber melanin, we validated the feasibility of photoacoustics for melanoma detection in human samples while we designed animal experiments to validate its applicability in other malignancies utilizing exogenous PA contrast substances. The thesis is therefore divided into two sections. Chapter 2 to 3 address our findings with regard to melanoma metastases while Chapter 4 to 7 focuses on the use of SPIO nanoparticles in their role as PA contrast agents. In Chapter 8 we draw several general conclusions and give some future perspectives.

CHAPTER 2

INITIAL RESULTS OF IMAGING MELANOMA METASTASIS IN RESECTED HUMAN LYMPH NODES USING PHOTOACOUSTIC COMPUTED TOMOGRAPHY*

The pathological status of the sentinel lymph node is important for accurate melanoma staging, ascertaining prognosis and planning treatment. The standard procedure involves biopsy of the node and histopathological assessment of its status. Drawbacks of this examination include a finite sampling of the node with the likelihood of missing metastases, and a significant time-lag before histopathological results are available to the surgeon. We studied the applicability of photoacoustic computed tomographic imaging as an intra-operative modality for examining the status of resected human sentinel lymph nodes. We first applied the technique to image ex vivo pig lymph nodes carrying metastases-simulating melanoma cells using multiple wavelengths. The experience gained was applied to image a suspect human lymph node. We validated the photoacoustic imaging results by comparing a reconstructed slice with a histopathological section through the node. Our results suggest that photoacoustics has the potential to develop into an intra-operative imaging method to detect melanoma metastases in sentinel lymph nodes.

* This chapter has been published as: J. Jose, D. J. Grootendorst, T. W. Vijn, M. Wouters, H. van Boven, T. G. van Leeuwen, W. Steenbergen, T. J. M. Ruers, and S. Manohar, "Initial results of imaging melanoma metastasis in resected human lymph nodes using photoacoustic computed tomography" Journal of Biomedical Optics 16 096021 (2011)

2.1 Introduction

The incidence of cutaneous melanoma, the deadliest form of skin cancer, is a major public health problem around the world. In the United States alone, around 68,000 new cases of skin melanoma were expected in 2010 (1). In Europe, the estimated figure for 2008 was similar, 67,000 (2). At the time when incidence of many cancer types is decreasing, melanoma incidence is increasing at the rate of between 3-4% per year. The main reason for this is thought to be increasing intermittent over-exposure to natural ultraviolet light of pale, non-acclimatized caucasian skin.

The treatment for early stage melanoma is primarily focused on wide surgical excision of the primary tumor. For melanomas with an invasion depth (Breslow thickness) > 1 mm, histopathological assessment of the first draining lymph node(s), the sentinel lymph node(s) (SLN), is performed (3). The pathological status of the SLN is an accurate reflection of the pathological status of the other nodes in the regional nodal basin which in turn is a strong predictor of patient survival (4). Patients with metastases in their SLNs are treated with radical lymphadenectomy of the other lymph nodes in the regional basin, which has been shown to increase survival (4). The SLN is identified by lymphatic mapping using radiocolloid and/or vital blue dye. After excision, the SLN is examined in sections stained with hematoxylin and eosin (H&E), and by immunohistochemical analysis with the use of specific antibodies.

Histopathology in combination with immunohistochemical staining is able to detect micrometastases from clumps right down to solitary melanoma cells. Despite the indisputable merits of the approach, there are disadvantages. The first is related to the act of physically sectioning the structure in finite samples, which leads to an incomplete examination of the node. This could cause micrometastases to be missed leading to false-negative outcomes and wrongly refraining from radical lymphadenectomy. The second disadvantage is that the results of histopathology are not immediately available to the surgeon, taking an average of 4-5 days (5). In case of tumor positive SLN diagnosis, this implies that complete lymphadenectomy cannot be performed during the sentinel node procedure but has to be planned in a second separate procedure. The two-step surgical procedure: SLN excision and complete lymph node basin excision, is consorted by increased patient discomfort, higher costs, organizational distress and is time-consuming.

These disadvantages could be addressed by the introduction of an intra-operative complete SLN assessment modality, where the excised SLN could be examined in real/near-real time. In the case of a positive SLN a radical lymphadenectomy could be performed directly without scheduling a second surgery at a later date. Methods such as high resolution ultrasound imaging (6) and frozen section histopathological examination (7) have been evaluated as intra-operative techniques to lead to one-step surgery. However these methods have not achieved the required sensitivities, with false negative rates up to 10 % (6).

Photoacoustic (PA) imaging could be one of the technologies able to address these shortcomings. PA imaging is an optical absorption based modality, which uses pulsed laser-induced ultrasound from specific endogenous tissue chromophores (e.g., melanin or hemoglobin) to map their distribution. In contrast to purely optical imaging, PA imaging retains good spatial resolutions at higher imaging depths since ultrasound waves are not scattered as highly as photons inside biological tissue. Since melanin possesses high optical absorption, melanoma can be detected and imaged using PA imaging without additional labeling.

Viator and co-workers developed PA systems for the *ex vivo* detection of circulating tumor cells (CTC) of melanoma, using piezoelectric detection (8) Zharov *et al* introduced a PA flow cytometry approach for the *in vivo* detection of the presence and concentration of melanoma CTCs in blood (9). Wang and co-workers obtained *in vivo* three-dimensional (3-D) melanoma images in nude mice using dark-field confocal PA microscopy (10). More recently, this group went on further to image single melanoma cells *in vivo* using sub-wavelength-resolution PA microscopy (11,12).

The group of Viator advocated the use of PA for detecting melanoma metastases in lymph nodes by using the elevated PA signal responses from melanoma cells implanted in the canine lymph nodes (13), while normal lymph nodes showed low responses. Even though their approach shows high sensitivities, other absorbing structures within nodes also cause PA signals which are difficult to distinguish from melanoma cell responses even when multiple wavelengths are being used. Before PA can be translated to the clinic, an improved method is required which can image the node by mapping various absorbing structures and will allow better discrimination of melanoma cells in the context of known lymph node components/structures such as connective tissue distributions, blood vessels etc.

In this study, we present such an approach using a PA computed tomography (PACT) system, which can generate sliced images of lymph nodes. We show the ability of the system to image micrometastases-simulating melanoma cell clumps in an *ex vivo* animal lymph node. The images are obtained at multiple wavelengths to ascertain wavelength-dependent contrast of melanoma cells to lymph node tissue. We then present the first imaging findings of a resected human lymph node and compare these with conventional histopathology.

2.2 Materials and methods

Figure 1 shows the schematic of the top-illumination PACT system. The lymph node is accommodated in a 20 mm deep hollow scooped out from the top of an agar gel cylinder (3% agar, Sigma-Aldrich). The lymph node is immersed in PBS (phosphate buffered saline) inside the hollow, and the agar gel cylinder is mounted in the imaging tank filled with water (Figure 1(b)). Light from an optical parametric oscillator (Opotek, 700-950 nm) pumped by a Q-switched Nd:YAG laser (Brilliant B, Quantel) operating at 10 Hz repetition rate is used to illuminate the node from above.

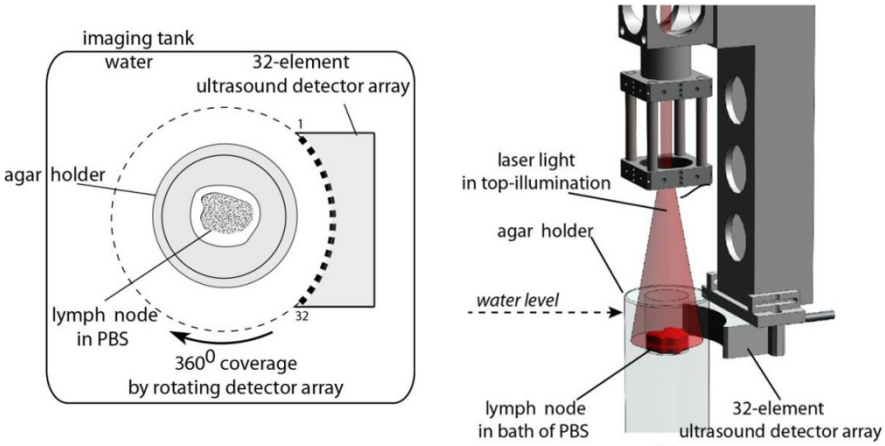

Fig. 1 The PACT instrument utilizing top-illumination. The lymph node is placed in PBS in a hollow in the agar gel cylinder. The detector array is rotated around the object in water.

The imager uses a 32-element curvilinear ultrasound detector array (Imasonic, Besançon) with a 32-channel pulser-receiver system (Lecoeur Electronique, Paris) for data acquisition (14). The piezocomposite elements of the detector have a central frequency of 6.25 MHz with a receiving bandwidth greater than 80%. Each element is shaped to produce an elevation plane focus of 1 mm at a distance of 48 mm from the detector surface. In each channel of the pulser-receiver system the PA signal is amplified by 60 dB, digitized with a sampling rate of 80 MS/s and transferred to the PC. Filtered acoustic backprojection (14) is used to reconstruct the PA images off-line. Prior to each set of measurements, a calibration measurement is performed using a horsetail hair, to ascertain the CT imaging geometry such as centre of rotation, position of detector elements and also the speed of sound in water.

To assess the sensitivity of the system in detecting melanoma cells, we imaged pork lymph nodes, specially prepared to simulate melanoma positive nodes. We first prepared 2% agar solutions in PBS mixed with specific counts of B16 mouse melanoma cells; constant stirring under 30^0 C heating promoted dissolution of agar and homogeneous distribution of

the cells. Slowly pipetting out 10 μl of the warm mixture using a micropipette with a 20 μl tip, resulted in 1-1.5 mm diameter drops which turned into solid beads once they cooled down. Such agar gel beads embedded with melanoma cells, simulating metastatic clumps, were inserted into a pork lymph node obtained from a butcher. Beads were embedded into the node using a 16G needle. After bead insertion the needle channel is gently squeezed and kneaded closed.

2.3 Results and discussions

Figure 2(a) is the photograph of a pig lymph node with next to it two beads of 10 μl volume (roughly 1.5 mm in diameter) containing $5x10^5$ and $5x10^4$ melanoma cells. The beads were imaged using 720, 760, 800 and 850 nm with a fluence of $12mJ/cm^{-2}$ per pulse .Data acquisition per slice for 100 signal averages and 9 projections takes 120 seconds; image reconstruction for a 300x300 pixel image takes 40 seconds. Figure 2(b) is a PA slice image through the center of the node before bead insertion at 6 mm from the top surface. The corresponding PA slice images after the beads were inserted in the lymph node and sealed,

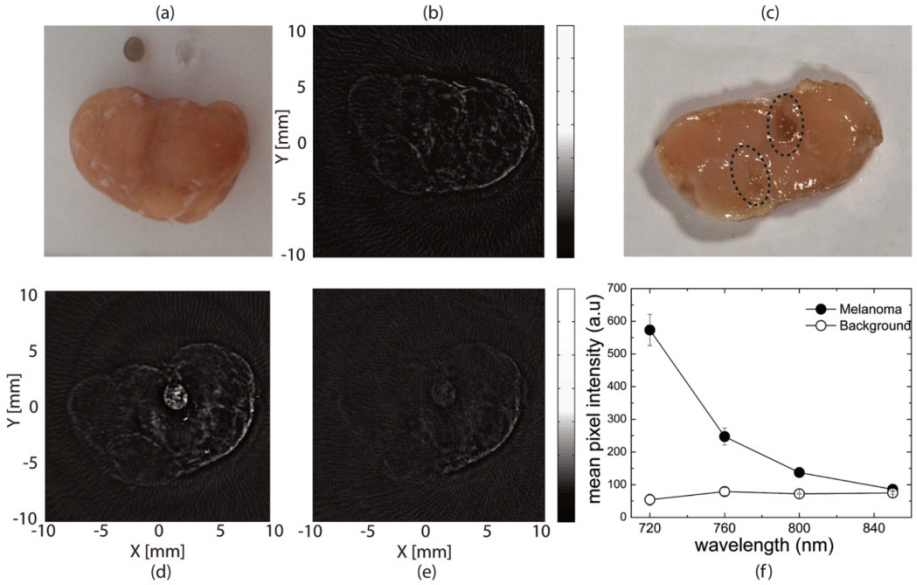

Fig 2: (a) Photograph of the pig lymph node and agar gel beads embedded with melanoma cells, the darker bead carrying $5x10^5$ cells and the other $5x10^4$ cells, (b) PACT image using 720 nm light of the node prior to bead-insertion, (c) Photograph of sliced lymph node exposing the beads; the right dotted circle marks the $5x10^5$ cell bead and left dotted circle marks the $5x10^4$ cell bead, (d) and (e) are the PACT images of the lymph node after bead-insertion using wavelengths of excitation 720 nm, and 800nm. (f) normalized mean pixel intensity (MPI) of the melanoma bead and the background lymph node plotted against wavelength.

are shown in Figs. 2(d)-(e) at wavelengths 720 and 800 nm respectively. The images were acquired at the same height through the node center; Fig.2(c) is a photograph of the cross-section of the lymph node at roughly the same height, exposed using a scalpel. The dotted circles respectively mark the positions of the beads containing $5x10^5$ and $5x10^4$ melanoma cells.

The bead with $5x10^5$ melanoma cells is well depicted in Figs. 2(d) and (e), while the bead with $5x10^4$ melanoma cells is not visible. The fibrous capsule of the lymph node consisting of trabeculae could be discernable due to collagen, but increased intensity could also be caused by the presence of remnant blood in the blood vessels. Patterns in the lymph node whether with or without the beads (Figs.2(b) (d) and (e)), can also be distinguished, which are most likely collagen associated with the inner trabeculae, which mark the division of the node into follicles. Another source of signal could be blood vessels in the trabeculae. We performed spectral analysis of pixel clusters (10x10 pixel) in melanoma cell regions and the lymph node background regions (border region between 3 and 5 'O' clock in Fig. 2(d)). Figure 2 (f) shows the normalized mean pixel intensity (MPI) against wavelength for the melanoma bead region and background. Increasing MPI values with decreasing wavelengths are indicative of increased absorption of light by melanin (15).

The imaging of human lymph nodes was based on a study protocol approved by the Medical Ethics Committee (METC) of the Netherlands Cancer Institute—Antoni van Leeuwenhoek Hospital, Amsterdam (NKI-AvL). Patients with the diagnosis of cutaneous melanoma undergoing radical lymphadenectomy following discovery of tumor-positive SLN or clinically detectable nodal recurrence are included in the study after informed consent. Visually identified macroscopic pathological nodes are transported in PBS to the University of Twente, Enschede. After imaging, the nodes are placed in 4% formaldehyde and returned to the Department of Pathology at the NKI-AvL, for standard histopathological examination. Considerations of Good Clinical Practice (GCP) such as maintaining patient anonymity are stringently adhered to. Images using PACT are later correlated with histopathological findings.

A lymph node was obtained from the second echelon lymph node basin from a patient, after regional lymphadenectomy. Figure 3 (a) is a photograph of the node. Eighteen projections of PA signals were obtained in a slice roughly at the center of the node using the same set of wavelengths as before, with a fluence of 12 $mJcm^{-2}$ per pulse. Signals were averaged 100 times and each measurement lasted 4 minutes. Figure 3 (b) shows the reconstructed slice at 720 nm approximately 5 mm beneath the nodal surface. The slice shows a diffuse distribution of increased intensity throughout the nodal area. In some regions (between 1 and 4 'o' clock) absorption hot spots are also observed. Figure 3(c) is the gross histopathology section of the lymph node at a depth of 5 mm from the surface.

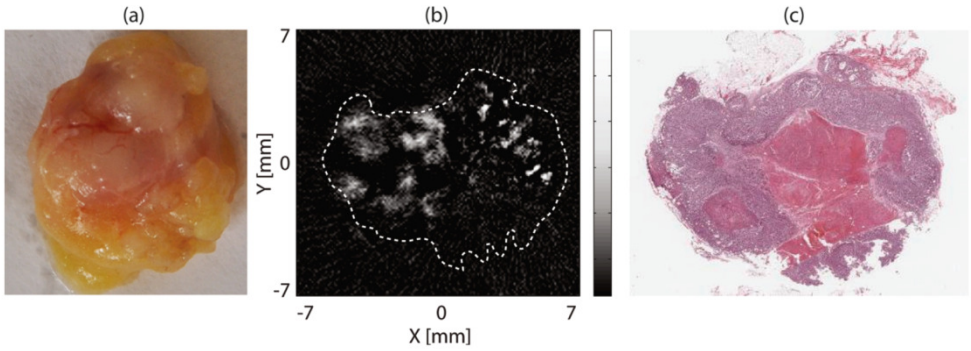

Fig 3: (a) Photograph of the resected human lymph node, (b) Photoacoustic slice image in roughly the center of the node using 720 nm excitation, showing a diffuse speckled distribution of high absorption. The right centre of the node does not contain these high absorption characteristics. (c) histopathology (H&E) section of the corresponding slice; the darker regions correspond with melanoma cells and the lighter region in the right centre is indicative for a necrotic area. (See text for details.)

H&E staining shows that intact melanoma cells are situated throughout the entire node (dark pink) with exception of the center area of the node which is occupied by a necrotic center (light pink). The size of the histopathological image corresponds with the outline of the photoacoustic image which shows lack of absorption in the right centre of the node corresponding with the location of the necrotic area. In addition, melanoma cell concentrations vary from location to location which could explain the varying contrast throughout the rest of the node. The two images however cannot be compared on a point-by-point basis and show differences in size and locations of the metastasized regions. This could be due to differences in the positions of the slices probed by the two methods. In addition, it is likely that the degree of pigmentation of the metastasized cells in the node is different at different locations: while the PA image will map such a variation, the H&E section does not.

2.4 Summary

In summary, we showed the first PACT images of melanoma metastasis in a suspect resected human lymph node. The 2-D tomogram of optical absorption showed a gross distribution of melanoma metastases within the node. The histopathological findings supported the images. The human node study protocol was developed based on experiences with phantoms (not shown) and animal lymph nodes. In the latter images, in addition to melanoma cell distributions, we could also recognize absorbing structures reminiscent of trabeculae subdividing the node into follicles. In the animal lymph nodes spectral analysis showed highest contrast at 720 nm.

Further research is required to improve detection capability or limits. In the specific human lymph node studied, melanoma cells dominated the structure, precluding any necessity for the use of spectral analysis. However, situations are expected where absorption from other lymph node constituents are also present in images making melanoma detection challenging. Here a spectral discrimination approach based on the method demonstrated in Fig. 2 (f) will be necessary. Another issue is that image contrast and resolution may not be optimal due to differences in speed-of-sound between the lymph node, water and agar,. In future studies we will apply methods to correct for acoustic velocity (14,16). We will also acquire projections from multiple slices in depth to provide 3-D absorption distributions of the node. This 3-D data set will permit virtual biopsy by visualizing slices in various orientations. The method has potential in future embodiments to develop into a compact intra-operative imaging modality that can be used to assess the resected sentinel lymph nodes.

2.5 References

1. Jemal A, Siegel R, Xu J, Ward E. Cancer statistics, 2010. CA Cancer J Clin 2010; 60(5):277-300.
2. Ferlay J, Parkin DM, Steliarova-Foucher E. Estimates of cancer incidence and mortality in Europe in 2008. Eur J Cancer 2010; 46(4):765-781.
3. Breslow A. Thickness, cross-sectional areas and depth of invasion in the prognosis of cutaneous melanoma. Ann Surg 1970; 172(5):902-908.
4. Morton DL, Thompson JF, Cochran AJ, Mozzillo N, Elashoff R, Essner R, Nieweg OE, Roses DF, Hoekstra HJ, Karakousis CP, Reintgen DS, Coventry BJ, Glass EC, Wang HJ. Sentinel-node biopsy or nodal observation in melanoma. N Engl J Med 2006; 355(13):1307-1317.
5. van der Velde-Zimmermann D, Schipper ME, de Weger RA, Hennipman A, Borel Rinkes IH. Sentinel node biopsies in melanoma patients: a protocol for accurate, efficient, and cost-effective analysis by preselection for immunohistochemistry on the basis of Tyr-PCR. Ann Surg Oncol 2000; 7(1):51-54.
6. Sanki A, Uren RF, Moncrieff M, Tran KL, Scolyer RA, Lin HY, Thompson JF. Targeted high-resolution ultrasound is not an effective substitute for sentinel lymph node biopsy in patients with primary cutaneous melanoma. J Clin Oncol 2009; 27(33):5614-5619.
7. Stojadinovic A, Allen PJ, Clary BM, Busam KJ, Coit DG. Value of frozen-section analysis of sentinel lymph nodes for primary cutaneous malignant melanoma. Ann Surg 2002; 235(1):92-98.
8. Weight RM, Viator JA, Dale PS, Caldwell CW, Lisle AE. Photoacoustic detection of metastatic melanoma cells in the human circulatory system. Opt Lett 2006; 31(20):2998-3000.
9. Zharov VP, Galanzha EI, Shashkov EV, Khlebtsov NG, Tuchin VV. In vivo photoacoustic flow cytometry for monitoring of circulating single cancer cells and contrast agents. Opt Lett 2006; 31(24):3623-3625.

10. Oh JT, Li ML, Zhang HF, Maslov K, Stoica G, Wang LHV. Three-dimensional imaging of skin melanoma in vivo by dual-wavelength photoacoustic microscopy. J Biomed Opt 2006; 11(3):-.
11. Zhang C, Maslov K, Wang LV. Subwavelength-resolution label-free photoacoustic microscopy of optical absorption in vivo. Opt Lett 2010; 35(19):3195-3197.
12. Erpelding TN, Kim C, Pramanik M, Jankovic L, Maslov K, Guo Z, Margenthaler JA, Pashley MD, Wang LV. Sentinel lymph nodes in the rat: noninvasive photoacoustic and US imaging with a clinical US system. Radiology 2010; 256(1):102-110.
13. McCormack D, Al-Shaer M, Goldschmidt BS, Dale PS, Henry C, Papageorgio C, Bhattacharyya K, Viator JA. Photoacoustic detection of melanoma micrometastasis in sentinel lymph nodes. J Biomech Eng 2009; 131(7):074519.
14. Jose J, Willemink RGH, Resink S, Piras D, van Hespen JCG, Slump CH, Steenbergen W, van Leeuwen TG, Manohar S. Passive element enriched photoacoustic computed tomography (PER PACT) for simultaneous imaging of acoustic propagation properties and light absorption. Opt Express 2011; 19(3):2093-2104.
15. Zonios G, Dimou A, Bassukas I, Galaris D, Tsolakidis A, Kaxiras E. Melanin absorption spectroscopy: new method for noninvasive skin investigation and melanoma detection. J Biomed Opt 2008; 13(1):014017.
16. Manohar S, Willemink RGH, van der Heijden F, Slump CH, van Leeuwen TG. Concomitant speed-of-sound tomography in photoacoustic imaging. Appl Phys Lett 2007; 91(13):-.

CHAPTER 3

FIRST EXPERIENCES OF PHOTOACOUSTIC IMAGING FOR DETECTION OF MELANOMA METASTASES IN RESECTED HUMAN LYMPH NODES*

Excision and histological assessment of the first draining node (Sentinel Lymph Node) is a frequently used method to assess metastatic lymph node involvement related to cutaneous melanoma. Due to the time required for accurate histological assessment, nodal status is not immediately available to the surgeon. Hence, in case histological examination shows metastases, the patient has to be recalled to perform additional lymphadenectomy. To overcome these drawbacks we studied the applicability of photoacoustic tomographic imaging as an intra-operative modality for examining the status of resected lymph nodes.
In melanoma patients undergoing lymphadectomy for metastatic disease, six suspect lymph nodes were photoacoustically (PA) imaged using multiple wavelengths. Histopathologal examination showed three nodes without tumor cells (benign nodes) and three nodes with melanoma cells (malignant nodes). PA images were compared with histology and anatomical features were analyzed. In addition, PA spectral analysis was performed on areas of increased signal intensity. After correlation with histopathology, multiple areas containing melanoma cells could be identified in the PA images due to their increased response. Malignant nodes showed a higher PA response and responded differently to an increase in excitation wavelength than benign nodes. In addition, differences in anatomical features between the two groups were detected. Photoacoustic detection of melanoma metastases based on their melanin content proves to be possible in resected human lymph nodes. The amount of PA signal and several specific anatomical features seem to provide additional characteristics for nodal analysis. However, it is as yet preliminary to designate a highly accurate parameter to distinguish between malignant and benign nodes. We expect to improve the specificity of the technique with a future implementation of an adjusted illumination scheme and depth correction for photon fluence.

* This chapter has been published as: D. J. Grootendorst, J. Jose, M. W. Wouters, H. van Boven, J. Van der Hage, T.G. Van Leeuwen, W. Steenbergen, S. Manohar, T. J. M. Ruers, "First experiences of photoacoustic imaging for detection of melanoma metastases in resected human lymph nodes", Lasers in Surgery and Medicine, 44(7), p. 541, 2012

3.1 Introduction

The incidence of melanoma is increasing faster than any other cancer, with about 68,000 new cases diagnosed every year in the United States (1). A similar number was diagnosed each year in Europe in 2008 (2). When diagnosed early and appropriately excised, melanoma is a curable malignancy. However, mortality is high for patients with advanced disease with 1-year survival rates of about 40% (3).

Early stage melanoma is primarily treated by a wide surgical excision of the primary tumor followed by a sentinel lymph node (SLN) biopsy if the Breslow thickness of the melanoma exceeds 1 mm (4). Combined histopathological and immunohistochemcial assessment of the excised SLN(s) proves to be an accurate predictor of the pathological status of nodal basin and as a result patient survival (5). Once metastases are detected in the SLN(s) surgical intervention is continued in the form of a radical lymphadenectomy of the regional lymph node basin (5). Radical lymphadenectomy, however may lead to serious morbidity, such as lymphedema (2% to 18% of cases), pain (16% to 56%), impaired joint mobility (4% to 45%), and limb weakness (19% to 35%) and should therefore be avoided if no clinical reason is present (6).

The time required for histopathological preparation of the SLN is known to amount to 5 days (7) due to fixation and staining of the tissue. This implies that in case the SLN turns out to harbour tumor metastases, a second operation has to be scheduled for the additional lymphadenectomy. This two-step approach leads to additional patient discomfort, morbidity cost, and organizational distress (8). There is thus a requirement for an intra-operative nodal scanning technique to enable a fast analysis of the entire nodal volume, and ascertain metastatic involvement during the SLN procedure. A positive metastatic involvement of the SLN will directly lead to a lymphadenectomy, which can be carried out in the same session, avoiding the need for patient recall.

Photoacoustics (PA) is one of the techniques which has the potential to develop into such a fast intra-operative imaging modality. PA imaging relies on the detection of acoustic waves produced by the thermoelastic expansion of tissue following absorption of short pulsed laser illumination. This allows the mapping of endogenous tissue chromophores like hemoglobin and melanin (9,10) . PA retains a good spatial resolution at higher imaging depths compared to purely optical imaging, due to the decreased amount of ultrasound scattering in tissue (11-14). The components of a PA imaging system are relatively inexpensive compared to MRI and no ionizing radiation is required for image acquisition. Melanoma cells, harbouring high optical absorbing melanin particles, can thus potentially be detected using PA imaging without any additional labelling.

Several groups including our own have looked into various aspects of melanoma metastases detection using PA imaging. Nedosekin *et al* (15) showed with high speed photoacoustic flow cytometry that circulating human melanoma cells could be detected in real-time in a

mouse model. Capturing of the circulating melanoma cells using magnetic or gold nanoparticle labelling has shown to further improve the sensitivity of this technique (16,17). McCormack *et al* (18) showed elevated PA responses in canine lymph nodes inserted with melanoma cells. Recently, we demonstrated that tomographic imaging of melanoma cells inside a pig lymph node using NIR illumination is possible, and spectral analysis could be used to support the visual discrimination of such deposits (19). Further, we performed the first PA studies on human lymph nodes and showed that nodal outline, shape and size could be determined with accuracy using 532 nm (20), and the PA response could be correlated to the presence of melanoma (19). However, before PA detection of melanoma metastases could be translated into a clinical setting, more information should be obtained on how to distinguish metastatic nodes from benign and hyperplastic nodes.

In this study, we present our experiences on the use of PA imaging for the detection of nodal melanoma metastases, based on the scans of six resected human lymph nodes. Three nodes were found to be benign and three malignant after histopathological analysis. PA images are correlated to histological sections and anatomical features are identified. The traditionally described ultrasound morphologic features predictive of malignancy which are size >1 cm, a rounded shape and the absence of a notch with or without blood vessels (hilum) (21-23) are also taken into account. In addition, we analyse the use of multispectral imaging to distinguish malignant nodes from benign nodes and discuss some instrumental drawbacks of the present embodiment of this new approach. Eventually this knowledge should lead to the development of a new nodal analysis technique which could improve intra-operative decision making for sentinel lymph nodes.

3.2 Materials and Methods

3.2.1 Research Protocol

The experimental protocol to perform PA imaging of melanoma metastases in resected human lymph nodes was approved by the medical ethics committee of the Netherlands Cancer Institute (NKI). Patients were included into the study when they had to undergo a lymphadenectomy because of proven metastatic disease of the inguinal or axillary lymph node basin. In these patients lymphadenectomy was performed according to standard procedures. All patients consented to the approved protocol. After the lymphadenectomy procedure, one or two nodes were selected and excised for PA imaging. Nodes were selected without knowledge of their pathological status. The nodes were scanned photoacoustically and routine pathological examination was

subsequently performed by slicing each node in half and obtaining one slice from each half. Before further slicing, both halves were photographed to obtain an overview of the interior of some of the nodes. Tissue was stained using a normal haematoxylin and eosin (H&E) stain. Of the total of 6 imaged lymph nodes, 3 nodes proved to contain metastatic cells (malignant) after pathological analysis and 3 were labelled as benign.

3.2.2 Setup

The photoacoustic setup employed has been described earlier in detail (19) and consists of a Q-switched Nd:YAG laser (Brilliant B, Quantel, France) with an optical parametric oscillator (Opotek, 700 to 950 nm) operating at a 10 Hz repetition rate. Radiant exposure on the surface of the sample could be varied up to 40 mJ/cm^2. Samples were placed inside an Agar holder (Fig. 1) and light was directed to fall on top of the sample using a beam expander. The produced acoustic signals are recorded with the help of a curvilinear detector array (Imasonic, Besançon) consisting of 32 elements. The piezo elements of the detector have a central frequency of 6.25 MHz with a receiving bandwidth greater than 80% which results in an in-plane resolution of around 150 µm and a slice thickness of around 1 mm (24). The array is placed to detect sound in a plane orthogonal to the light beam and it rotates around the object to acquire a tomographic measurement.

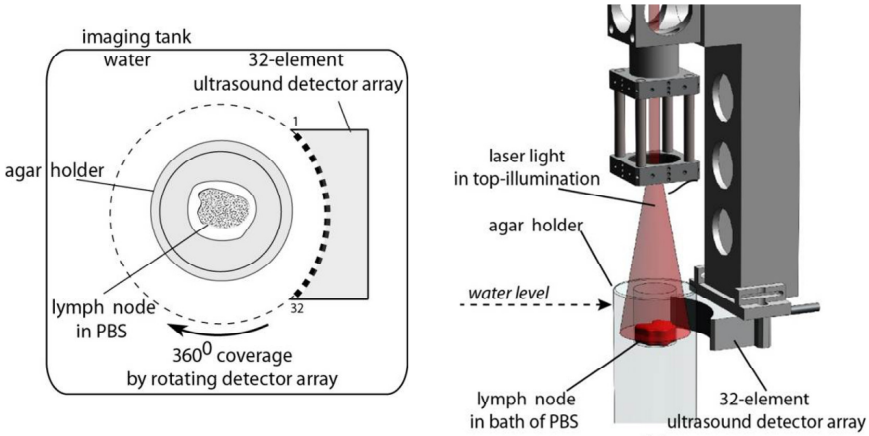

Fig. 1. Tomographic PA setup utilizing top illumination. The holder containing the lymph node is illuminated from the top while the ultrasound detector is rotated around the holder.

3.2.3 Imaging

Multispectral imaging can assist in the visualization of melanoma metastases due to differences in the optical absorption spectra of melanin and other biological chromophores like hemoglobin (19,25). We varied the illumination wavelength and obtained images of the resected nodes between 720 to 800 nm. In this range, hemoglobin shows a flat or increased absorption depending on its state while melanin absorption decreases with increasing wavelength.

Five sectional PA images in depth of each resected node were acquired to obtain an overview of each node. The PA images around the central plane of the node, in the results referred to as PA slices, were used for comparison with histology because this plane is closest to the histological sections made. Nodal dimensions were calculated from the histological slides and the PA images. In addition, the PA images were visually analyzed

with regard to their shape and the presence of a hilum. All nodes were imaged using several different excitation wavelengths as displayed in Table 2. Energy was varied depending on the size of the node in order to approach an equal fluence in moderate and thicker samples.

To quantify the amount of PA response at each illumination wavelength, we calculated the Average Pixel Values (APV) at selected regions of interest within the image. Regions of interest in the PA images were selected according to the amount of PA response and the results of histopathology. Interpolation was used for missing excitation wavelength information. Values of both benign and malignant nodes were normalized for the energy input (Table 2), plotted and compared.

3.3 Results

We present all results of the studied lymph nodes, subdivided according to dignity of the node, malignant (nodes 1-3) or benign (nodes 4-6), as known from histopathology. A combination of the PA images at 720 nm, histological, and overview photographs of the malignant and benign nodes is displayed in Figure 2 and 3. Table 1 displays the maximum diameter of each node measured in both the PA images and histopathology.

3.3.1 Imaging malignant lymph nodes

Node 1 features a darkened appearance and included some additional fat (Fig. 2D). The PA slice (Fig. 2B) obtained in the central plane at a depth of approximately 3 mm, shows a pronounced nodal outline which lacks a clear bean shape and appears more rounded. No clear hilum could be located. Most contrast is located in the nodal outline while most of the nodal interior shows low PA response. An area of increased response is located at two o'clock containing a diameter of 0.7 cm (green arrow). Pathology shows the presence of melanoma throughout the entire node with large quantities of melanin present in an area corresponding in dimension to the area of photoacoustic signal increase at two o'clock (Fig. 2C). The larger melanin deposits in the lower part of the node could not be retrieved within the PA map (blue arrow).

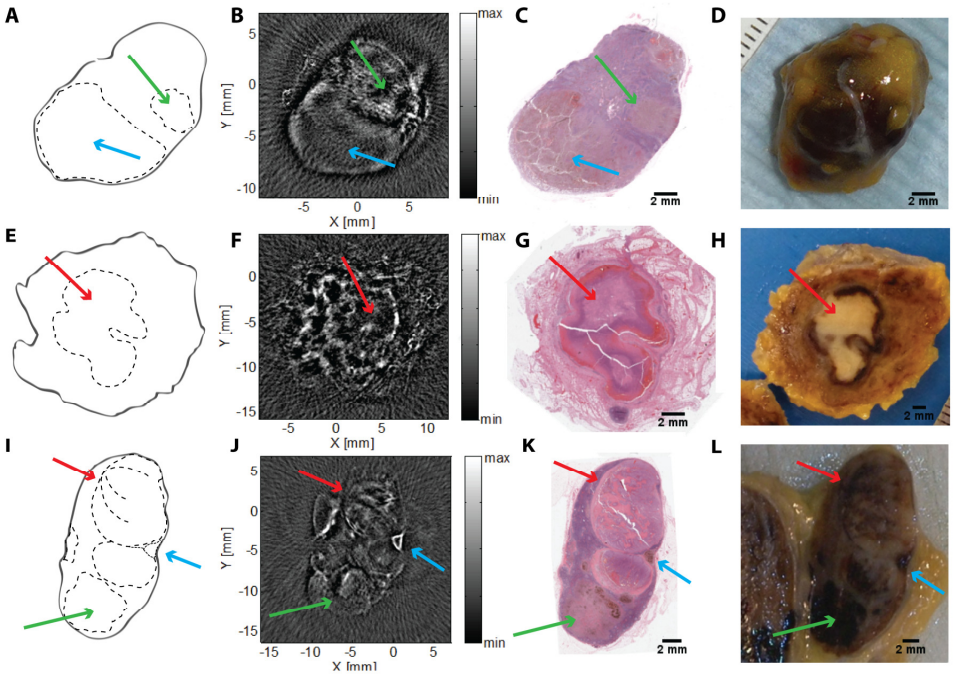

Fig. 2. PA images of malignant nodes at 720 nm. Color scales are optimized to display the identified features. A, E, and I: Layout of the visualized structures within each node based on contour of the histopathological images (C, G, and K). B: PA image of lymph node 1.Contrast is increased throughout the upper part of the node and a small area around 2 O'clock shows an increased response (green arrow). C: Corresponding pathological slice. Melanoma cells present throughout the node, especially at 2 O'clock and 7 O'clock. D: Corresponding photograph of unsliced node. F: PA image of lymph node 2. Slice shows a ring of increased contrast located around the unenhanced centre of the node (red arrow). G: Corresponding pathological slice. Melanoma cells are located around a necrotic centre (red arrow) H: Corresponding photograph of the sliced node before staining. Diffuse darkening of the nodal volume which contains a large necrotic area surrounded by a dark ring of melanoma cells (red arrow). J: PA image of lymph node 3. A small triangle of increased response is located at 3 O'clock (blue arrow) and some ring like response patterns can be distinguished at 12 O'clock (red arrow). K: Corresponding pathological slice showing a triangular melanin rich area at 3 O'clock (blue arrow) and some additional vital melanoma cells in curved patterns grouped around and throughout the necrotic center at 12 O'clock (red arrow). L: Corresponding photograph of the sliced node before staining. Dark triangular area at 3 O'clock is distinguishable (blue arrow) and ring like patterns in the upper part of the node are visible (red arrow).

Node 2 showed no clear darkening after excision and contained only small quantities of extra nodal fat. The PA slice (Fig. 2F) in the nodal plane taken at a depth of 5 mm shows an increase in signal at different locations heterogeneously throughout the node with an exception of the nodal center. Surrounding the area lacking PA response (red arrow) is a small ring of increased signal. No clear nodal outline or hilum could be detected although nodal features seemed to be more rounded compared to the PA images of the benign nodes (Fig. 3A and 3G). The photograph of the sliced node taken before pathological analysis (Fig. 2H) shows diffuse darkening throughout the node together with a small dark ring surrounding a large necrotic area in the center of the node (red arrow). Shape of both the dark ring and the light colored necrotic area, correlate to the area respectively containing and lacking photoacoustic response (red arrow). Pathology confirms the presence of viable melanoma cells in the periphery of the necrotic area. (Fig. 2G). The shape of the necrotic area correlates with both the photograph and the PA image.

Node 3 features some darkening throughout the entire nodal surface with some deposits of extranodal fat after excision. The PA slice (Fig. 2J) around the central plane obtained at a depth of 4 mm did show a traceable nodal outline and locations of increased signal intensity. Absence of a clear bean shaped outline proved hard to deduce and no hilum could be located. Absorption at all wavelengths was most pronounced at three o'clock corresponding with a relatively small area (blue arrow). The area located at three o'clock displays a pronounced triangular shape, lacking PA contrast in its center. The photograph taken before pathological analysis (Fig. 2L) shows a node which contains several areas of pronounced darkening primarily located from three to nine o'clock. Located at three o'clock is a small triangular area corresponding in location, shape and size with the area of increased signal intensity in the photoacoustic image (blue arrow). A curved ray like PA intensity pattern (Fig. 2J) is noted in the upper area of the node which resembles the curved ray like structures in the photograph (red arrows). The larger darkened area at six o'clock (green arrow) did not show up clearly in the PA images although some signal was detected at this location. Histology (Fig. 2K) confirms the presence of melanoma throughout the node with larger melanin deposits in the lower areas of the node. Especially the triangular location at three o'clock and larger areas around five and six o'clock seem to include large quantities of melanin. The upper region of the node contains two distinct necrotic areas (light purple staining) which still contain some viable melanoma cells in their center and outer rings. These patterns correspond with the curved ray like patterns of our photographs and the detectable PA rings at twelve o'clock (red arrow).

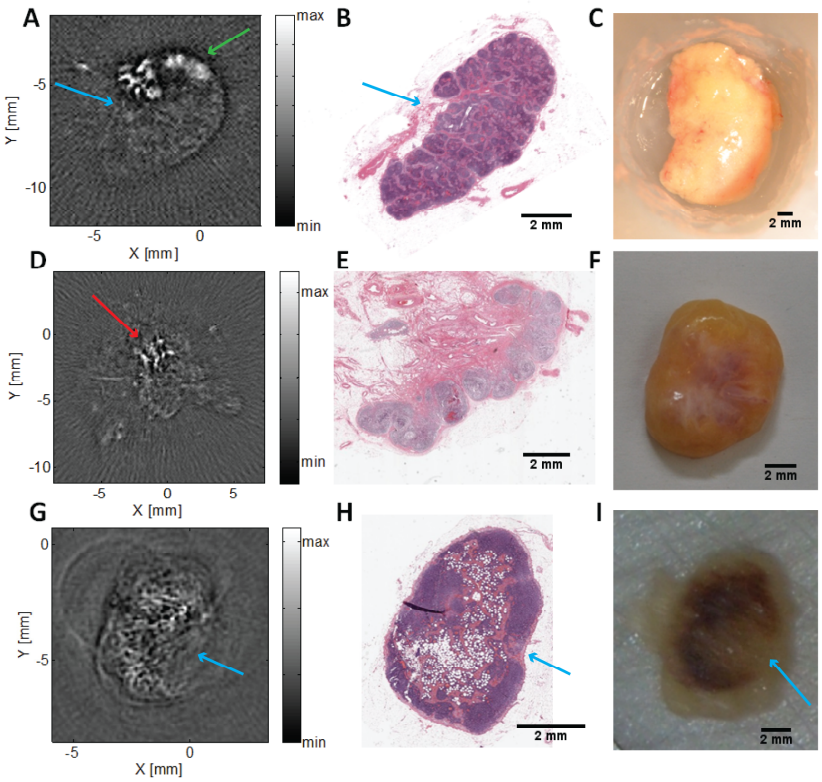

Fig. 3. PA images of benign nodes at 720 nm. Color scales are optimized to display the identified features. A: PA image of lymph node 4. Contrast is increased in the upper part of the node (green arrow) and a slight notch indicating the hilum can be seen at 10 O'clock (blue arrow). B: Corresponding pathological slice. Hilum location correlates to PA image (blue arrow). C: Corresponding photograph of unsliced node. D: PA image of lymph node 5. Slice shows a speckle pattern which is most intense in the centre of the image (red Arrow). E: Corresponding pathological slice. F: Corresponding photograph of unsliced node. G: PA image of lymph node 6. Notch around 4 O'clock resembles hilum location (blue arrow). H: Corresponding pathological slice showing hilum location (blue arrow). I: Corresponding photograph of the sliced node before staining. Darkening throughout the tissue resembles PA shape. Hilum is located at 4 O'clock (blue arrow).

3.3.2 Imaging benign lymph nodes

Node 4 showed no significant discolouring and contained some accessory fat after excision (Fig. 3C). The PA slices taken in the central plane at a depth of 3 mm (Fig. 3A) show a well defined nodal outline which resembles a bean shape and shows a pronounced hilum at ten o'clock (blue arrow). A speckled high contrast area (green arrow) is located at twelve o'clock. Pathology shows that the node contains reactive changes, however, no malignant cells were present in the specimen (Fig. 3B).

Node 5 did not show any discolouring but showed significant quantities of accessory fat after excision (Fig. 3F). In the PA slice at the central plane (2 mm beneath the surface) (Fig. 3D) the nodal outline proved hard to distinguish and the nodal diameter could therefore not be determined with accuracy. In addition, no defined hilum could be located. Most signal is located in the centre of the image showing a diffuse speckle pattern (red arrow). Pathological examination shows reactive changes throughout the node with absence of malignant cells (Fig. 3E).

Table 1. Lymph node sizes

#	Maximum diameter in histology (mm)	Maximum diameter in PA image (mm)
1	17	15
2	17	17
3	20	20
4	9	7
5	10	11
6	6	7

Node 6 showed some discolouring and contained minor deposits of accessory fat after excision. PA images show a distinct nodal outline which is bean shaped (Fig. 3G) and the inclusion of a hilum (blue arrow) can be located at four o'clock. PA response is located throughout the entire nodal volume, although fluctuations are present in some locations. The photograph taken before pathological analysis (Fig. 3I) shows a fatty dark node which contains a hilum at four o'clock (blue arrow). Pathological examination (Fig. 3H, 4C) reveals that the node contains some fatty deposits and includes a lot of red blood cells inside several vessels explaining the darkened color. Malignant cells are not observed.

Table 2. Photoacoustic imaging parameters

#	Energy (mJ/cm^2)*	Wavelengths (nm)■	Projections●
1	30	720-760-800	20
2	30	720-740-760-780-800	20
3	40	720-740-760-780-800	40
4	25	720-760-800	20
5	25	720-760-800	20
6	25	720-760-800	20

* Energy was varied depending on the size of the node
■ Additional excitation wavelengths were used to more accurately define the PA response of the different structures within the node
● Additional projections were taken depending on the quality of the image

3.3.3 Multispectral analysis

The added potential benefit of multiple wavelength illumination is shown in node 6 (Fig. 4). The images obtained at 800 nm show a vessel like structure leaving the nodal hilum which could not be visualized using 720 nm (Fig. 4A-B, red arrow). Pathological examination revealed the presence of a blood vessel at this location (Fig. 4D, red arrow). The response inside the vessel depicted in node 6 (Fig. 4B, red arrow) proved to be increased, pointing to the presence of oxidized hemoglobin, however this trend was not measured in the rest of the nodal volume.

Spectral analysis was performed on the areas within each node containing most pronounced PA responses. For node 1-3 these areas were respectively the area at two o'clock (green arrow), the ring around the necrotic center of the node containing viable melanoma cells (red arrow) and the area at three o'clock (blue arrow). For node 4-6, spectral analysis was respectively performed on the region at twelve o'clock (green arrow), the centre of the image (red arrow) and the entire area within the nodal outline.

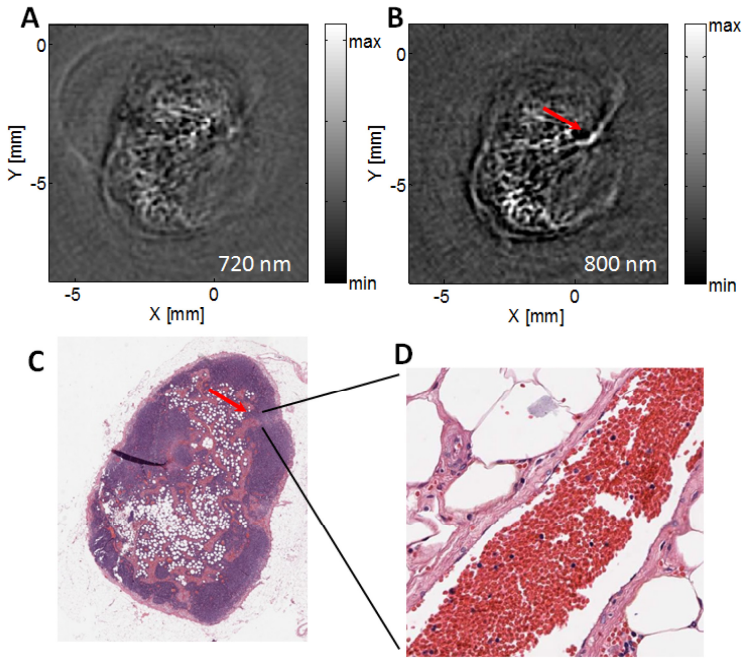

Fig. 4. A: Lymph node 6. Map of the PA response within the lymph node at 720 nm. PA response is present throughout the node, however no vessel like structures are visible. B: Map of the PA response within the lymph node at 800 nm. PA response is present throughout the node and a vessel like structure is located in the upper right (red arrow). C: Pathological overview of the node. Slice shows a fatty node without malignant cells. D: Amplification reveals red blood cells in a small vessel exiting the node boundary.

Figure 5 displays the multiple wavelength response of the selected areas within the nodes and shows that the PA response in the selected regions within the malignant nodes is larger than those within the benign ones. All nodes show most PA signal at 720 nm but the measured APVs within the malignant nodes show a larger decrease up to 800 nm than those within the benign nodes. Although node 3 shows a higher APV than the benign nodes, its decrease in APV up to 800 nm is less pronounced compared to node 1 and 2.

3.4 Discussion and Conclusions

As shown by our PA scans of six human lymph nodes, detection of melanoma cells in resected human lymph nodes proves to be possible using photoacoustics. In all three malignant nodes an increased PA response in the images could be correlated to the presence of melanoma cells verified by histopathology. This is the first study on both malignant and benign resected human samples demonstrating differences in PA response. However, it should be noticed that not all metastatic areas detected on histology could be visualized with PA. This could be attributed to the biological diversity of the metastases and their melanin content or the lack of optical penetration due to the optical thickness of malignant tissue.

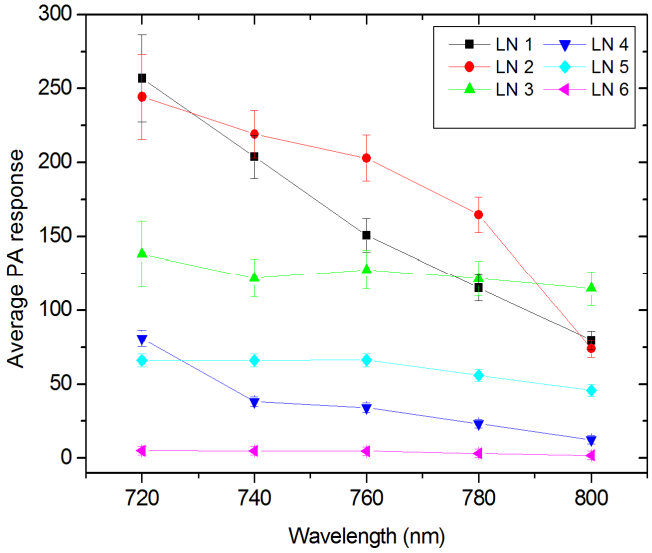

Fig. 5. Average pixel values (APVs) of the selected areas within the lymph nodes (LN) at different illumination wavelengths.

In our understanding, the latter contributes most to this decreased detection rate since the optical density of the melanin-rich (malignant) tissue impedes imaging more than 5 mm beneath the nodal surface. This is shown in the PA image of lymph node 1 where the nodal outline is enhanced while the PA response in the center of the node is less pronounced. As the photographs of the malignant nodes show, their tissue is slightly discoloured and in node 1 even severely darkened which produces an increased optical density compared to normal or reactive nodal tissue. An improved illumination scheme, providing light from different angles onto the nodal volume could be useful to ensure that sufficient optical energy reaches the inner parts of the node. At the moment these adjustments are implemented and evaluated. It has to be mentioned that our final application purpose of

scanning resected nodes during surgery does not require the scanning of nodes larger than 1-1.5 cm because it is already relatively certain that they harbour metastases. Loss of sensitivity due to illumination problems is therefore less likely to arise once the technique is used within a patient population which contains less pronounced nodal metastases, such as sentinel lymph nodes.

In the benign cases, a PA response was also noted but these were considerably weaker than in the malignant nodes, as shown by the APV (Fig. 5). Most likely, this PA reponse can be attributed to the presence of hemoglobin which could be present in small vessels or haemorrhages throughout the nodes. Other biological components like collagen and fat show minor absorption in the NIR range (11), and are therefore not suspected of generating this amount of response. In addition, during surgical resection of the lymph nodes, small blood vessels in the extranodal fat of the node may be disrupted causing little haemorrhages in the perinodal fat. Though the nodes were placed in PBS during transport and washed before imaging, some small blood deposits could have remained leading to a PA signal.

The use of multispectral imaging was however not able to verify that all PA response within the benign nodes could be attributed to hemoglobin, and the spectra did not point to the presence of one specific other chromophore. The fact that the exact blood content and state is unknown in an ex-vivo sample makes it more difficult to verify the exact origin of the signal. In addition, since all samples differ in size and there is a significant variability in the scattering and absorption components between the tissues, it is challenging to compensate for the optical attenuation difference between the wavelengths at different depths within the sample. The APV's normalized for the laser input energy in malignant nodes prove to be higher than those in benign nodes and their drop towards 800 nm seems to be larger. Although the fluence within each sample may have differed, these characteristics could possibly function as additional indicators for metastatic presence. To improve spectral unmixing in future experiments, the implementation of algorithms to correct for light attenuation (26-28) and speed-of-sound inhomogeneities (29), could prove helpful. Further, optical spectroscopy could be used to obtain more knowledge on the exact content of malignant and benign nodal tissue (30).

Next to the use of multi-spectral imaging, anatomical nodal characteristics could possibly be taken into account to increase the distinctive power of the technique. Ultrasound features described as being indicators for metastatic presence, namely increased nodal size, lack of bean shape and the absence of a hilum, could possibly be used to this end. The correlation between measured maximum diameters in the PA images and histology (Table 1) shows that PA is able to produce an accurate depiction of nodal size even when the node is embedded in additional layers of fatty tissue. The PA images (Fig. 2-3) show that all metastatic nodes measure more than 10 mm while only one of the benign nodes shows an enlarged size. In addition, the contours of two of the malignant nodes seemed more rounded

while two of the benign nodes possessed a detectable bean like contour and hilum. The fact that node 2 and 4 lacked a clear nodal outline made the identification of nodal features difficult in these cases which offers some explanation why not all nodes complied with the predictive ultrasound features. Additional imaging using a wavelength of 532 nm could have enhanced these features as we have shown earlier (20). Unfortunately, this excitation wavelength was not available in our present set up but will be taken into account in future experiments. Nodal hilum identification may further be improved by the detection of blood vessels leaving or entering the nodal outline. The use of 800 nm illumination could improve the identification of these structures as shown in Fig. 4. We emphasize that the absence of these features does not fully exclude the possibility of the node harbouring (micro) metastases (31) and these external characteristics can therefore only function as an additional analysis tool.

In general, we can conclude that the detection of melanoma metastases in resected human lymph nodes can be performed using photoacoustics, however a highly accurate parameter to distinguish between malignant and benign nodes is at this point, at the present embodiment of the technique, challenging to define. The amount of PA signal seems to provide an indication for malignancy although the PA signal generated in benign nodes could not be linked to a specific biological chromophore. By paying attention to additional nodal features like shape and size, the distinctive capability of the technique could possibly be increased. Multiple angle illumination could furthermore ensure homogeneous imaging of optically dense or larger samples and application of spectral unmixing algorithms could facilitate a more accurate analysis. To include the use of more excitation wavelengths, we are taking steps towards the implementation of higher sensitivity detectors to reduce the scanning time and the addition of a wavelength-dependent fluence corrections algorithm. A larger photoacoustic study of melanoma metastases will shed more light on the influence of the biological diversity, and the role photoacoustics can play in accurately identifying metastases on the basis of these characteristics.

3.5 References

1. Rigel DS. Epidemiology of melanoma. Semin Cutan Med Surg 2010; 29(4):204-209.
2. Ferlay J, Parkin DM, Steliarova-Foucher E. Estimates of cancer incidence and mortality in Europe in 2008. Eur J Cancer 2010; 46(4):765-781.
3. Edge SB, Compton CC. The American Joint Committee on Cancer: the 7th edition of the AJCC cancer staging manual and the future of TNM. Annals of surgical oncology 2010; 17(6):1471-1474.
4. Breslow A. Thickness, cross-sectional areas and depth of invasion in the prognosis of cutaneous melanoma. Ann Surg 1970; 172(5):902-908.
5. Morton DL, Thompson JF, Cochran AJ, Mozzillo N, Elashoff R, Essner R, Nieweg OE, Roses DF, Hoekstra HJ, Karakousis CP, Reintgen DS, Coventry BJ,

Glass EC, Wang HJ. Sentinel-node biopsy or nodal observation in melanoma. N Engl J Med 2006; 355(13):1307-1317.
6. Abe H, Schmidt RA, Sennett CA, Shimauchi A, Newstead GM. US-guided core needle biopsy of axillary lymph nodes in patients with breast cancer: Why and how to do it. Radiographics 2007; 27:S91-S99.
7. van der Velde-Zimmermann D, Schipper MI, de Weger RA, Hennipman A, Rinkes IHMB. Sentinel node biopsies in melanoma patients: A protocol for accurate, efficient, and cost-effective analysis by preselection for immunohistochemistry on the basis of Tyr-PCR. Annals of Surgical Oncology 2000; 7(1):51-54.
8. Wrightson WR, Wong SL, Edwards MJ, Chao C, Reintgen DS, Ross MI, Noyes RD, Viar V, Cerrito PB, McMasters KM, Grp SMTS. Complications associated with sentinel lymph node biopsy for melanoma. Annals of Surgical Oncology 2003; 10(6):676-680.
9. Yao J, Wang LV. Photoacoustic tomography: fundamentals, advances and prospects. Contrast Media & Molecular Imaging 2011; 6(5):332-345.
10. Piras D, Xia W, Steenbergen W, van Leeuwen TG, Manohar S. Photoacoustic imaging of the breast using the twente photoacoustic mammoscope: present status and future perspectives. Selected Topics in Quantum Electronics, IEEE Journal of 2010(99):1-10.
11. Beard P. Biomedical photoacoustic imaging. Interface Focus 2011; 1(4):602-631.
12. Razansky D, Buehler A, Ntziachristos V. Volumetric real-time multispectral optoacoustic tomography of biomarkers. Nat Protoc 2011; 6(8):1121-1129.
13. Telenkov SA, Mandelis A. Photothermoacoustic imaging of biological tissues: maximum depth characterization comparison of time and frequency-domain measurements. J Biomed Opt 2009; 14(4):044025.
14. Grun H, Berer T, Burgholzer P, Nuster R, Paltauf G. Three-dimensional photoacoustic imaging using fiber-based line detectors. J Biomed Opt 2010; 15(2):021306.
15. Nedosekin DA, Sarimollaoglu M, Ye JH, Galanzha EI, Zharov VP. In vivo ultra-fast photoacoustic flow cytometry of circulating human melanoma cells using near-infrared high-pulse rate lasers. Cytometry A 2011; 79(10):825-833.
16. Galanzha EI, Shashkov EV, Kelly T, Kim JW, Yang L, Zharov VP. In vivo magnetic enrichment and multiplex photoacoustic detection of circulating tumour cells. Nat Nanotechnol 2009; 4(12):855-860.
17. McCormack DR, Bhattacharyya K, Kannan R, Katti K, Viator JA. Enhanced photoacoustic detection of melanoma cells using gold nanoparticles. Lasers Surg Med 2011; 43(4):333-338.
18. McCormack D, Al-Shaer M, Goldschmidt BS, Dale PS, Henry C, Papageorgio C, Bhattacharyya K, Viator JA. Photoacoustic Detection of Melanoma Micrometastasis in Sentinel Lymph Nodes. J Biomech Eng-T Asme 2009; 131(7).
19. Jose J, Grootendorst DJ, Vijn TW, Wouters M, van Boven H, van Leeuwen TG, Steenbergen W, Ruers TJ, Manohar S. Initial results of imaging melanoma metastasis in resected human lymph nodes using photoacoustic computed tomography. J Biomed Opt 2011; 16(9):096021.
20. Grootendorst D, Jose J, Van der Jagt P, Van der Weg W, Nagel K, Wouters M, Van Boven H, Van Leeuwen TG, Steenbergen W, Ruers T, Manohar S. Initial

experiences in the photoacoustic detection of melanoma metastases in resected lymph nodes. Proc Spie 2011; 7899.
21. Gill KR, Ghabril MS, Jamil LH, Hasan MK, McNeil RB, Woodward TA, Raimondo M, Hoffman BJ, Hawes RH, Romagnuolo J. Endosonographic features predictive of malignancy in mediastinal lymph nodes in patients with lung cancer. Gastrointestinal endoscopy 2010; 72(2):265-271.
22. Catalano MF, Sivak MV, Rice T, Gragg LA, Vandam J. Endosonographic Features Predictive of Lymph-Node Metastasis. Gastrointestinal Endoscopy 1994; 40(4):442-446.
23. Kelly S, Harris K, Berry E, Hutton J, Roderick P, Cullingworth J, Gathercole L, Smith M. A systematic review of the staging performance of endoscopic ultrasound in gastro-oesophageal carcinoma. Gut 2001; 49(4):534-539.
24. Jose J, Willemink RG, Resink S, Piras D, van Hespen JC, Slump CH, Steenbergen W, van Leeuwen TG, Manohar S. Passive element enriched photoacoustic computed tomography (PER PACT) for simultaneous imaging of acoustic propagation properties and light absorption. Opt Express 2011; 19(3):2093-2104.
25. Petrova IY, Petrov YY, Esenaliev RO, Deyo DJ, Cicenaite I, Prough DS. Noninvasive monitoring of cerebral blood oxygenation in ovine superior sagittal sinus with novel multi-wavelength optoacoustic system. Opt Express 2009; 17(9):7285-7294.
26. Rosenthal A, Razansky D, Ntziachristos V. Quantitative Optoacoustic Signal Extraction Using Sparse Signal Representation. Ieee T Med Imaging 2009; 28(12):1997-2006.
27. Shao P, Cox B, Zemp RJ. Estimating optical absorption, scattering, and Grueneisen distributions with multiple-illumination photoacoustic tomography. Appl Opt 2011; 50(19):3145-3154.
28. Jetzfellner T, Razansky D, Rosenthal A, Schulz R, Englmeier KH, Ntziachristos V. Performance of iterative optoacoustic tomography with experimental data. Appl Phys Lett 2009; 95(1).
29. Schoonover RW, Anastasio MA. Image reconstruction in photoacoustic tomography involving layered acoustic media. J Opt Soc Am A Opt Image Sci Vis 2011; 28(6):1114-1120.
30. Kanick SC, van der Leest C, Djamin RS, Janssens AM, Hoogsteden HC, Sterenborg HJCM, Amelink A, Aerts JGJV. Characterization of mediastinal lymph node physiology in vivo by optical spectroscopy during endoscopic ultrasound-guided fine needle aspiration. Journal of Thoracic Oncology 2010; 5(7):981.
31. Catalano MF, Sivak Jr MV, Rice T, Gragg LA, Van Dam J. Endosonographic features predictive of lymph node metastasis. Gastrointestinal endoscopy 1994; 40(4):442-446.

CHAPTER 4

EVALUATION OF SUPERPARAMAGNETIC IRON OXIDE NANOPARTICLES (ENDOREM®) AS A PHOTOACOUSTIC CONTRAST AGENT FOR INTRA-OPERATIVE NODAL STAGING*

Detection of tumor metastases in the lymphatic system is essential for accurate staging of malignancies. Commercially available superparagmagnetic nanoparticles (SPIOs) accumulate in normal lymph tissue after injection at a tumor site, whereas less or no accumulation takes place in metastatic nodes, thus enabling lymphatic staging using MRI. We verify for the first time the potential of SPIOs, such as Endorem® as a novel photoacoustic (PA) contrast agent in biological tissue.We injected five Wistar rats subcutaneously with variable amounts of Endorem® and scanned the resected lymph nodes using a tomographic PA setup. Findings were compared using histology, vibrating sample magnetometry (VSM) and 14 T MR-imaging. Our PA setup was able to detect the iron oxide accumulations in all the nodes containing the nanoparticles. The distribution inside the nodes corresponded with both MRI and histological findings. VSM revealed that iron quantities inside the nodes varied between 51±4 and 11±1 μg. Nodes without SPIO enhancement did not show up in any of the PA scans. Iron oxide nanoparticles (Endorem®) can be used as a PA contrast agent for lymph node analysis and a distinction can be made between nodes with and nodes without the agent. This opens up possibilities for intra-operative nodal staging for patients undergoing nodal resections for metastatic malignancies.

* This chapter has been published as: D. J. Grootendorst, J. Jose, R. M. Fratila, M. Visscher, A.H. Velders, B. Ten Haken, T.G. Van Leeuwen, W. Steenbergen, S. Manohar, T. J. M. Ruers, "Evaluation of superparamagnetic iron oxide nanoparticles (Endorem®) as a photoacoustic contrast agent for intra-operative nodal staging", Contrast Media & Molecular Imaging, 44(7), p. 541, 2012

4.1 Introduction

Photoacoustic (PA) imaging is a hybrid imaging modality, whose ability to provide functional imaging based on physiological parameters has resulted in widespread acceptance in biomedical research applications ranging from tumor detection to cerebral hemodynamic analysis (1). PA imaging relies on the detection of acoustic waves produced by the thermoelastic expansion of tissue following absorption of short pulsed illumination.

The method combines the excellent absorption contrast achieved in optical techniques with the high spatial resolution of ultrasound imaging (2). Since biological chromophores like melanin and hemoglobin are strong optical absorbers, PA imaging provides the possibility for non-invasive imaging of these chromophores *in vivo*. The strong PA response of these chromophores enables the detection of melanoma cells (3,4) and melanoma metastases (5,6) or visualization of the vasculature associated with breast carcinoma (7) without the addition of extrinsic contrast. However, biological processes that lack an intrinsic chromophore related to a disease state, including many malignancies, would require the addition of extrinsic contrast for its detection. PA imaging, owing to its lack of ionizing radiation and fast imaging performance, could develop into an additional medical imaging method once a specific and biocompatible PA contrast agent was available.

Research into PA extrinsic contrast strategies has been going on for several years in both *in vitro* and i*n vivo* models (8). Research is focused predominantly on the use of nanoparticles including gold nanorods, gold nanoshells and carbon nanotubes (9-12). Yang et al. showed that gold nanocages can be used to map sentinel lymph nodes (13) and enhance the optical absorption in the cerebral cortex of mice (14), while De La Zerda demonstrated that tumors in mice can be enhanced and imaged *in vivo* using antigen coupled single-walled carbon nanotubes (15). These newly developed particles show great potential to enhance contrast with regard to several pathological problems, including cancer. However almost all of these contrast agents are still in the experimental stage, and few clinical studies have been initialized in recent years. At this point, it is as yet uncertain if these particles will obtain clearance by the Food and Drugs Administration (FDA) and the European Medicines Agency (EMA) in the near future. Recent studies with gold nano shells (16,17) have led to the initiation of a clinical trial using gold nano shells as photo-induced hyperthermia agents for cancer therapy in patients with oropharyngeal malignancies; however it may take several years to acquire all of the results.

A PA contrast agent that has already been clinically established would require a less extensive follow-up, facilitating a fast implementation in the clinic. With respect to extrinsic contrast enhancement, magnetic resonance imaging (MRI) is one of the areas that have seen major developments in the recent years. In 1989, Weissleder *et al.* (18) used dextran-coated superparamagnetic iron oxide (SPIO) nanoparticles for nodal contrast enhancement in MRI. After subcutaneous administration of 20 mmol/kg SPIO in the

footpad of healthy and tumor-bearing rats, it was shown that non-metastatic nodes appeared dark in MR images while the metastatic nodes appeared iso- or hyperintense. This image contrast difference is based on the selective uptake of the nanosized particles in non-metastatic nodes by the process of phagocytosis by macrophages (19). After subcutaneous injection, SPIOs are cleared by draining lymphatic vessels and transported to the regional lymph nodes where they are phagocytosed by nodal macrophages in a scavenger receptor-mediated endocytosis pathway (20,21). In MRI, locations containing SPIOs then show upas areas of reduced signal intensity because of the magnetic susceptibility of the particles. If metastases cause disturbances in node flow or displace nodal macrophages, the uptake of SPIOs inside the node is decreased and the node will contain lessiron oxide appearing iso- or hyperintense. Most importantly, the inhomogeneities in the MRI contrast patterns within the node are shown to correlate with the locations of metastatic deposits, enabling staging on the outlook of the SPIO distribution within a node. The oncologist's decision to use neoadjuvant therapy or the surgeon's decision to perform nodal dissection is influenced by the presence or absence of lymphatic metastases and therefore the use of SPIOs to improve pre-operative nodal staging has been extensively researched. Coated iron oxide nanoparticles have been found to contain a satisfactory safety profile for human applications (22) and, as a result, several iron oxide dispersions have been cleared for clinical use. Preoperative nodal staging for different malignancies is known to benefit from the use of these dispersions (23-26).

Our work regarding the detection of melanoma metastases in resected human lymph nodes proved that metastases could be visualized using PA imaging (5,6). However, while melanoma metastases contain melanin, a strong optical absorber, other malignancies spread across the lymphatic system without such an intrinsic chromophore. The fact that SPIOs could function as nodal staging agents, possess large optical cross-sections (27) and proved to be photoacoustically detectable in phantoms (28), prompted us to study these particles. We investigated the PA contrast potential of iron oxide nanoparticles using an animal model to explore the possibilities of detecting the accumulated nodal deposits of these particles after subcutaneous injection. The detection of these deposits could allow for resected lymph nodes to be photoacoustically scanned for metastatic involvement in the operation theatre, saving time and possibly preventing the recall of a patient for an additional operation, a concept also explored by other optical techniques like optical coherence Tomography (29) and Raman spectroscopy (30).

4.2 Materials and Methods

4.2.1 Iron Oxide Nanoparticles

We used the commercially available SPIO agent Endorem® (Guerbet, Villepinte, France) (Fig. 2A), comprising iron oxide nanoparticles (11.2 mg/ml) dispersed in water. The particles are composed of several iron oxide cores (diameter 4–6 nm) embedded inside a

dextran coating (31). Particles have an estimated hydrodynamic size of 80–150nm (32). Dilutions were prepared using sterile phosphate buffered saline (PBS).

4.2.2 Animals

A rodent model was implemented to mimic the human lymphatic situation. The animal research protocol was approved by the animal ethics committee of the University Medical Center Utrecht. Five mature female Wistar rats, weighing approximately 250–300 g were housed at the animal facility of the University of Twente and fed according to normal procedures, including grouped housing, nesting material and free access to food and water. Swelling of the lymph nodes, required to obtain a nodal volume that could be easily resected and imaged, was achieved by a subcutaneous injection of 0.1 ml of incomplete Freund adjuvant (IFA) (33) inside both footpads of the hind legs. IFA is composed of a water in oil emulsion and functions as immunopotentiator to achieve macrophage activation and immune cell multiplication, leading to an increase in lymph node size. In addition, in a future clinical situation nodes are likely to show tumor induced reactive lymphadenopathy which, according to Klerkx et al. (34), can be mimicked using IFA. The use of IFA will therefore result in an immune response that more closely resembles the lymphatic system in oncology patients.

After 7 days, a significant increase in size was achieved and the animals were subcutaneously injected with 0.1 ml of the SPIO contrast agent in one or both footpads of the hind legs. The animals were euthanized by cervical dislocation 24 h after injection and the popliteal lymph nodes of both legs were excised. Once excised, all lymph nodes were photographed and placed inside a PBS solution. PBS prevented swelling of the tissue owing to water inflow and ensured proper PA imaging of the nodal volume over time. Weissleder *et al.* (18) subcutaneously injected approximately 3.2 mg iron oxide in their initial study in rats to verify the potential of the nanoparticle agent. In order to find out if PA detection of the nodes could be done with smaller SPIO concentrations, we also administered several dilutions of the Endorem® stock solution. The five animals were subcutaneously injected in the following way:

1. In one animal no contrast agent was injected (control).
2. In two animals undiluted (1.12mg iron oxide) Endorem® was injected in the left footpad.
3. In one animal both footpads were injected with a 2x dilution (0.56 mg iron oxide).
4. In one animal both footpads were injected with a 4x dilution (0.28 mg iron oxide).

A total of 10 lymph nodes were included in the study of which six were suspected of containing iron oxide nanoparticles (contrast nodes) and four were not (control nodes).

4.2.3 PA imaging

Resected nodes were placed inside a hollow transparent 3% Agar sample holder with an inner diameter of 25mm and wall thickness of 10 mm. The sample holder was placed in the center of a large water container where it was illuminated from the top. The detector was placed orthogonal to the light illumination and rotated around the object to acquire a tomographic measurement. While details of the instrument have been presented earlier (35), we describe here the essentials. The PA setup (Fig. 1) consists of a Q-switched Nd:YAG laser (Brilliant B, Quantel, France) with an optical parametric oscillator (Opotek, 700–950nm) operating at a 10Hz repetition rate. Irradiation intensity can be varied up to 40 mJ/cm2. The light is delivered via a beam expander creating a beam diameter of around 1 cm to cover the entire specimen under investigation. The photoacoustic signals are recorded with a curvilinear detector array (Imasonic, Besançon) consisting of 32 elements and shaped to 85º of a circle of 40mm radius. The center frequency of the array is 6.25MHz with a reception bandwidth >80%. Individual elements have sizes of 10 by 0.25mm. These elements are arranged with an inter-element spacing of 1.85mm. At each position signals are acquired from the detector using a 32 channel pulse-receiver system (Lecoeur Electronique, Paris) with a sampling rate of 80MHz. Filtered acoustic backprojection was used to reconstruct the PA images off-line (35).

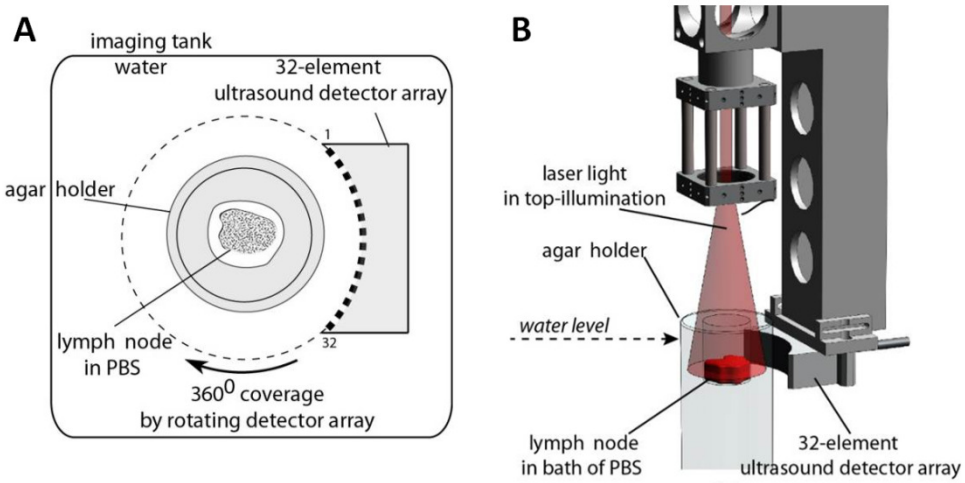

Fig. 1. A: A top view of the tomographic photoacoustic setup utilizing top illumination. B: A three dimensional schematic of the setup. The holder containing the lymph node is illuminated from the top while the ultrasound detector is rotated around the holder. The water in the imaging tank ensures ultrasound transmission to the detector.

Before the start of scanning procedure, the setup was calibrated using an agar phantom containing four horse tail hairs to ascertain the tomographic geometry. All nodes were fixed with a small amount of ultrasound gel to prevent floating and disruptive movements. Once

fixed, the position of the node was checked by visual examination and air bubbles around the sample were removed. The temperature of the water in the PA tank was monitored throughout the experiment to avoid image reconstruction irregularities caused by a change in the speed of sound.

All scans were performed using an irradiation intensity of around 15 mJ/cm^2, a wavelength of 720 nm and 20 projections. While 720 nm is not an exclusive wavelength (Fig. 2B), we can identify at this wavelength a low absorption of total hemoglobin coupled with a significant absorption of the dispersion. Further, absorption by fat (and water) is negligible (2). In addition, our previous research shows (5) that the large penetration depth of near-infra-red illumination also contains an advantage for the imaging of larger nodes and nodes that contain significant amounts of extranodal fat.

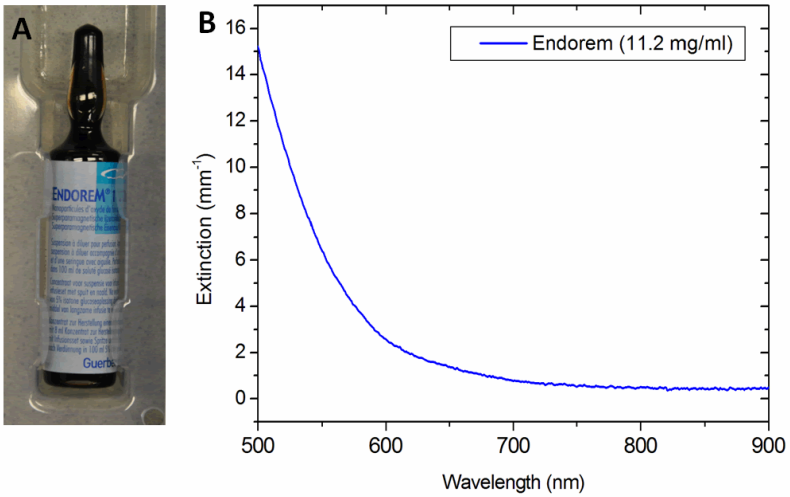

Fig. 2. A: Photograph of an Endorem® vial displaying the dark color of the dispersion
B: The extinction spectrum of an Endorem® dispersion.

4.2.4 Magnetic Resonance Imaging

Verification of the PA contrast results with regard to the presence of iron oxide nanoparticles and their distribution in the node was performed using a 14 T MRI system (Bruker, Ettlingen, Germany). The system was equipped with a vertical narrow bore magnet (14.1 T), a B0 compensation unit (BGU-II) and three 1/60 amplifier units (X, Y and Z). A micro-imaging probe, equipped with a 10mm diameter saddle coil insert, was used. All experiments (acquisition and processing) were carried out using ParaVision (version 4.0)/Top Spin (version 1.5) software. The nodes were fixated in 4% buffered formaldehyde after PA imaging and transferred to quartz NMR tubes with a diameter of 10 mm. All nodes were positioned in such way to ensure that the orientation corresponded to that of the PA scans. The iron oxide nanoparticles shorten both T2 and T1 relaxation times, which results

in a signal loss at locations of the SPIOs inside the lymphatic tissue. A multi-slice–multi-echo (MSME) imaging sequence was used with an echo time of 10 ms and a repetition time of 1000 ms. The sequence produces a larger longitudinal and transverse magnetization, making the surrounding fat appear bright, facilitating nodal identification and SPIO distribution analysis in the imaged volume. Images were acquired using a matrix dimension of 256x256, a field of view of 1 cm and a slice thickness of 0.5 mm. Signal averaging was varied between 5 and 10, based on the quality of the acquired image.

4.2.5 Vibrating Sample Magnetometry

The amount of iron oxide inside the lymphatic tissue was quantified with a vibrating sample magnetometer (Quantum Design, San Diego, CA, USA) with a variable magnetic field of ± 4T. Nodes were kept inside the quartz NMR tubes and strongly fixated to ensure no movement occurred owing to the vibrations of the device. Measurements were checked for movement artifacts and all results were correlated to three reference samples containing a known amount of iron oxide. A standard deviation and average iron oxide amount were thencalculated.

4.2.6 Optical Property Estimation

Based on the iron quantities measured within the nodes using vibrating sample magnetometry (VSM), we aimed to estimate the optical absorption coefficient μ_a (mm^{-1}). To this end, interaction efficiencies (extinction, scattering and absorption) were estimated using Mie theory (36) for a core radius of 2.5 nm and a shell radius of 15 nm (31), with dielectric data for iron oxide and dextran from Schlegel *et al.* (27) and Butler and Cameron (37). Results indicated that the scattering component of the extinction was small compared with the absorption component. Spectroscopy (UV-2401PC spectrophotometer, Shimadzu, Tokyo, Japan) on a diluted Endorem dispersion ($0.56x10^{-6}$ g/mm^3) was used to measure the extinction coefficient μ_{ext} (mm^{-1}) at 720nm and, by correlating the μ_{ext} to the iron quantities within each node divided by the nodal volume, an estimation of the μ_{ext} within each node was produced.

The volume within each node was calculated using the MRI slice dimensions. In addition, the PA contrast of SPIO particles was compared with that of whole human blood by embedding the measured iron amounts inside a phantom. By taking the lowest and highest iron amounts measured within the nodes and dividing them by the nodal volume, an estimation of the SPIO concentration within the nodal tissue could be made. The estimated concentrations were diluted from the stock dispersion and injected into two nylon tubes (i.d. 1 mm, o.d. 1.8 mm). These were embedded one-by-one, into a 2% agar phantom in which a similar tube containing unclotted whole human blood was placed, as depicted in Fig. 5(A). By measuring the average PA response of the tubes, the contrast between both could be quantified.

4.2.7 Histology

To verify the presence of SPIOs inside the lymphatic tissue, additional histological analysis of several nodes was performed using a Pearls Prussian Blue stain (Sigma-Aldrich, St Louis, MO, USA). The nodes were embedded in paraffin and cut into 5 µm slices. Special attention was paid to the orientation of the cutting surface, which was kept parallel to the imaging plane of both the PA as the MR image. After staining, the slices were imaged and photographed using a bright field optical microscope (Nikon E600, Tokyo, Japan).

4.3 Results

During the experiments none of the animals experienced visual signs of discomfort following both IFA and Endorem® injections. Some licking of the hind legs was noted directly after injection; however, all animals functioned normally during the subsequent days. Injection of the different Endorem® solutions into the hind leg of the animals entailed a visible discoloring throughout the lower part of the injected leg. After excision a dark discoloring of all of the popliteal lymph nodes draining the hind leg in which Endorem® was injected was observed, while lymph nodes from hind legs without Endorem®

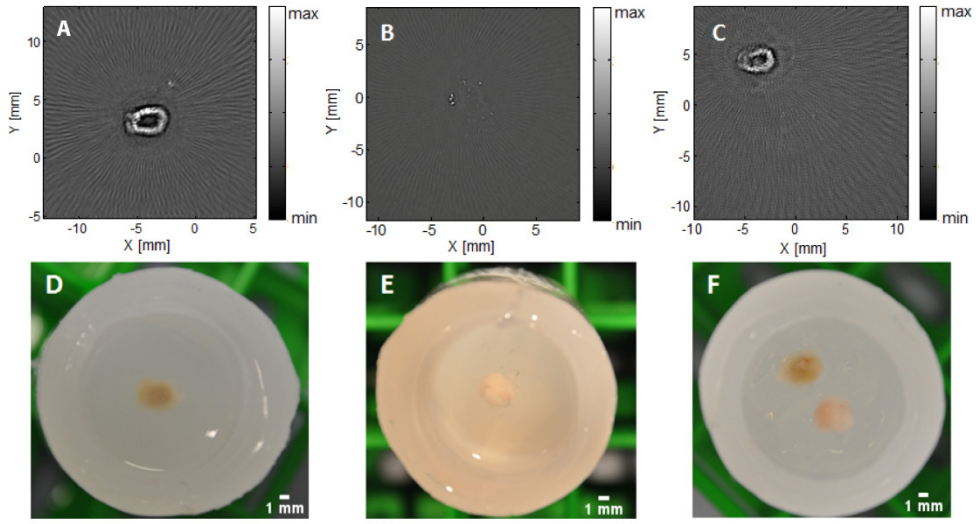

Fig. 3. A: Photoacoustic image of lymph node containing Endorem®. B: PA image of control node. C: PA image of both the control and the Endorem® containing node. D: Photograph of lymph node containing Endorem®. E: Photograph of control node. F: Photograph of both the control and the Endorem® containing node.

administration did not possess this discoloring. All nodes had diameters of around 3–5 mm and most contained some extranodal fat.

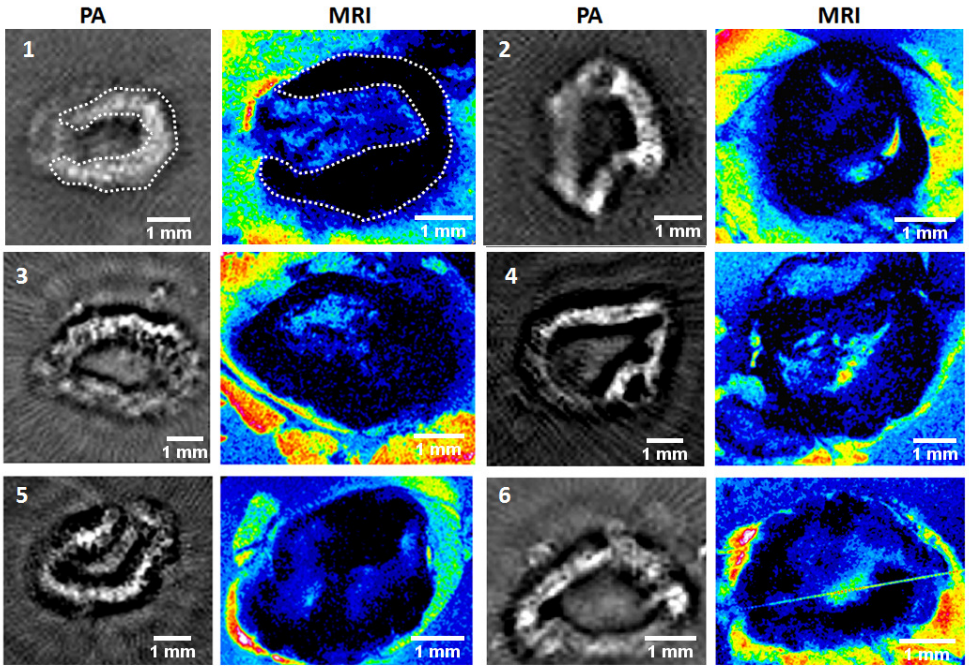

Fig. 4. Photoacoustic and MR image comparison of all resected lymph nodes with contrast injection. As shown in lymph node 1 (white dotted line), the PA response pattern is comparable with the location of MRI signal decrease. Some nodes show a continuous contrast band throughout their periphery (1,5), while others show some small irregularities (4,6).

Figure 3 shows the PA images of a contrast and a control node (A–C) together with corresponding photographs of the nodes in their imaged positions (D–F). Figure 4 shows PA and MR images of all contrast nodes and demonstrates their correlation in contrast distribution. PA imaging of the individual nodes showed bands of clear signal increase in the periphery of the nodes suspected of containing SPIOs (Figs 3A and 4, columns 1 and 3). Almost no signal enhancement was noted in the center of these nodes, although some contained larger signal poor areas then others. No significant increase in signal was noted in the popliteal nodes excised from hind legs not injected with Endorem® (control nodes), corresponding with the absence of discoloring noted after excision (Fig. 3B). The image of both the control and the contrast containing node shows this clear distinction in PA response (Fig. 3C). The small centers of absorption in the PA image of the control node (Fig. 3B) are possibly small blood droplets in the extranodal fat caused by the surgical resection. Although small amounts of Endorem® up to 0.28mg, were injected (Fig. 4(5,6), Table 1), all nodes suspected of containing SPIOs showed enough PA signal to be distinguished from nodes without contrast injection.

MR images (Fig. 4, columns 2 and 4) showed a clear signal decrease in all discolored nodes, largely located in the periphery of the nodal volume. Distribution of this decrease corresponded with the areas showing PA response in most cases. Almost all nodes showed only a small decrease in signal in the center of their anatomy. Calculation of the dimensions of all nodes using the MR information revealed a strong correlation with the dimension calculations based on the PA scans (Table 2). MRI of the control nodes showed no significant decrease in signal throughout the nodal volume corresponding to a lack of SPIOs.

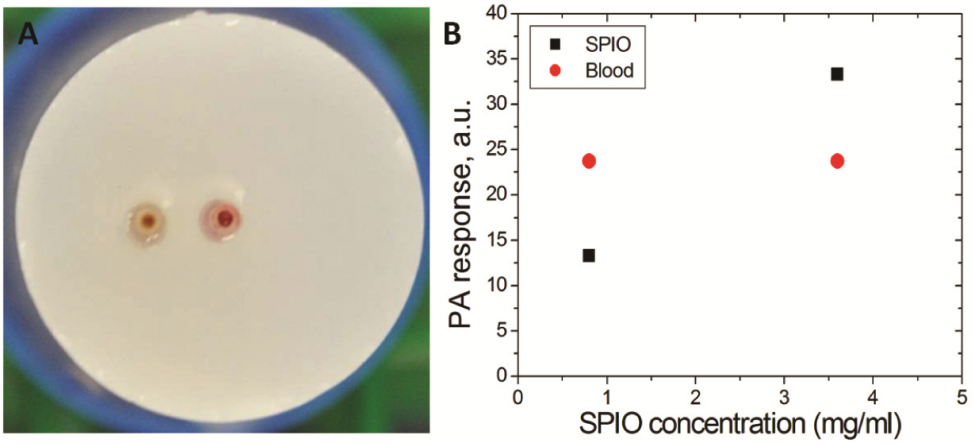

Fig. 5. Phantom measurement of the amount of PA contrast generated within the node compared to that of whole blood. A: Photograph of the agar phantom containing one tube filled with different concentrations of SPIO particles (left) and one tube filled with whole human blood (right).
B: The average PA contrast measured within the tubes for a SPIO concentration of 0.8 and 3.6 mg/ml. At a SPIO concentration of 3.6 mg/ml the PA response is higher than that of blood.

Vibrating sample magnetometry measurements showed the presence of a superparamagnetic contrast agent inside all nodes suspected of contrast inclusion, although the amounts varied between the nodes. Table 1 displays the amount of iron oxide measured by VSM inside each node together with the estimated absorption coefficients. The highest iron quantity was measured in node 2 at 51±4 µg, while the lowest quantity was determined in node 6 at 11±1 µg. The control nodes obtained from the animals subjected to contrast injections at the contra-lateral limb showed the presence of very small deposits of iron, up to 1 µg, while the nodes from the control animal did not display any superparamagnetic behavior. Based on these amounts, the estimated μ_a of the contrast nodes varied between 0.27 and 0.06 mm^{-1}. By taking the nodal dimensions measured by MRI into account, the highest (51 µg) and lowest (11 µg) iron amounts correlated to SPIO concentrations of 3.6 and 0.8 mg/ml. PA measurement of these concentrations and whole human blood showed an average PA response of 23 for blood compared with a response of 15 and 34 for respectively the low and high concentration samples (Fig. 5B). Histology (Fig. 6)

confirmed the presence of significant iron deposits throughout the nodes suspected of nanoparticle inclusion. Iron presence was most pronounced inside macrophages located in the periphery of the nodes. No significant presence of iron was revealed by the histological assessment of the control nodes (Fig. 6D).

4.4 Discussion and Conclusions

The results obtained from the animal model show that PA imaging can be used to detect the presence of iron oxide nanoparticles inside lymphatic tissue. Subcutaneous injection of Endorem® did not produce any negative side effects in the animals, giving an indication that the safety profile may potentially be favorable for subcutaneous applications in humans. The effects of the IFA injection to initiate nodal swelling enabled
us to easily pinpoint and extract the popliteal node while ensuring that both imaging techniques would be able to map the contrast agents accumulation. Weissleder *et al.* (18) showed that the distribution and amount of iron in these so-called hyperplastic nodes are similar to those of normal nodes, which indicates that the uptake of these nodes is not significantly altered by the adjuvant.

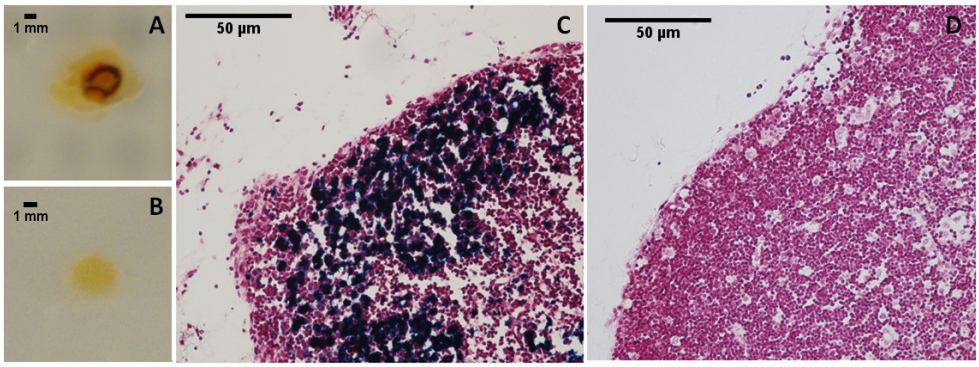

Fig. 6. A: Photograph of a paraffin section of a contrast node showing a dark discoloring in its peripheral zone (node 1). B: Photograph of a paraffin section of a control node showing no significant discoloring (node 7). C: Prussian Blue stained microscopic image of a contrast node (node 1) (Magnification 20x) showing iron deposits in the periphery of the node D: Prussian Blue stained microscopic image of a control node (node 7) (Magnification 20x) showing no irondeposits.

Predominant PA signal generation was noted in the periphery of the nodes, which coincides with the location of the peripheral sinusoidal macrophages. MRI shows clear loss of signal in corresponding regions in the nodes, confirming that most of the iron oxide nanoparticles are located at these locations. The histologic presence of iron particles in the periphery of the nodes confirms the imaging results and demonstrates that the contrast agent is distributed selectively at the margins of the lymphatic tissue. An explanation for this phenomenon is given by Lee *et al.* (38),who also noted signal loss in the periphery of their unenlarged rat nodes using 9.4 T MR imaging and Prussian blue staining. Their analysis

suggested that the predominant accumulation of iron oxide nanoparticles in the peripheral sinusoidal macrophages lining the subcapsular sinuses gave rise to this phenomenon. The larger size of the Endorem SPIO particles in comparison to the particles used in their study could have further facilitated the retention of the particles in the nodal periphery. However, an inhomogeneous distribution was also noted by Lind *et al.* (39) using SPIOs with a larger hydrodynamic size. Prussian blue stained histology indicated that some nodes did contain smaller iron deposits in their medullary sinuses or less pronounced iron presence in their periphery compared with the imaging results. It should be noted, however, that histology is less sensitive to the presence of iron oxide nanoparticles than MRI, making a point-to-point comparison between histological slices and images difficult to produce in most situations.

Table 1. Lymph nodes sorted by number with their corresponding iron quantities and stimated absorption coefficients at 720nm

Number	Injected Iron (µg)	Iron inside the node (µg)	μ_a (mm^{-1})
1	1120	27 ± 2	0.14 ± 0.01
2	1120	51 ± 4	0.27 ± 0.02
3	560	40 ± 3	0.21 ± 0.02
4	560	49 ± 3	0.26 ± 0.02
5	280	30 ± 2	0.15 ± 0.01
6	280	11 ± 1	0.06 ± 0.01
7-10	0	0 ± 1	± 0

Iron quantity analysis using vibrating sample magnetometry revealed that the amount of iron present in each node varied significantly between animals. No clear relation could be established between the amount of iron injected and the amount of iron captured within the nodal volume. In addition, the average PA response within the contrast band in each node could not be correlated to the corresponding measured iron amount. This is most likely due to the differences in extranodal fat covering each sample, which leads to the fluence at the slice carrying the signal band being different. However, our results show that the location of the contrast agent could still be verified at a quantity as low as 11±1 µg, indicating that, if the human situation showed less nodal uptake, it could still be possible to perform accurate nodal staging. The phantom measurements indicate that the amount of PA response of SPIO deposits mainly depends on the quantity in which it is present in the nodes and that at higher concentrations they produce more PA signal than human blood. However, as shown by our VSM measurements, the amount of iron obtained within the nodes is variable, so it remains unclear whether an *in vivo* approach could clearly visualize the characteristics of the absorption patterns mentioned (28). The influence of other biological structures is limited in an *ex vivo* intra-operative staging setting, which therefore should be the first clinical application goal of the technique.

The estimated absorption coefficients show that the optical absorption of the tissue is increased owing to the inclusion of the nanoparticles. The estimated amounts of absorption do not impede the penetration of optical energy into lower parts of the node, indicating that metastases that are located deeper within the node could also be visualized. Since normal lymphatic tissue displays low absorption at 720 nm, the nodal outline and size could not be distinguished in nodes 7–10 (Table 2); however, the dimensions and shape extracted from the PA images of the nodes containing SPIOs match those estimated from MRI. An accurate depiction of nodal size using SPIO-enhanced PA imaging could function as an additional indicator of possible metastatic involvement, because larger nodes (≥1 cm) are more likely to include metastases (40). The fact that nodes without SPIOs do not produce recognizable PA response patterns could imply that nodes that are totally filled with malignant cells will also not show up on PA measurements. In these cases, clinical staging has to be performed on images without distinguishable features, which could create some problems with regard to specificity. However, in the case of a sentinel node biopsy, an additional colored tracer, spreading homogeneously through the node, is always injected for locating the actual sentinel node. Multiple wavelength imaging (41,42) could in this case provide us with a nodal outline based on the colored tracer while staging decisions could be made on the images of a wavelength sensitive for the SPIO contrast agent. In nodes with smaller metastases, macrophages will be replaced by tumor cells in specific parts of the node. These tumor deposits occupying in regions as small as 2 mm in the node have been proven to be detectable in MR studies (43-45). Likewise in PA images, smaller metastases could be detectable based on spatial features showing low intensities. How sensitively these features can be visualized in PA needs to be investigated in future experiments using a metastatic model.

Table 2. Calculated maximal and perpendicular diameters of all lymph nodes based on both photoacoustic (PA) imaging and MRI. Lymph nodes sorted by number. Measured sizes contain error margins of ± 0.3 mm. PA dimensions of nodes 7–10 could not be calculated because of their lack of PA response

	PA based diameter		MRI based diameter	
Number	Maximal (mm)	Perpendicular (mm)	Maximal (mm)	Perpendicular (mm)
1	3.5	3.0	3.5	3.0
2	4.1	2.8	3.4	2.8
3	4.5	2.8	4.5	2.8
4	4.1	2.6	4.1	2.9
5	4.0	3.3	4.2	2.9
6	3.5	2.6	3.4	2.6
7	-	-	3.5	2.6
8	-	-	3.3	2.8
9	-	-	3.9	3.1
10	-	-	3.4	3.2

The detection of SPIOs in lymphatic tissue using PA imaging offers possibilities for distinguishing nodes with nanoparticle deposits from nodes lacking uptake. Future research should verify if the difference in uptake between malignant and benign nodes can be visualized using PA imaging, creating opportunities for fast intra-operative nodal staging. Detection of iron oxide nanoparticles using PA imaging can prove especially promising once other types of iron oxide-based agents enter the clinic. A combination of diagnostic pre-operative imaging using MRI and per-operative staging using PA imaging could be performed and the translation of PA imaging into the clinic would also benefit from a direct comparison of the results with an established imaging method like MRI. Moreover, the magnetic properties of the SPIOs could also be used to influence photoacoustic signals, thereby generating additional biological information and considerably improving specificity (46-48). Although our *ex vivo* study mainly shows the potential for intra-operative imaging, non-invasive high-resolution PA lymph node mapping (49,50) after SPIO injection for superficial nodes could also be investigated, although it remains unclear if SPIO particles provide sufficient *in vivo* contrast for such an application.

4.5 Conclusion

We conclude that iron oxide nanoparticles are able to enhance PA response in lymph nodes because of their active uptake by nodal macrophages in locations unaffected by metastatic cells and therefore have the potential to be implemented as a PA contrast agent for nodal

staging purposes. Further research using a metastatic model should show if PA imaging based on these nanoparticles is able to produce reliable indicators for the presence of metastatic deposits.

4.6 References

1. Li C, Wang LV. Photoacoustic tomography and sensing in biomedicine. Phys Med Biol 2009; 54(19):R59-97.
2. Beard P. Biomedical photoacoustic imaging. Interface Focus 2011; 1(4):602-631.
3. Zharov VP, Galanzha EI, Shashkov EV, Khlebtsov NG, Tuchin VV. In vivo photoacoustic flow cytometry for monitoring of circulating single cancer cells and contrast agents. Opt Lett 2006; 31(24):3623-3625.
4. Weight RM, Dale PS, Viator JA. Detection of circulating melanoma cells in human blood using photoacoustic flowmetry. Conf Proc IEEE Eng Med Biol Soc 2009; 2009:106-109.
5. Jose J, Grootendorst DJ, Vijn TW, Wouters MW, van Boven H, van Leeuwen TG, Steenbergen W, Ruers TJ, Manohar S. Initial results of imaging melanoma metastasis in resected human lymph nodes using photoacoustic computed tomography. J Biomed Opt 2011; 16(9):096021.
6. Grootendorst D, Jose J, Van der Jagt P, Van der Weg W, Nagel K, Wouters M, Van Boven H, Van Leeuwen T, Steenbergen W, Ruers T. Initial experiences in the photoacoustic detection of melanoma metastases in resected lymph nodes. 2011. p 78993J.
7. Piras D, Xia WF, Steenbergen W, van Leeuwen TG, Manohar S. Photoacoustic Imaging of the Breast Using the Twente Photoacoustic Mammoscope: Present Status and Future Perspectives. Ieee J Sel Top Quant 2010; 16(4):730-739.
8. Luke GP, Yeager D, Emelianov SY. Biomedical applications of photoacoustic imaging with exogenous contrast agents. Ann Biomed Eng 2012; 40(2):422-437.
9. Eghtedari M, Oraevsky A, Copland JA, Kotov NA, Conjusteau A, Motamedi M. High sensitivity of in vivo detection of gold nanorods using a laser optoacoustic imaging system. Nano Lett 2007; 7(7):1914-1918.
10. Manohar S, Ungureanu C, Van Leeuwen TG. Gold nanorods as molecular contrast agents in photoacoustic imaging: the promises and the caveats. Contrast Media Mol Imaging 2011; 6(5):389-400.
11. de la Zerda A, Kim JW, Galanzha EI, Gambhir SS, Zharov VP. Advanced contrast nanoagents for photoacoustic molecular imaging, cytometry, blood test and photothermal theranostics. Contrast Media Mol Imaging 2011; 6(5):346-369.
12. McCormack DR, Bhattacharyya K, Kannan R, Katti K, Viator JA. Enhanced photoacoustic detection of melanoma cells using gold nanoparticles. Lasers Surg Med 2011; 43(4):333-338.
13. Song KH, Kim C, Cobley CM, Xia Y, Wang LV. Near-infrared gold nanocages as a new class of tracers for photoacoustic sentinel lymph node mapping on a rat model. Nano Lett 2009; 9(1):183-188.
14. Yang X, Skrabalak SE, Li ZY, Xia Y, Wang LV. Photoacoustic tomography of a rat cerebral cortex in vivo with au nanocages as an optical contrast agent. Nano Lett 2007; 7(12):3798-3802.

15. de la Zerda A, Liu Z, Bodapati S, Teed R, Vaithilingam S, Khuri-Yakub BT, Chen X, Dai H, Gambhir SS. Ultrahigh sensitivity carbon nanotube agents for photoacoustic molecular imaging in living mice. Nano Lett 2010; 10(6):2168-2172.
16. Hirsch LR, Stafford RJ, Bankson JA, Sershen SR, Rivera B, Price RE, Hazle JD, Halas NJ, West JL. Nanoshell-mediated near-infrared thermal therapy of tumors under magnetic resonance guidance. Proc Natl Acad Sci U S A 2003; 100(23):13549-13554.
17. Fu K, Sun JT, Lin AWH, Wang H, Halas NJ, Drezek RA. Polarized angular dependent light scattering properties of bare and PEGylated gold nanoshells. Curr Nanosci 2007; 3(2):167-170.
18. Weissleder R, Elizondo G, Josephson L, Compton CC, Fretz CJ, Stark DD, Ferrucci JT. Experimental lymph node metastases: enhanced detection with MR lymphography. Radiology 1989; 171(3):835-839.
19. Daldrup HE, Link TM, Blasius S, Strozyk A, Konemann S, Jurgens H, Rummeny EJ. Monitoring radiation-induced changes in bone marrow histopathology with ultra-small superparamagnetic iron oxide (USPIO)-enhanced MRI. J Magn Reson Imaging 1999; 9(5):643-652.
20. Metz S, Bonaterra G, Rudelius M, Settles M, Rummeny EJ, Daldrup-Link HE. Capacity of human monocytes to phagocytose approved iron oxide MR contrast agents in vitro. Eur Radiol 2004; 14(10):1851-1858.
21. Raynal I, Prigent P, Peyramaure S, Najid A, Rebuzzi C, Corot C. Macrophage endocytosis of superparamagnetic iron oxide nanoparticles: mechanisms and comparison of ferumoxides and ferumoxtran-10. Invest Radiol 2004; 39(1):56-63.
22. Clement O, Siauve N, Cuenod CA, Frija G. Liver imaging with ferumoxides (Feridex): fundamentals, controversies, and practical aspects. Top Magn Reson Imaging 1998; 9(3):167-182.
23. Motomura K, Ishitobi M, Komoike Y, Koyama H, Noguchi A, Sumino H, Kumatani Y, Inaji H, Horinouchi T, Nakanishi K. SPIO-enhanced magnetic resonance imaging for the detection of metastases in sentinel nodes localized by computed tomography lymphography in patients with breast cancer. Ann Surg Oncol 2011; 18(12):3422-3429.
24. Anzai Y, McLachlan S, Morris M, Saxton R, Lufkin RB. Dextran-coated superparamagnetic iron oxide, an MR contrast agent for assessing lymph nodes in the head and neck. AJNR Am J Neuroradiol 1994; 15(1):87-94.
25. Bellin MF, Roy C, Kinkel K, Thoumas D, Zaim S, Vanel D, Tuchmann C, Richard F, Jacqmin D, Delcourt A, Challier E, Lebret T, Cluzel P. Lymph node metastases: safety and effectiveness of MR imaging with ultrasmall superparamagnetic iron oxide particles--initial clinical experience. Radiology 1998; 207(3):799-808.
26. Will O, Purkayastha S, Chan C, Athanasiou T, Darzi AW, Gedroyc W, Tekkis PP. Diagnostic precision of nanoparticle-enhanced MRI for lymph-node metastases: a meta-analysis. Lancet Oncol 2006; 7(1):52-60.
27. Schlegel A, Alvarado SF, Wachter P. Optical-Properties of Magnetite (Fe3o4). J Phys C Solid State 1979; 12(6):1157-1164.
28. Mienkina MP, Friedrich CS, Hensel K, Gerhardt NC, Hofmann MR, Schmitz G. Evaluation of Ferucarbotran (Resovist) as a photoacoustic contrast agent /

Evaluation von Ferucarbotran (Resovist) als photoakustisches Kontrastmittel. Biomed Tech (Berl) 2009; 54(2):83-88.
29. McLaughlin RA, Scolaro L, Robbins P, Hamza S, Saunders C, Sampson DD. Imaging of human lymph nodes using optical coherence tomography: potential for staging cancer. Cancer Res 2010; 70(7):2579-2584.
30. Horsnell JD, Smith JA, Sattlecker M, Sammon A, Christie-Brown J, Kendall C, Stone N. Raman spectroscopy--a potential new method for the intra-operative assessment of axillary lymph nodes. Surgeon 2012; 10(3):123-127.
31. Cengelli F, Maysinger D, Tschudi-Monnet F, Montet X, Corot C, Petri-Fink A, Hofmann H, Juillerat-Jeanneret L. Interaction of functionalized superparamagnetic iron oxide nanoparticles with brain structures. J Pharmacol Exp Ther 2006; 318(1):108-116.
32. Wang YX, Hussain SM, Krestin GP. Superparamagnetic iron oxide contrast agents: physicochemical characteristics and applications in MR imaging. Eur Radiol 2001; 11(11):2319-2331.
33. Aucouturier J, Dupuis L, Deville S, Ascarateil S, Ganne V. Montanide ISA 720 and 51: a new generation of water in oil emulsions as adjuvants for human vaccines. Expert Rev Vaccines 2002; 1(1):111-118.
34. Klerkx WM, Geldof AA, Heintz AP, van Diest PJ, Visser F, Mali WP, Veldhuis WB. Longitudinal 3.0T MRI analysis of changes in lymph node volume and apparent diffusion coefficient in an experimental animal model of metastatic and hyperplastic lymph nodes. J Magn Reson Imaging 2011; 33(5):1151-1159.
35. Jose J, Willemink RG, Resink S, Piras D, van Hespen JC, Slump CH, Steenbergen W, van Leeuwen TG, Manohar S. Passive element enriched photoacoustic computed tomography (PER PACT) for simultaneous imaging of acoustic propagation properties and light absorption. Opt Express 2011; 19(3):2093-2104.
36. Bohren CF, Huffman DR. Absorption and scattering of light by small particles: Wiley-Vch. 2008.
37. Butler MF, Cameron RE. A study of the molecular relaxations in solid starch using dielectric spectroscopy. Polymer 2000; 41(6):2249-2263.
38. Lee A, Weissleder R, Brady T, Wittenberg J. Lymph nodes: microstructural anatomy at MR imaging. Radiology 1991; 178(2):519-522.
39. Lind K, Kresse M, Debus NP, Muller RH. A novel formulation for superparamagnetic iron oxide (SPIO) particles enhancing MR lymphography: comparison of physicochemical properties and the in vivo behaviour. J Drug Target 2002; 10(3):221-230.
40. Catalano MF, Sivak MV, Jr., Rice T, Gragg LA, Van Dam J. Endosonographic features predictive of lymph node metastasis. Gastrointest Endosc 1994; 40(4):442-446.
41. Razansky D, Baeten J, Ntziachristos V. Sensitivity of molecular target detection by multispectral optoacoustic tomography (MSOT). Med Phys 2009; 36(3):939-945.
42. Shao P, Cox B, Zemp RJ. Estimating optical absorption, scattering, and Grueneisen distributions with multiple-illumination photoacoustic tomography. Appl Opt 2011; 50(19):3145-3154.

43. Taupitz M, Wagner S, Hamm B, Binder A, Pfefferer D. Interstitial MR lymphography with iron oxide particles: results in tumor-free and VX2 tumor-bearing rabbits. American Journal of Roentgenology 1993; 161(1):193-200.
44. Heesakkers RA, Hovels AM, Jager GJ, van den Bosch HC, Witjes JA, Raat HP, Severens JL, Adang EM, van der Kaa CH, Futterer JJ, Barentsz J. MRI with a lymph-node-specific contrast agent as an alternative to CT scan and lymph-node dissection in patients with prostate cancer: a prospective multicohort study. Lancet Oncol 2008; 9(9):850-856.
45. Harisinghani MG, Barentsz J, Hahn PF, Deserno WM, Tabatabaei S, van de Kaa CH, de la Rosette J, Weissleder R. Noninvasive detection of clinically occult lymph-node metastases in prostate cancer. N Engl J Med 2003; 348(25):2491-2499.
46. Haraszczuk R, Nurzyńska K. Photoacoustic detection of sentinel lymph node with sensor arrays. Journal of Medical Informatics 2011; 17:233-238.
47. Qu M, Mallidi S, Mehrmohammadi M, Truby R, Homan K, Joshi P, Chen YS, Sokolov K, Emelianov S. Magneto-photo-acoustic imaging. Biomed Opt Express 2011; 2(2):385-396.
48. Qu M, Mehrmohammadi M, Emelianov S. Detection of nanoparticle endocytosis using magneto-photoacoustic imaging. Small 2011; 7(20):2858-2862.
49. Kim C, Erpelding TN, Jankovic L, Pashley MD, Wang LV. Deeply penetrating in vivo photoacoustic imaging using a clinical ultrasound array system. Biomed Opt Express 2010; 1(1):278-284.
50. Kim C, Erpelding TN, Jankovic L, Wang LV. Performance benchmarks of an array-based hand-held photoacoustic probe adapted from a clinical ultrasound system for non-invasive sentinel lymph node imaging. Philos Transact A Math Phys Eng Sci 2011; 369(1955):4644-4650.

CHAPTER 5

INTRA-OPERATIVE EX VIVO PHOTOACOUSTIC NODAL STAGING IN A RAT MODEL USING A CLINICAL SUPERPARAMAGNETIC IRON OXIDE NANOPARTICLE DISPERSION*

The ability to accurately detect tumor metastases in lymph nodes is essential for intra-operative staging of various malignancies. Histopathological assessment of nodes has the drawback of a time delay before results are available to the surgeon and a likelihood of missing metastases. Photoacoustic (PA) imaging has been shown to possess the potential to detect melanoma metastases in resected in toto lymph nodes based on intrinsic contrast. To extend application of the method to other malignancies, extrinsic contrast for lymphatic mapping is important. We investigate in a metastatic animal model whether clinically approved superparamagnetic iron oxide (SPIO) nanoparticles, applied for MRI, can help PA imaging for staging in an intra-operative ex vivo setting. Imaging results are compared with 14 Tesla MR images and histology. We observe that irregularities in SPIO distribution in PA images of the nodes and a decrease in contrast correlate with metastatic involvement as seen in MR images and histology. The results show that a PA based imaging technique may be valuable for nodal staging in the field of surgical oncology.

* This chapter will be published as: D. J. Grootendorst, R. M. Fratila, M. Visscher, B. Ten Haken, R.J.A. Van Wezel, S. Rottenberg, W. Steenbergen, S. Manohar, T. J. M. Ruers, "Intra-operative ex vivo photoacoustic nodal staging in a rat model using a clinical superparamagnetic iron oxide nanoparticle dispersion" in the Journal of BioPhotonics, doi: 10.1002/jbio.201200204, Ahead of print "

5.1 Introduction

The presence of lymphatic metastases is a predictor of poor outcome in many solid malignancies (1-4). Metastasis positive lymph nodes are associated with a decrease of the 5-year survival of melanoma patients, independent of other prognostic factors of the primary tumor (5). Likewise, the number of resected metastatic lymph nodes correlates with survival in breast cancer patients (6). Despite the importance of lymph node metastases as highlighted by its inclusion in cancer staging systems, both detection and treatment remain far from optimal.

Superparamagnetic iron oxide nanoparticle (SPIO) enhanced MRI has been proven to detect small and otherwise undetectable lymph-node metastases in patients with prostate cancer (7), providing a possibility to improve early diagnosis and decision making. In addition, this approach has also been proven to be of additional benefit for head and neck, breast and pelvis lymph node assessment showing an overall sensitivity of 88% and an overall specificity of 96% based on 19 prospective studies (8). After subcutaneous or intravenous injection, SPIOs are cleared by draining lymphatic vessels and transported to the lymph nodes where they are phagocytosed by nodal macrophages. Inhomogeneties in SPIO distribution in a lymph node arise once metastatic cells displace the normal nodal architecture. MRI is able to visualize this displacement due to the longer relaxation times arising from the absence of SPIOs at these locations and can be used to distinguish benign from metastatic lymph nodes. The dissimilarity in SPIO distribution between benign and metastatic nodes is schematically displayed in Figure 1.

The success of the approach in pre-operative staging together with the fact that coated SPIOs contain a satisfactory safety profile for human applications (9) have cleared several SPIO dispersions for clinical use. However, MRI is unable to detect micrometastases less than 1 mm in size using a conventional 1.5 Tesla system (10) in pre- or intra-operative staging. The latter is important for decision making towards the nature of therapy and surgery to be performed. The availability of diagnostic information during the surgical procedure could for example, limit the number of resected lymph nodes during lymphadenectomies or offer the potential to perform a lymphadenectomy directly after sentinel lymph node resection. Both can reduce morbidity while saving time and funds.

Photoacoustic (PA) imaging, an emerging powerful imaging modality that uses optical absorption contrast and posseses ultrasonic resolution, is being widely applied within biomedical research (11,12). PA imaging relies on the detection of acoustic waves produced by the thermoelastic expansion of tissue following absorption of short pulsed optical illumination. By this mechanism, PA uncouples signal generation and detection since diffuse light excites ultrasound which can be detected with high resolution. Therefore, PA is able to obtain high resolution images using diffused light from deeper within biological samples compared to purely optical based techniques. In addition, in biological

tissue, ultrasonic scattering is about two to three orders of magnitude weaker than optical scattering, resulting in high spatial resolution compared to many optical techniques. The fact that PA imaging makes no use of ionizing radiation and enables fast imaging performance, could facilitate its introduction as an additional medical imaging technique.

PA imaging can both be based on endogenous biomolecules with natural PA contrast properties (e.g. hemoglobin, melanin), or exogenous contrast agents delivered by injection. The strong PA response of many endogenous biomolecules enables the visualization of the vasculature associated with breast carcinoma (13-16) or, for example the detection of melanoma cells (17) and melanoma metastases (18,19). Exogenous agents, on the other hand, are mostly applied to improve contrast, where the tissue lacks endogenous chromophores related to the studied disease state, including many malignancies (20-22). To this end, several contrast agents, including nano-materials (23-25), are the subject of extensive research to analyze their benefit in the imaging of specific disease states. Research into the PA imaging of the lymphatics using contrast agents is mostly centered around the mapping of the sentinel lymph node(s) (SLN(s)) (26-29). Recently, Akers *et al.* visualized the SLN of rats after methylene blue injection and verified their results using SPECT/CT (30). Pan *et al.* proved that copper nanoparticles can be used to enhance and visualize SLN(s) *in vivo* using PA imaging (31).

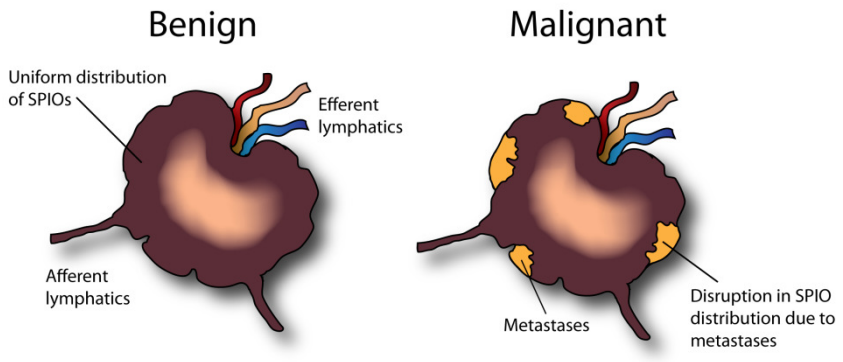

Fig. 1. Schematic of the nodal metastases detection scheme using SPIO nanoparticles. In a benign case, the SPIO particles accumulated in a regular pattern in the cortical zone of the lymph node through macrophage uptake 24 hours after injection. Accumulation is mostly centered in the cortical zone of the node due to the particle size of the SPIO agent. In a metastatic case, homogenous distribution of the particles is disrupted in locations where metastatic cells have replaced normal nodal architecture. These irregularities can be visualized with MRI due to differences in relaxation times between nodal tissue with and without SPIOs.

While showing promising results, most PA contrast agents are as yet in an experimental stage and would require extensive approval procedures before being approved for clinical use by the Food and Drugs Administration (FDA) or European Medicines Agency (EMA).

SPIOs on the other hand have been cleared for clinical use and their lymphatic metastasis detection potential has been verified by several clinical MRI studies (7,8) making them potentially valuable for intra-operative lymph node staging. Based on this, intra-operative staging of lymph nodes as researched by several other optical techniques like Optical Coherence Tomography (OCT) (32) and Raman spectroscopy (33), could possibly also be performed using the combination of photoacoustic imaging and SPIO nanoparticles. This would mean that freshly resected nodes could be scanned during the operation, offering direct diagnostic information to the surgical team. The increased penetration potential of PA imaging compared to optical techniques ensures imaging of the entire nodal volume without requiring the nodes to be sliced or damaged, retaining the possibility to perform (immuno)histochemical analysis post-operatively.

In order to explore this concept, our group recently used clinical SPIO dispersions in healthy rodents to verify that these deposits could be detected with PA. It was shown that the distribution of SPIOs could be mapped with accuracy down to an amount of approximately 11 µg, corresponding with a concentration of 0.8 mg/ml (34). With regard to the clinical potential of intra-operative lymph node staging using a combination of PA imaging and SPIOs, it however remains to be investigated whether, and on what basis, such a combination is able to make a distinction between benign and metastatic nodes.

In this work, we investigate whether lymph nodes metastases can be visualized with PA imaging after the subcutaneous injection of a clinically approved SPIO dispersion (Endorem®) in a metastatic animal model. Distinctive differences between benign and metastatic nodes are identified and PA imaging results are compared with high field MR images. Findings are verified by way of (immuno)histochemistry and limitations are discussed. In addition, we quantify the SPIO amounts inside the nodes using PA and correlate them to quantitative iron measurements. These experiments could produce the information needed to validate whether PA staging of lymph nodes can be performed with iron oxide nanoparticles. Overall, this could pave the way for the introduction of a PA based imaging technique in the field of surgical oncology.

5.2 Materials and Methods

5.2.1 Animal model and tumor cell line

All experiments were approved by the local Animal Care Committee. Female Copenhagen rats, weighing 150-200 g were subcutaneously injected with R3327 MAT-LyLu cells in their left hindpaw. The R3327 MAT LyLu prostate tumor variant has been used as an experimental model for syngeneic progression and metastasis of prostate adenocarcinoma. This model has also been frequently used to validate the potential of SPIO agents in MRI (35,36). *In vivo*, this tumor is characterized by a rapid and hormone-independent proliferation, anaplastic histology, and metastases to draining lymph nodes and lungs.

For the experiments, cells were cultured in RPMI-1640 medium, supplemented with 10% fetal calf serum and 100 ml penicillin/streptomycin. One million R3327 MAT LyLu tumor cells were dispersed in 0.1 mL of medium and inoculated aseptically in eight Copenhagen rats. The animals were separated into two groups depending on when a subcutaneous injection of 0.1 ml of SPIOs (11.2 g/l) (Endorem®, Guerbet, France) was administered in both hindpaws. The Endorem® particles are composed of several randomly clustered iron oxide cores (diameter 4–6 nm) embedded in a dextran coating (37). Particles have an estimated hydrodynamic size of 80–150nm (38). The extinction spectrum of an Endorem® dispersion is displayed in Figure 2. In the first animal group SPIOs were administered 5 days after tumor inoculation (minor metastatic group), where the second group received injections 8 days after inoculation (major metastatic group). Time spans were chosen according to a pilot study which showed that the popliteal lymph nodes were totally replaced by metastatic cells after 10 days and showed initial metastatic involvement after 4 days. Because we aimed to study the changes in SPIO distribution at an earlier stage of metastatic involvement, corresponding with smaller metastases, the inoculation times were set at 5 and 8 days.

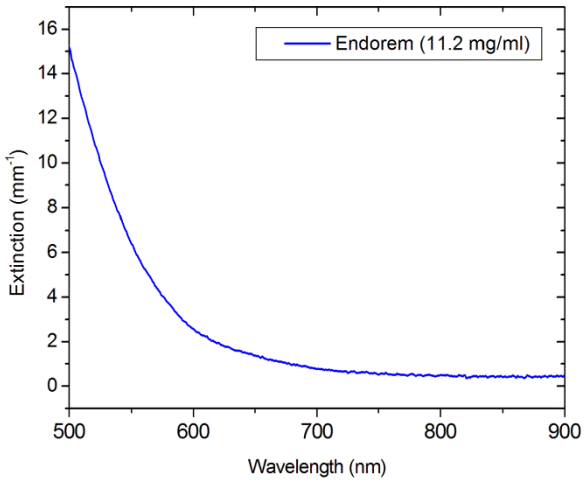

Fig. 2. Extinction spectrum of Endorem® (11,2 mg/ml).

Twenty-four hours after SPIO injection the animals were euthanized under anesthesia by cervical dislocation and the popliteal lymph nodes of both hindlegs were dissected. Four popliteal nodes of the contra lateral side were used as controls (control group) because earlier research has proven that these nodes remain free of metastasis within the used inoculation time (35). In addition to the two tumor groups, two animals received no SPIO injection after 5 days of inoculation (sham group) to verify the PA response in metastatic and normal nodes without SPIOs. After PA and MR imaging, the nodes were embedded in paraffin, cut into 5 µm slices and stained using a normal H&E staining. To visualize the

locations of the metastases and compare them with the PA and MR images, one of the nodes was additionally immunohistochemically stained for vimentin. Vimentin, a type III intermediate filament (IF) protein and mesenchymal marker, is specifically suited to stain poorly differentiated and highly metastatic cells like the MAT-lylu line. Attention was paid during sectioning of the tissue to ensure the orientation corresponded with the imaging planes of both PA and MR imaging.

5.2.2 Photoacoustic imaging setup

Resected nodes were placed inside a hollow transparent 3% Agar sample holder with an inner diameter of 25 mm and wall thickness of 10 mm. The sample holder was filled with phosphate buffered saline (PBS) to prevent tissue degradation and placed in the center of a large water container.

The detector was placed orthogonal to the light illumination from the top and rotated around the object to acquire a tomographic measurement. Twenty tomographic projections were acquired for each image using the instrument we described earlier (39). In summary, the system (Fig. 3) consists of a Q-switched Nd:YAG laser (Brilliant B, Quantel, France) with an optical parametric oscillator (Opotek, 700 to 950 nm) operating at a 10 Hz repetition rate. The light is delivered via a beam expander creating a beam diameter of around 1 cm to cover the sample in a top-illumination configuration (40). An output energy of approximately 20 mJ/cm^2 was used for all scans. The photoacoustic signals are recorded with a curvilinear detector array (Imasonic, Besançon) consisting of 32 elements and shaped to 85º of a circle of 40 mm radius. The center frequency of the array is 6.25 MHz with a reception bandwidth greater than 80%. Individual elements have sizes of 10 by 0.25 mm. These elements are arranged with an inter-element spacing of 1.85 mm. At each position, signals are acquired from the detector using a 32 channel pulse-receiver system (Lecoeur Electronique, Paris, France) with a sampling rate of 80 MHz. Filtered acoustic backprojection was used to reconstruct the PA images.

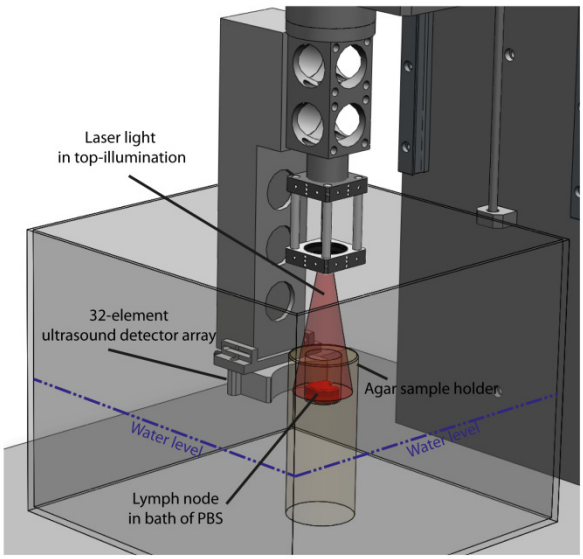

Fig. 3. Schematic of the photoacoustic setup. Lymph node samples are placed inside an agar holder and illuminated from the top while the ultrasound detector is rotated around the sample. The entire setup is placed inside a water filled tank to enable wave propagation.

Images were acquired using an excitation wavelength of 720 nm. While 720 nm is not an exclusive wavelength for detecting SPIO's, it combines a low absorption of total hemoglobin with a significant absorption of the SPIO dispersion, while absorption by fat (and water) remains negligible (41). Furthermore, it allows for a direct comparison with our previous results in healthy animals (34). Image slice acquisition time of the system for 20 projections is about 60 seconds.

In addition to the single wavelength illumination at 720 nm, multiple wavelength images of two lymph nodes were acquired at 720, 740, 760 and 780 nm. Multiple wavelength information could possibly facilitate the distinction of the SPIO deposits from other biological absorbers in an *in vivo* setting. To this end, average pixel value of the PA contrast regions within the images was calculated and compared to spectroscopic values of the SPIO dispersion. For comparison, both the spectroscopic data and the average pixel values within the images were normalized.

5.2.3 Magnetic Resonance Imaging

In order to achieve a comparable spatial resolution to our PA images, the nodes were imaged using a 14 Tesla MRI system (Bruker, Ettlingen, Germany) described earlier (34). Before imaging, the nodes were transferred to quartz NMR tubes with a diameter of 10 mm, and fixated using 4% buffered formaldehyde. All nodes were positioned according to their orientation within the PA setup. A Multi-slice-multi-echo (MSME) imaging sequence was

used with an echo time of 10 ms and a repetition time of 1000 ms. The sequence produces a larger longitudinal and transverse magnetization making the surrounding fat appear bright, while SPIO areas appear dark due to rapid reduction of transverse magnetization. This difference facilitates nodal identification and SPIO distribution analysis in the imaged volume. Images were acquired using a matrix dimension of 256x256, a field of view of 1 cm, 25 averages and a slice thickness of 1 mm. MR scan time mounted up to 2 hours per node.

5.2.4 Contrast quantification

The amount of iron inside the lymphatic tissue was quantified using a vibrating sample magnetometer (VSM) (Quantum Design, San Diego, United States) with a variable magnetic field of ± 4 Tesla. From the measured SPIO amounts a concentration estimation ($\mu g/mm^3$) within each node was calculated by dividing the total iron amount by the volume of the node. Nodal volume was estimated from the dimensions of the nodes in the MR images. The estimated concentration was then correlated to the amount of PA contrast within each nodal image by manually selecting the nodal area within the PA image and calculating the average pixel value of the selection. To exclude large deviations in single pixel values, a 5x5 pixel moving average was first implemented on each PA image. Due to the fact that the detector contains an image slice thickness of approximately 1 mm, the average pixel value (APV) of each selected image region was then divided by its area to produce a "contrast" concentration (APV/mm^3) comparable with the estimated iron concentration.

5.3 Results

A comparison between the PA and MR images for the different animal groups is shown in Figures 4-6. PA imaging of lymph nodes without contrast agent (both benign and metastatic) (Fig. 4) shows that almost no PA response is generated by nodal tissue without the SPIO additive and no clear structures can be distinguished. As a result no clear distinction can be made between nodes with and without metastases. Such a distinction can also not be made based on the corresponding unenhanced MR images. The absence of hypo-intense regions also indicates that no SPIO particles are present within the nodal volume.

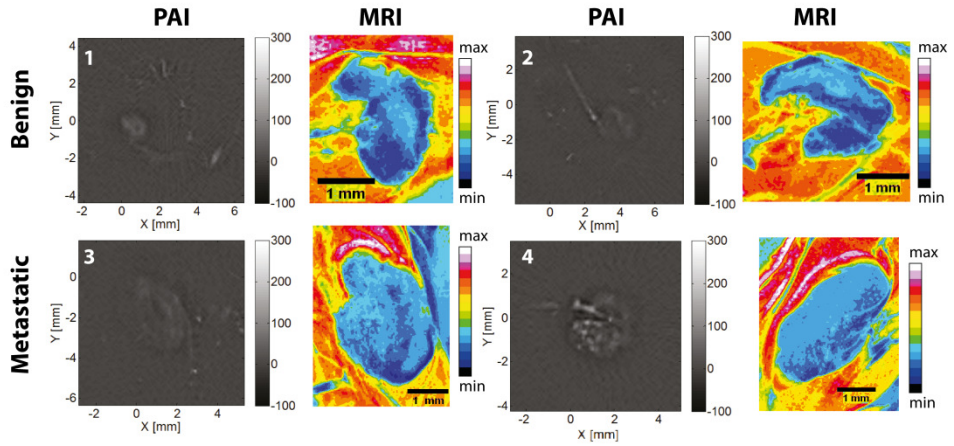

Fig. 4. PA and MR image of benign and metastatic nodes without SPIOs (sham group). PAI maps display PA intensity distributions (a.u.) and MR images show signal intensity (a.u.) obtained with a MSME pulse sequence (see materials & methods). The PA contrast between the tissue and the background is small and the nodes are not easily distinguished. The MR images show no hypointense regions, corresponding with the absence of SPIOs.

The control group (Fig. 5) shows that addition of the SPIOs results in a clear and continuous ring of PA contrast in the peripheral zone of the nodes. The ring like patterns are relatively free of intermissions and show large PA responses throughout their volume compared to the background. The associated MR images contain homogeneous blackening throughout the nodal volume except for the third node (Fig. 5(3), red arrow).

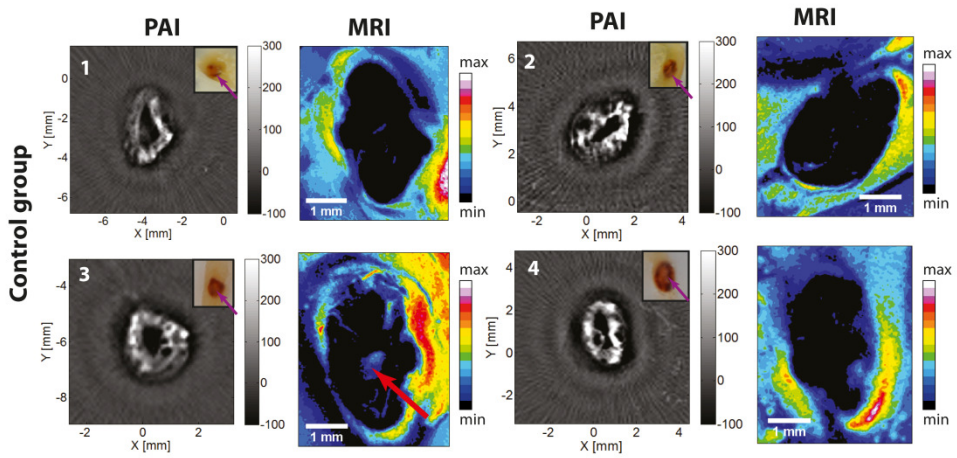

Fig. 5. PA and MR images of the control group. The PA images show a clearly distinguishable continuous high contrast band in the peripheral zone of the nodes while MR images display hypointensity throughout the nodal volume, with exception of node 3 (red arrow). Photos of the paraffin sections show that this discrepancy could be caused by sensitivity differences between both modalities, because the central zone of the nodes display a decreased SPIO deposition (purple arrows).

The blackening within the nodal volume seems to display an uniform distribution and no irregularities are detected. Photos of the paraffin samples show that the discrepancy between MR and PA images could be caused by a sensitivity difference between both modalities as the nodes show a decreased SPIO deposition in their center (Fig. 5, purple arrows) which corresponds with the PA images. Shapes and dimensions correspond for both imaging modalities. The detected iron concentrations measured with VSM varies from 2.9 to 4.2 µg/mm^3 (Table 1). Histology reveals no metastatic cells (Fig. 8(1-3)).

The PA images of the nodes in the major metastatic group (Fig. 6(1-4)) show an altered contrast distribution. There is an absence of a continuous contrast band together with a lowered PA response. The PA signal areas within the images display a discontinuous, irregular distribution with a decreased PA signal response compared to the control nodes (Table 1). MR images show a similar contrast distribution with a lack of hypo-intensity in large areas of the nodal volume (Fig. 6, red arrows). In areas displaying the presence of SPIO contrast, the contrast bands seem to be irregular with hyper intensive spots within

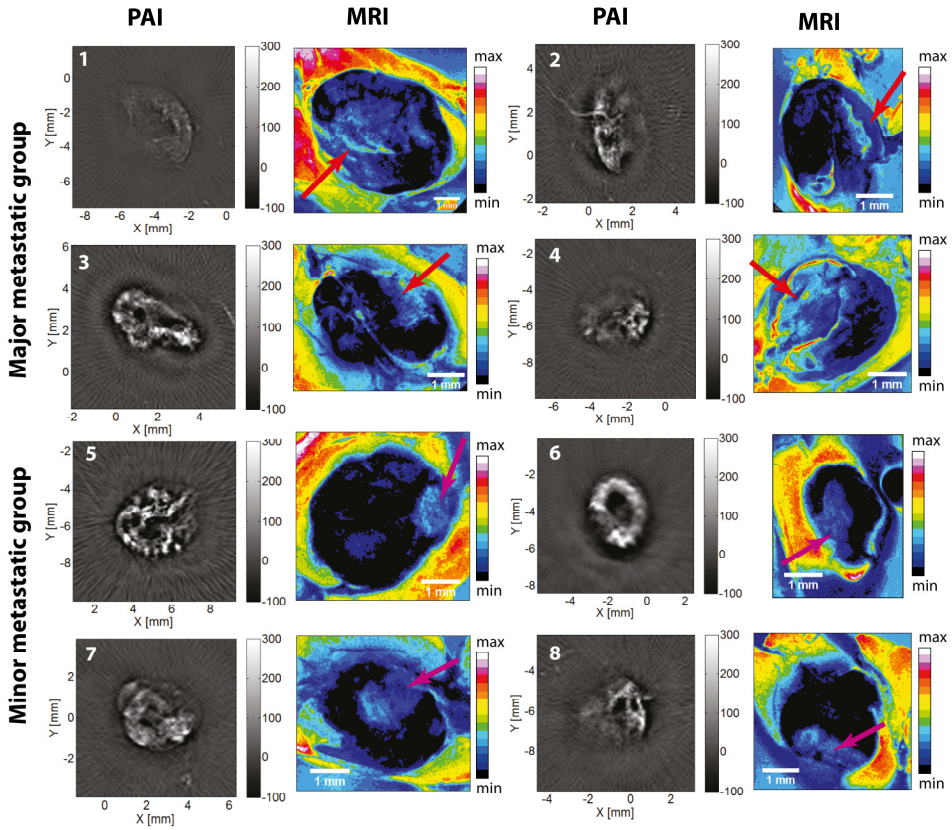

Fig. 6. PA and MR images of the metastatic groups. The PA response pattern is grossly comparable to the areas of MR signal decrease in all the nodes. The contrast distribution is irregular compared to the control group with large areas lacking enhancement, especially in the major metastatic group (Red arrows). MR and PA contrast patterns grossly compare for all the nodes. In contrast to the other nodes, node 6 seems to contain a regular peripheral contrast band with only a small decreased PA response in the lower left quadrant (purple arrow).

these contrast areas. Again there is a clear resemblance in contrast distribution between the MR and PA images, as more clearly displayed by a comparison of the images of lymph node 1 (Fig. 7). Both maps show a similar lack of contrast in the left lower part of the node while an irregular contrast band is located in the upper right. The iron concentration

measured within the nodes of the major metastatic group is also significantly lower compared to the control group with concentrations ranging from 0.4 to 1.0 µg/mm^3 (Table 1). Histology reveals the presence of metastatic cells (Fig. 8(4-6)) in all nodes, although the location of these metastases could not to be matched to all contrast lacking areas in the MR or PA images on a point-to-point basis. This is more clear once the images of lymph node 1 are compared to the vimentin stains (Fig. 7). Although the node shows larger metastatic deposits in the lower peripheral zone of the node (red arrows) compared to the upper part (blue arrows), the vimentin map shows that not all contrast lacking areas correspond to metastatic cell deposits.

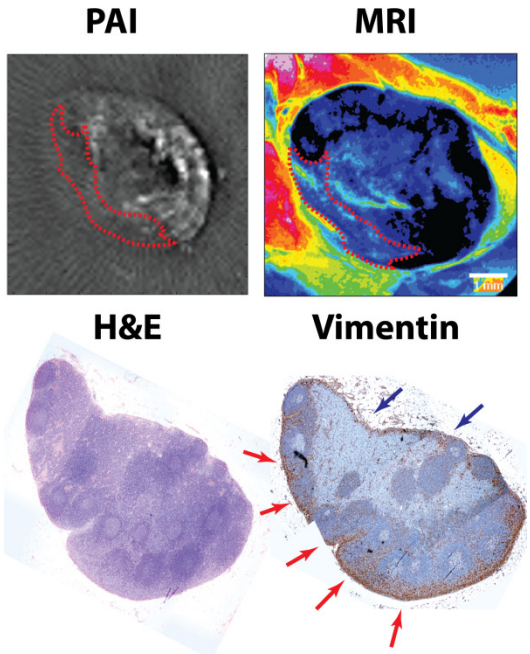

Fig. 7. PA and MR images compared with both H&E and Vimentin histology staining for node 1. The contrast distribution between PA and MR is comparable, showing some SPIOs deposits in the upper parts of the node and absence of SPIOs in the lower parts (Red dotted line). Localization of the metastatic deposits is difficult to correlate to the images using the H&E staining due to lack of contrast between metastatic cells and lymphocytes. Vimentin staining shows the metastatic deposits more clearly (dark brown) and displays a larger amount of metastatic cells in the lower part of the node (red arrows). Some metastatic cells can be detected in the upper part of the node (blue arrows) but deposits are less pronounced.

The PA images of the nodes in the minor metastatic group (Fig. 6(5-8)) do also display irregularities in their contrast distribution and a decreased PA response per mm^3 (Table 1). The amount of PA contrast per mm^3 has however decreased less than within the major metastatic group (Table 1). The corresponding MR images also show areas which lack the hypo-intensity caused by SPIO presence (Fig. 6, purple arrows) and to great extent correlate

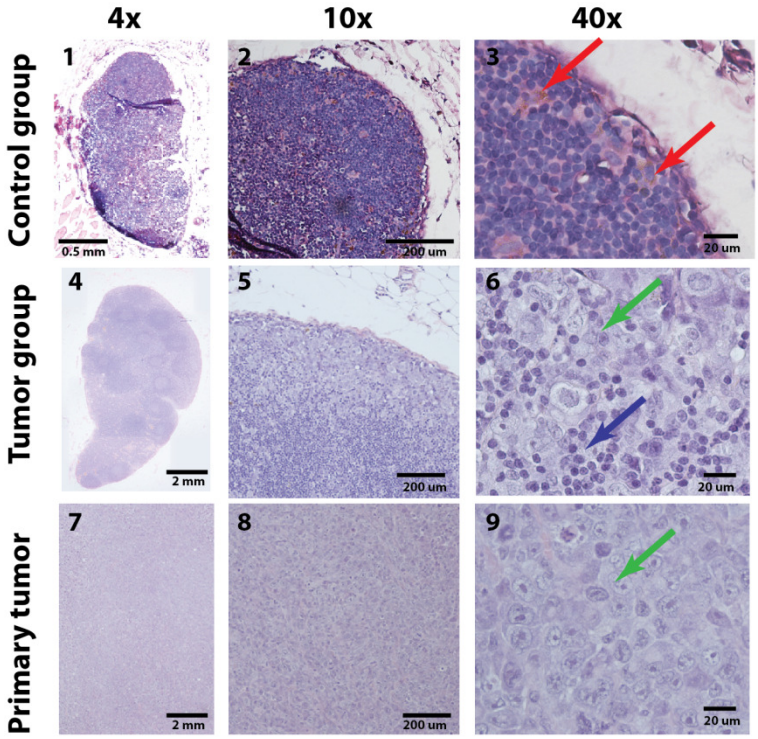

Fig. 8. H&E staining of the control and tumor groups together with the primary tumor at 4x, 10x and 40x magnification. The control nodes show the presence of both lymphocytes and macrophages (1-3). SPIO deposits can be seen within the peripheral zone of the node (red arrows). The nodes in the tumor group show metastatic involvement throughout the nodal volume with larger metastatic deposits in the pheripheral zone (4-6). Normal lymphocytes (blue arrow) can still be located near the metastatic cells (green arrow). The metastasic cells correlate well to the poorly differentiated adenocarcinoma cells of the primary tumor (green arrow) (7-9).

to the absorption patterns of the PA images. However, the hypo-intense areas seem to be less extensively present than within the major metastatic group. Compared to the other nodes within the group, lymph node 6 displays a more regular contrast distribution with only a minor area of SPIO absence in the left peripheral zone (purple area). Measured iron concentrations of the minor metastatic group lie between the control and major metastatic group ranging from 1.1 to 1.8 µg/mm^3 (Table 1.).

Correlation of the calculated APVs with the measured iron concentrations using the least squares approach for all nodes reveals a strong linear relation between the two (Fig. 9), showing a correlation coefficient R=0.94 and a corresponding root mean square of the error (Root MSE) of 1.3. This correlation shows that it could be possible to produce an estimation of the iron concentration by analyzing the PA image contrast within the node. Multiple wavelength imaging of SPIO containing areas in two of the lymph nodes shows an almost constant average PA response for 720, 740, 760 and 780 nm excitation. This constant response agrees with the extinction spectrum of the SPIO dispersion (Fig. 10) which is dissimilar from the varying absorption of hemoglobin in this wavelength range.

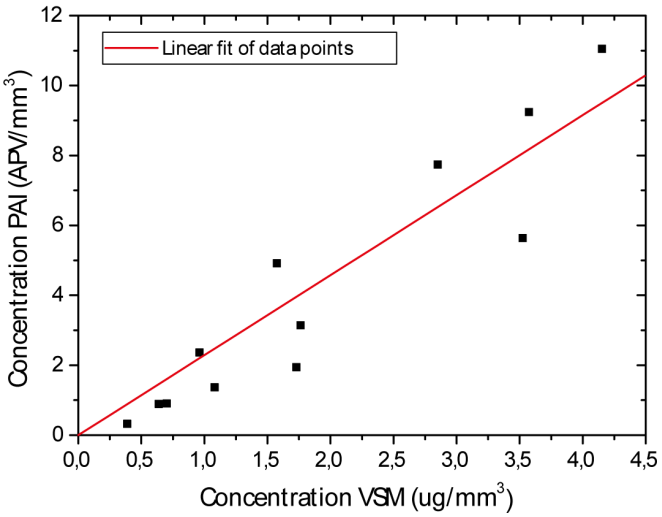

Fig. 9. Correlation between the measured iron concentration with VSM and the calculated PA image contrast. Linear fit through 0,0 of the data points (red line) shows a linear correlation between the two parameters (R=0.94, Root MSE = 1.3).

5.4 Discussion

The results demonstrate that there is a difference in both the PA contrast pattern and the PA intensity between resected rat lymph nodes with and without metastatic deposits after subcutaneous SPIO injection. A regular high intensity PA contrast pattern in the periphery of the nodes seems to correspond to an absence of nodal metastases while the presence of metastatic deposits results in a decline of PA signal intensity and the presence of irregularities in the peripheral contrast band. MR imaging shows a similar trend with the presence of larger areas of hyper-intensity once the tumor inoculation time is prolonged. These findings correspond with the general theory that SPIO uptake in metastatic lymph nodes is altered due to displacement of peripheral macrophages by metastatic cells as explained by Kimura *et al* (42). To our understanding this is the first time that nodal metastases are visualized with PA imaging using a non-specific clinically approved contrast nanoparticle.

However, one-on-one matching of the PA and MR images with histology does prove challenging as shown in Figure 7. This could be explained by small differences in orientation or the fact that MRI and PAI contain slice thicknesses of 1 mm while histological slides are only 5 µm. Its leads us to conclude that PA images should not be viewed as an exact metastatic map, but that alterations in the absorption pattern should be interpreted as indications of metastatic involvement within the nodal volume. Although this might decrease the eventual sensitivity of the technique for smaller metastases, recent data from the American College of Surgeons Oncology Group Z0011 trial gives some indication that small metastatic deposits in lymph nodes are of limited importance for the clinical outcome of, for example, breast cancer patients (43). Although there remains some discussion about the implications of the trial, the fact that the detection of these deposits might be of minor importance compared to macro-metastases, could make the application

of the method for rapid intra-operative screening especially applicable for breast cancer patients. The technique then offers the additional advantage that post-operative analysis remains possible because the tissue is left intact by the imaging procedure and can still be processed for histology. This would then permit additional lymph node removal once histology reveals that metastases have been missed.

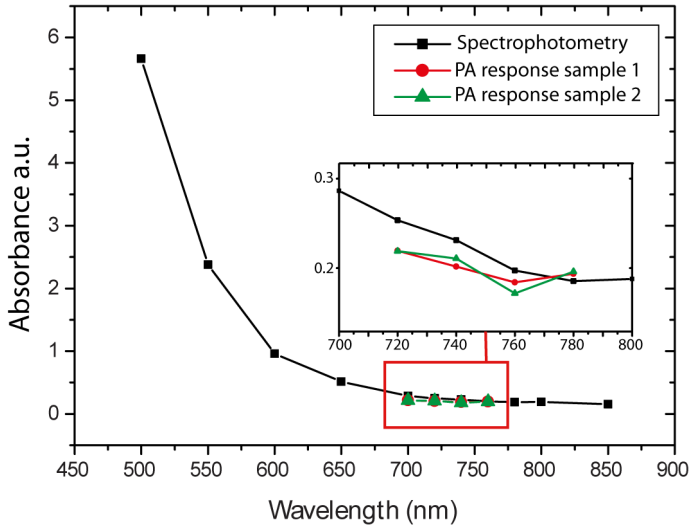

Fig. 10. Correlation between the optical extinction of a SPIO dispersion measured with optical spectroscopy (black line) compared to the amount of PA response from two lymph nodes at 4 different excitation wavelengths (green and red line). With the absorbance displayed on a logarithmic scale, the zoomed graph shows that both the optical absorption and PA response are almost constant at the wavelength range from 720 to 780 nm. This constant absorption is not present in other biological chromophores, which might offer additional grounds to distinguish

In contrast to the indication that a regular PA contrast distribution combined with a high signal intensity seems to correspond to a healthy node, one of the metastatic nodes, namely number 6, also shows a relatively regular and intensive PA band. The absence of contrast in the lower left part of the node (purple arrow) represents the only irregular observation in both PAI and MRI, making it challenging to define to which extent metastases have to be progressed before they can be sensitively detected with this approach. On the other hand, small areas of PA signal absence in benign nodes might also lead to a wrong metastatic diagnosis which could give the technique a higher false positive rate. These unknowns warrant the claim for additional research with larger sample numbers on lymph nodes harboring early metastatic involvement could provide more information whether in most cases the metastatic induced phagocytotic changes will result in detectable alterations of the PA contrast map and how this has impact on the sensitivity and specificity of the technique.

The MR and PA images show clear similarities in the distribution of SPIO contrast, indicating that SPIO distributions can also be accurately mapped using photoacoustics. With regard to image quality, the MRI system is superior compared to the tomographic PA system ,but it has to be taken into account that MR image acquisition requires several hours. Furthermore, a comparable MR setup is not only expensive and bulky but also contains a strong magnetic field which is unsuitable for an intra-operative setting. These advantages emphasize the possible additional benefit of a PA approach.

Table 1. Measured SPIO concentrations and PA contrast within the individual nodes. Nodal numbers correspond to the numbering within the figures.

Control nodes	**Iron concentration VSM (ug/mm^3)**	**PA contrast in image (mm^{-3})**
1	2,9	13,0
2	3,5	9,6
3	4,2	15,6
4	3,6	15,0
Metastatic nodes	**Iron concentration VSM (ug/mm^3)**	**PA contrast in image (mm^{-3})**
1	0,4	0,8
2	0,6	2,5
3	1,0	5,4
4	0,7	3,8
5	1,6	8,4
6	1,1	6,8
7	1,8	7,5
8	1,7	6,5

The decrease in PA intensity within the metastatic nodes corresponds to a measured decrease in iron concentration (Table 1). The iron concentrations measured with VSM show a decline in SPIO uptake depending on the length of the primary tumor inoculation time. PA contrast amounts are shown to have a strong linear relationship (R=0.94) with the iron concentrations indicating that the PA intensity could be converted into an estimation for the iron amount. Although this remains to be a qualitative estimation because the actual photon fluence within the tissue is unknown, more quantitative approaches could possibly be implemented including an ultrasound modulated fluence correction approach (44). For now, the fact that PA intensity per mm^3 seems to be decreased in metastatic nodes, which can be linked to a decreased iron concentration, shows that PA intensity measurements could possibly be used as an additional tool for nodal assessment.

The fact that the control lymph nodes are smaller and contain less immune cells than the nodes within the tumor groups could raise some questions about the applicability of the technique for large reactive nodes. These nodes could for example be present once the

immune system reacts to the presence of a primary tumor. Although we stress the importance of further research, results in a healthy animal model in which reactive nodes were induced by incomplete Freund Adjuvant injection also showed the presence of regular high intensity peripheral PA contrast bands (34). This seems to indicate that the uptake of SPIOs by the peripheral macrophages is unaltered even if tumor induced reactivity results in the presence of more immune cells and swelling of the node. The technique might therefore also be suitable for larger or activated lymph nodes.

Finally, even though the results demonstrate the potential of an intra-operative PA application for resected *ex vivo* nodal staging, the use of SPIOs in an *in vivo* setting could also be considered. In such a setting, the fact that smaller SPIO deposits generate lower PA response (45) could be compensated by differentiation on the basis of multiple wavelength excitation. The constant PA response of the SPIOs in the near-infrared (Fig. 10) is dissimilar from the varying absorption of oxy- and deoxyhemoglobin, providing some grounds to separate the PA signals of both. Future research will be directed towards such a spectral method, which should verify if SPIOs could also contain *in vivo* applicability.

5.5 Conclusion

The use of a tomographic PA setup together with a subcutaneously injected, clinically approved SPIO dispersion is capable of distinguishing benign from metastatic nodes in an *ex vivo* setting. Indications for metastatic involvement seem to be a lowered and irregular PA intensity pattern which can be linked to a decreased SPIO concentration and distribution. These results pave the way for a clinical exploratory study into the accuracy of the technique for intra-operative staging.

5.6 References

1. Govindarajan A, Baxter NN. Lymph node evaluation in early-stage colon cancer. Clin Colorectal Cancer 2008; 7(4):240-246.
2. Giuliano AE, Kirgan DM, Guenther JM, Morton DL. Lymphatic mapping and sentinel lymphadenectomy for breast cancer. Ann Surg 1994; 220(3):391-398; discussion 398-401.
3. Morton DL, Wen DR, Wong JH, Economou JS, Cagle LA, Storm FK, Foshag LJ, Cochran AJ. Technical details of intraoperative lymphatic mapping for early stage melanoma. Arch Surg 1992; 127(4):392-399.
4. Liptay MJ. Sentinel node mapping in lung cancer. Ann Surg Oncol 2004; 11(3 Suppl):271S-274S.
5. Balch CM, Soong SJ, Gershenwald JE, Thompson JF, Reintgen DS, Cascinelli N, Urist M, McMasters KM, Ross MI, Kirkwood JM, Atkins MB, Thompson JA, Coit DG, Byrd D, Desmond R, Zhang Y, Liu PY, Lyman GH, Morabito A. Prognostic factors analysis of 17,600 melanoma patients: validation of the American Joint Committee on Cancer melanoma staging system. J Clin Oncol 2001; 19(16):3622-3634.

6. Krag DN, Single RM. Breast cancer survival according to number of nodes removed. Ann Surg Oncol 2003; 10(10):1152-1159.
7. Harisinghani MG, Barentsz J, Hahn PF, Deserno WM, Tabatabaei S, van de Kaa CH, de la Rosette J, Weissleder R. Noninvasive detection of clinically occult lymph-node metastases in prostate cancer. N Engl J Med 2003; 348(25):2491-2499.
8. Will O, Purkayastha S, Chan C, Athanasiou T, Darzi AW, Gedroyc W, Tekkis PP. Diagnostic precision of nanoparticle-enhanced MRI for lymph-node metastases: a meta-analysis. Lancet Oncol 2006; 7(1):52-60.
9. Clement O, Siauve N, Cuenod CA, Frija G. Liver imaging with ferumoxides (Feridex): fundamentals, controversies, and practical aspects. Top Magn Reson Imaging 1998; 9(3):167-182.
10. Taupitz M, Wagner S, Hamm B. Contrast media for magnetic resonance tomographic lymph node diagnosis (MR lymphography). Radiologe 1996; 36(2):134-140.
11. Wang LV, Hu S. Photoacoustic tomography: in vivo imaging from organelles to organs. Science 2012; 335(6075):1458-1462.
12. Razansky D, Deliolanis NC, Vinegoni C, Ntziachristos V. Deep tissue optical and optoacoustic molecular imaging technologies for pre-clinical research and drug discovery. Curr Pharm Biotechnol 2012; 13(4):504-522.
13. Heijblom M, Piras D, Xia W, van Hespen JC, Klaase JM, van den Engh FM, van Leeuwen TG, Steenbergen W, Manohar S. Visualizing breast cancer using the Twente photoacoustic mammoscope: What do we learn from twelve new patient measurements? Opt Express 2012; 20(11):11582-11597.
14. Ermilov SA, Khamapirad T, Conjusteau A, Leonard MH, Lacewell R, Mehta K, Miller T, Oraevsky AA. Laser optoacoustic imaging system for detection of breast cancer. J Biomed Opt 2009; 14(2):024007.
15. Kruger RA, Lam RB, Reinecke DR, Del Rio SP, Doyle RP. Photoacoustic angiography of the breast. Med Phys 2010; 37(11):6096-6100.
16. Jaeger M, Preisser S, Kitz M, Ferrara D, Senegas S, Schweizer D, Frenz M. Improved contrast deep optoacoustic imaging using displacement-compensated averaging: breast tumour phantom studies. Phys Med Biol 2011; 56(18):5889-5901.
17. O'Brien CM, Rood K, Sengupta S, Gupta SK, DeSouza T, Cook A, Viator JA. Detection and isolation of circulating melanoma cells using photoacoustic flowmetry. J Vis Exp 2011(57):e3559.
18. Jose J, Grootendorst DJ, Vijn TW, Wouters M, van Boven H, van Leeuwen TG, Steenbergen W, Ruers TJ, Manohar S. Initial results of imaging melanoma metastasis in resected human lymph nodes using photoacoustic computed tomography. J Biomed Opt 2011; 16(9):096021.
19. Grootendorst DJ, Jose J, Wouters MW, van Boven H, Van der Hage J, Van Leeuwen TG, Steenbergen W, Manohar S, Ruers TJ. First experiences of photoacoustic imaging for detection of melanoma metastases in resected human lymph nodes. Lasers Surg Med 2012; 44(7):541-549.
20. Luke GP, Yeager D, Emelianov SY. Biomedical applications of photoacoustic imaging with exogenous contrast agents. Ann Biomed Eng 2012; 40(2):422-437.

21. Manohar S, Ungureanu C, Van Leeuwen TG. Gold nanorods as molecular contrast agents in photoacoustic imaging: the promises and the caveats. Contrast Media & Mol Imaging 2011; 6(5):389-400.
22. Lanza GM. Emerging contrast agents for photoacoustic imaging. Contrast Media Mol Imaging 2011; 6(5):331.
23. Kosaka N, Bernardo M, Mitsunaga M, Choyke PL, Kobayashi H. MR and optical imaging of early micrometastases in lymph nodes: triple labeling with nano-sized agents yielding distinct signals. Contrast Media Mol Imaging 2012; 7(2):247-253.
24. Ballou B, Ernst LA, Andreko S, Harper T, Fitzpatrick JA, Waggoner AS, Bruchez MP. Sentinel lymph node imaging using quantum dots in mouse tumor models. Bioconjug Chem 2007; 18(2):389-396.
25. Yang K, Hu L, Ma X, Ye S, Cheng L, Shi X, Li C, Li Y, Liu Z. Multimodal imaging guided photothermal therapy using functionalized graphene nanosheets anchored with magnetic nanoparticles. Adv Mater 2012; 24(14):1868-1872.
26. Song KH, Kim C, Maslov K, Wang LV. Noninvasive in vivo spectroscopic nanorod-contrast photoacoustic mapping of sentinel lymph nodes. Eur J Radiol 2009; 70(2):227-231.
27. Song KH, Stein EW, Margenthaler JA, Wang LV. Noninvasive photoacoustic identification of sentinel lymph nodes containing methylene blue in vivo in a rat model. J Biomed Opt 2008; 13(5):054033.
28. Erpelding TN, Kim C, Pramanik M, Jankovic L, Maslov K, Guo Z, Margenthaler JA, Pashley MD, Wang LV. Sentinel lymph nodes in the rat: noninvasive photoacoustic and US imaging with a clinical US system. Radiology 2010; 256(1):102-110.
29. Galanzha EI, Shashkov EV, Spring PM, Suen JY, Zharov VP. In vivo, noninvasive, label-free detection and eradication of circulating metastatic melanoma cells using two-color photoacoustic flow cytometry with a diode laser. Cancer Res 2009; 69(20):7926-7934.
30. Akers WJ, Edwards WB, Kim C, Xu B, Erpelding TN, Wang LV, Achilefu S. Multimodal sentinel lymph node mapping with single-photon emission computed tomography (SPECT)/computed tomography (CT) and photoacoustic tomography. Transl Res 2012; 159(3):175-181.
31. Pan D, Cai X, Yalaz C, Senpan A, Omanakuttan K, Wickline SA, Wang LV, Lanza GM. Photoacoustic sentinel lymph node imaging with self-assembled copper neodecanoate nanoparticles. ACS Nano 2012; 6(2):1260-1267.
32. McLaughlin RA, Scolaro L, Robbins P, Hamza S, Saunders C, Sampson DD. Imaging of human lymph nodes using optical coherence tomography: potential for staging cancer. Cancer Res 2010; 70(7):2579-2584.
33. Horsnell JD, Smith JA, Sattlecker M, Sammon A, Christie-Brown J, Kendall C, Stone N. Raman spectroscopy - A potential new method for the intra-operative assessment of axillary lymph nodes. Surgeon 2012; 10(3):123-127.
34. Grootendorst DJ, Jose J, Fratila RM, Visscher M, Velders AH, Ten Haken B, Van Leeuwen TG, Steenbergen W, Manohar S, Ruers TJ. Evaluation of superparamagnetic iron oxide nanoparticles (Endorem(R)) as a photoacoustic contrast agent for intra-operative nodal staging. Contrast Media Mol Imaging 2013; 8(1):83-91.

35. Vassallo P, Matei C, Heston WD, McLachlan SJ, Koutcher JA, Castellino RA. Characterization of reactive versus tumor-bearing lymph nodes with interstitial magnetic resonance lymphography in an animal model. Invest Radiol 1995; 30(12):706-711.
36. Klerkx WM, Geldof AA, Heintz AP, van Diest PJ, Visser F, Mali WP, Veldhuis WB. Longitudinal 3.0T MRI analysis of changes in lymph node volume and apparent diffusion coefficient in an experimental animal model of metastatic and hyperplastic lymph nodes. J Magn Reson Imaging 2011; 33(5):1151-1159.
37. Cengelli F, Maysinger D, Tschudi-Monnet F, Montet X, Corot C, Petri-Fink A, Hofmann H, Juillerat-Jeanneret L. Interaction of functionalized superparamagnetic iron oxide nanoparticles with brain structures. J Pharmacol Exp Ther 2006; 318(1):108-116.
38. Wang YX, Hussain SM, Krestin GP. Superparamagnetic iron oxide contrast agents: physicochemical characteristics and applications in MR imaging. Eur Radiol 2001; 11(11):2319-2331.
39. Jose J, Willemink RG, Resink S, Piras D, van Hespen JC, Slump CH, Steenbergen W, van Leeuwen TG, Manohar S. Passive element enriched photoacoustic computed tomography (PER PACT) for simultaneous imaging of acoustic propagation properties and light absorption. Opt Express 2011; 19(3):2093-2104.
40. Lao Y, Xing D, Yang S, Xiang L. Noninvasive photoacoustic imaging of the developing vasculature during early tumor growth. Phys Med Biol 2008; 53(15):4203-4212.
41. Beard P. Biomedical photoacoustic imaging. Interface Focus 2011; 1(4):602-631.
42. Kimura K, Tanigawa N, Matsuki M, Nohara T, Iwamoto M, Sumiyoshi K, Tanaka S, Takahashi Y, Narumi Y. High-resolution MR lymphography using ultrasmall superparamagnetic iron oxide (USPIO) in the evaluation of axillary lymph nodes in patients with early stage breast cancer: preliminary results. Breast Cancer 2010; 17(4):241-246.
43. Galimberti V, Chifu C, Rodriguez Perez S, Veronesi P, Intra M, Botteri E, Mastropasqua M, Colleoni M, Luini A, Veronesi U. Positive axillary sentinel lymph node: is axillary dissection always necessary? Breast 2011; 20 Suppl 3:S96-98.
44. Daoudi K, Hussain A, Hondebrink E, Steenbergen W. Correcting photoacoustic signals for fluence variations using acousto-optic modulation. Opt Express 2012; 20(13):14117-14129.
45. Mienkina MP, Friedrich CS, Hensel K, Gerhardt NC, Hofmann MR, Schmitz G. Evaluation of Ferucarbotran (Resovist) as a photoacoustic contrast agent / Evaluation von Ferucarbotran (Resovist) als photoakustisches Kontrastmittel. Biomed Tech (Berl) 2009; 54(2):83-88.

CHAPTER 6

APPLICATION OF CARBON NANOPARTICLES FOR PHOTOACOUSTIC DETECTION OF LYMPH NODE METASTASES

Detection of tumor metastases in the lymphatic system is essential for accurate staging of malignancies. Photoacoustic (PA) and MRI based differentiation between metastatic and benign lymph nodes can be achieved through the addition of clinical grade nanoparticle dispersions containing iron oxide cores. However, the expense and limited optical absorption of these particles makes them less ideal for PA nodal staging alone. We therefore verify in an animal model whether carbon nanoparticle dispersions, characterized by a higher optical absorption, can be used to facilitate PA intra-operative nodal staging. Experiments are mainly focused on the use of these particles for intra-operative *ex vivo*, however their potential for superficial nodal staging is also explored. Results show that *ex vivo* nodal staging using carbon nanoparticle dispersions can be performed successfully and is able to distinguish both normal and hypertrofic lymph nodes from metastatic nodes, based on their PA maps. Differentiation between unresected benign and metastatic nodes, at a depth of 1 cm beneath the skin, however remains challenging due to the absence of sufficient signal in both types of nodes. We conclude that carbon nanoparticle dispersions can be used to facilitate PA *ex vivo* nodal staging which could make them applicable in a intra-operative setting.

.

6.1 Introduction

Exogeneous agents are applied throughout all fields of medical imaging to enhance the contrast between the tissue of investigation and its surroundings. In oncology, their application is of the greatest importance to accurately stage and monitor the progress of multiple malignancies. So are gadolinium based contrast fluids routinely used to enhance Magnetic Resonance Images (MRI) of neurological, hepatic, or renal malignancies (1) while iodine based agents are applied to support the visualization of for example lung cancer nodules (2). As it is well known that the presence of lymph node metastases has a great influence on the treatment and survival (3) of patients suffering from various malignancies, research into agents which could aid in the visualization of these metastases was already initiated in the early nineties (4,5). Pieterman et al. (6) demonstrated that sensitivity and specificity of PET after administration of 18F-FDG was superior to unenhanced CT in detecting malignant lymph nodes and staging of lung cancer. A combination of PET and CT increased the accuracy of staging even more (7). For nodal staging in prostate cancer 11C-Acetate and 11C-methionine have shown to be more useful then 18F-FDG (8,9). In the area of MRI, consecutive years of research resulted in the introduction of iron oxide based contrast materials for pre-operative nodal staging. Several groups obtained valuable information about the safety of the applied agents (10,11) and their additional value in the detection of nodal metastases using MRI (12). So called, ultra-small superparamagnetic iron oxide (USPIO) nanoparticles proved to increase the sensitivity and specificity for detection of lymph-node metastases throughout the human body, while iron oxide nanoparticles with slightly larger cores (SPIOs) proved to be of additional benefit for regional lymph node staging in breast cancer (13). The concept behind the application of USPIOs and SPIOs was first shown by Weissleder *et al* (14), who verified that while macrophages in benign lymph nodes internalize these nanoparticles, the displacement of these macrophages by metastatic cells ensures a decreased uptake. MRI is able to visualize this difference because of the change in relaxation time induced by the iron oxide cores of the material.

Recently our group demonstrated that SPIO particles could also be of additional benefit for nodal staging using photoacoustic (PA) imaging, a technique utilizing ultrasound detection after short pulsed laser excitation (15). Illumination of nodal tissue containing SPIO's results in a thermo elastic expansion due to an increased absorption, generating a detectable ultrasound wave. Because of the relatively small scattering of ultrasound waves compared to photons, a high resolution can be maintained up to several centimeters beneath the tissue surface (16-18). Compared to SPIO particles, carbon nanoparticles are even more prone to thermo elastic expansion due to their increased absorption in the near-infrared (19,20) which could result in larger PA signals at lower concentrations. The non-clinical status of carbon particles also makes them inexpensive to manufacture compared to commercially produced clinical SPIO dispersions ($2000, 8ml). Nodal mapping using carbon nanoparticles has already been investigated in abdominal surgery, where colonic lesions

routinely are being mapped using a carbon nanoparticle dispersion, like India Ink (21). The long term safety of the routine has been verified extensively and the particles have been found safe to use for colonic marking (22). Kumashiro *et al* (23) furthermore showed that carbon dispersions can be injected safely into patients undergoing a radical lymphadectomy for rectal cancer, facilitating the discernability of the nodes and resulting in less nerve damage during resections. Subdermal injection of carbon particles in the breast was also shown to improve intra-operative mapping of lymph nodes during radical mastectomies while showing no adverse reactions (24). A similar approach has been studied for gastric cancer resulting in a larger number of lymph nodes to be identified and dissected (25). It was also found that metastatic lymph nodes had an intact lymphatic system allowing carbon particles to reach them as efficiently as non-metastatic nodes. However, systematic validation of the staging potential of carbon nanoparticles has not been performed and it is unknown whether these particles are able to produce a similar staging improvement as iron oxide based agents. Here we verify whether carbon nanoparticle dispersions can be used for photoacoustic regional lymph node staging. Performance is being studied in a metastatic animal model both *ex vivo* and *in corpore*, in euthanized animals. Results are compared to SPIOs and conclusions are drawn regarding the clinical application potential of carbon nanoparticles.

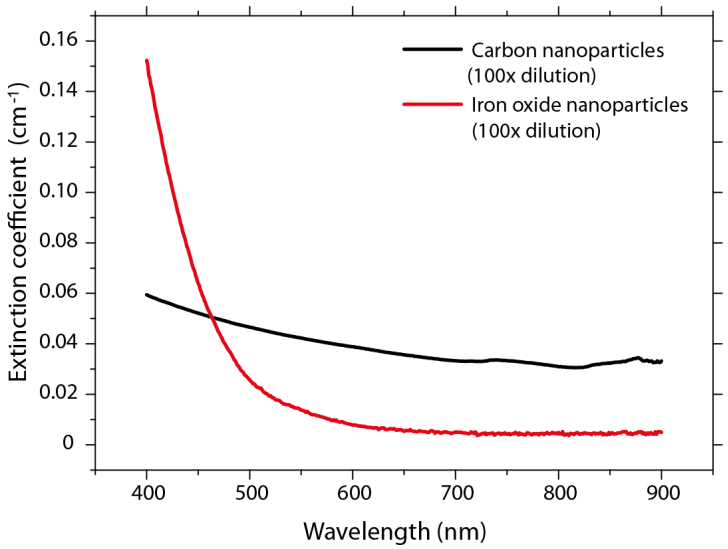

Fig. 1. Extinction spectra of both iron and carbon nanoparticle dispersions (100x diluted). Both nanoparticles display a decline in extinction with an increase in excitation wavelength.

6.2 Materials and Methods

6.2.1 Animal protocol

Carbon nanoparticles were produced by diluting 1 ml of India Ink (Rotring, Hamburg, Germany) in 9 ml phosphate buffered saline solution. The dispersion was filtered utilizing a 0.2 µm polymer filter, to guarantee sterilization and the exclusion of nanoparticles larger than 200 nm. The extinction spectrum of the dispersion after an additional 100 times dilution is depicted in Figure 1, together with the extinction spectrum of iron oxide nanoparticles (Endorem®, Guerbet, France).

In order to analyze the potential of carbon nanoparticles for photoacoustic nodal staging, a metastatic animal model was used and approved according to the Dutch animal welfare guidelines. Four female Copenhagen rats (± 200 g) were subcutaneously inoculated with one million highly metastatic prostate carcinoma (MAT-lylu) cells in the left hindpaw. Cells were cultured in RPMI-1640 medium, supplemented with 10% fetal calf serum and 100 ml penicillin/streptomycin. After 8 days of inoculation, 0.1 ml of the carbon dispersion was injected subcutaneously around the primary tumor and in the opposite hindpaw. This was done, so the popliteal nodes on the contra lateral side could be used as controls, as previously shown possible by Vassallo *et al* (26). In order investigate the effect of aspecific immune stimulation of lymph nodes, two female Wistar rats (± 400 g) were injected with 0.1 ml of Incomplete Freund Adjuvant (IFA) instead of tumor cells in both hindpaws. This was done since reactive non-tumor harbouring lymph nodes, could be present in a situation where the presence of primary tumor has resulted in the activation of the immune system, as is the case in many oncological patients. From both animal groups, the lymph nodes were resected 24 hours after carbon injection and freshly imaged using photoacoustic tomography. The animal protocol resulted in 12 nodes to be resected, 4 metastatic, 4 reactive and 4 control. After imaging the nodes were fixated in 4% formaldehyde and histologically processed using H&E staining. Photographs of the paraffin blocks were made to provide some indication of the carbon distribution within the node.

6.2.2 Photoacoustic imaging

All resected lymph nodes were placed inside a hollow transparent 3% Agar sample holder with an inner diameter of 25 mm and wall thickness of 10 mm. Twenty tomographic projections were acquired at approximately 20 mJ/cm^2 using the instrument we described previously (Fig. 2A) (27) . An illumination wavelength of 720 nm was chosen to compare the imaging results with those obtained using SPIO particles. Filtered acoustic backprojection was used to reconstruct the images. After reconstruction the average signal quantity within the different groups was estimated by calculating the mean pixel intensity within the nodes and averaging it across the group. The pixel intensity of each node was calculated by averaging all the pixels above background level, within the nodal outline. Calculations were performed using Matlab based software.

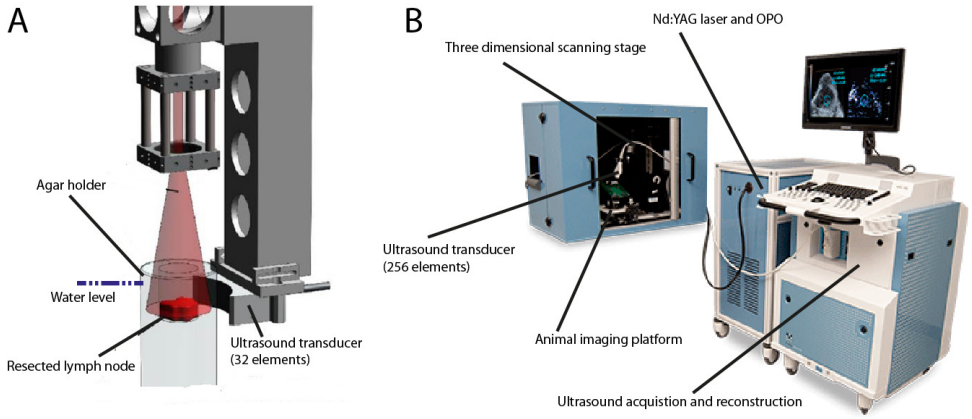

Fig. 2. Overview of the tomographic photoacoustic setup (A) and the VEVOLAZR imaging system (B)

In addition to the *ex vivo* image protocol, two metastatic animals were imaged directly after euthanization while the nodes still remained in the body, using the hand-held VEVOLAZR photoacoustic setup (Visualsonics, Ontario, Canada) (Fig. 2B). This setup proved capable of real-time acquisition of the photoacoustic signal while enabling a direct ultrasound overlay to facilitate the identification of anatomical structures. To facilitate PA imaging the animal was carefully shaved while keeping the skin intact. After placing the transducer on the inguinal area between tail and paw and enabling image acquisition with ultrasound gel contact, a volume scan of the area containing the popliteal node was made using mechanically translocated B-Mode scanning with an inter-slice distance of 200 µm. A comparable excitation wavelength of 720 nm was used and all images were acquired at approximately 20 mJ/cm^2. Image acquisition time of the system proved to be 0.2 s for a 2D image and 74 seconds for a 3D volume scan of 10 mm. To verify these *in corpore* image results, the nodes were also scanned after resection by embedding them in ultrasound gel and performing a comparable volume scan. After imaging, the metastatic nodes were processed in a similar way as the other lymph node samples. In addition, they were immunohistochemically stained with Vimentin to improve the correlation of metastatic cell clusters with the PA images.

6.3 Results

Tomographic photoacoustic imaging of the control nodes (Fig. 3(A-D)) shows that most signal is generated in the nodal border and the contrast of the nodal center is lowered compared to the background. Generated signal quantities are not totally homogeneous throughout the peripheral zone for nodes A and B (yellow arrows), where nodes C and D show fairly regular signal distributions. For all nodes, the size can be easily depicted and no areas in the peripheral zone remain unenhanced. The average mean pixel intensity within the control nodes proves to be approximately 200. Corresponding photographs of the paraffin blocks are difficult to interpret due to the small sizes of the nodes but show the

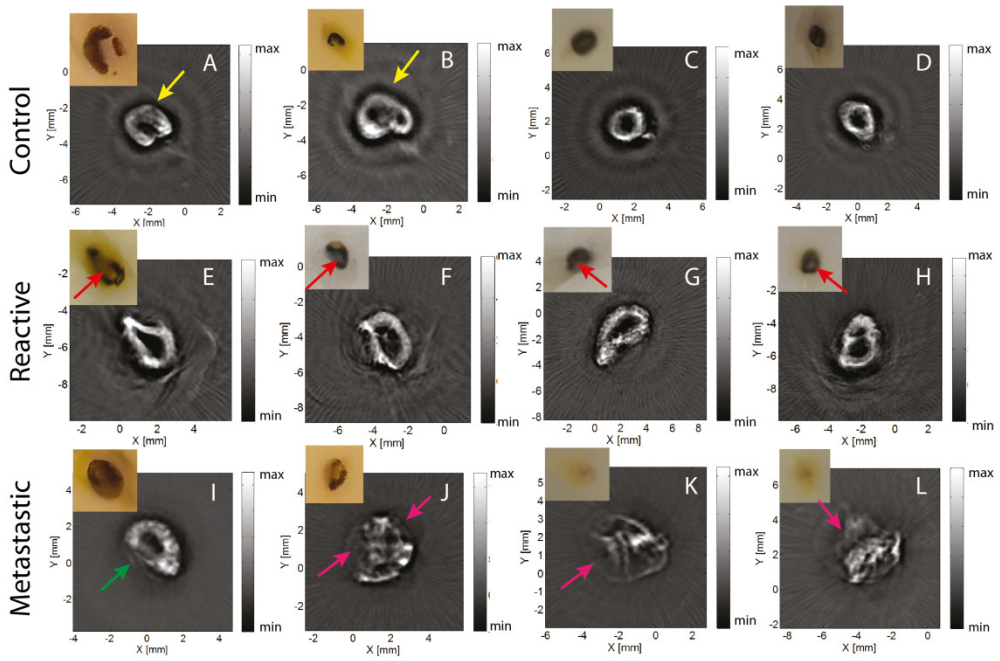

Fig. 3. Photoacoustic images of the three different lymph node groups together with a corresponding photos of the paraffin blocks. PA images of the control lymph nodes (A-D) show a relatively homogeneous contrast distributions and a lack of signal in the centre of the nodes. A slight signal decrease can be noted in nodes A and B (yellow arrows). Photos show the presence of carbon nanoparticles within all the control nodes (brown/black discoloring) and display a decrease of carbon deposition in the center of the nodal outline which explains the lower signal intensities at these locations. PA images of the reactive lymph nodes (E-H) display a similar distribution with regular contrast deposition in the peripheral zone of all the nodes. The lack of contrast in the center of the nodes corresponds with an absence of carbon particles at these locations (red arrows). PA images of the metastatic nodes (I-L) show the absence of a regular distribution and multiple areas of decreased signal intensity (pink arrows). This irregular distribution is less pronounced in the PA image of node I, although an absence of signal can be seen in the lower left quadrant (green arrow).

presence of carbon nanoparticles within the nodal volume (Fig 3A. Blue arrow). Histology (Fig. 4(A,D)) verifies that all nodes are unreactive node without an increased presence of immune cells or metastatic deposits. Phagocytosed carbon nanoparticles can be distinguished within the peripheral zones of the nodes (Fig. 4D).

Photoacoustic imaging of the reactive nodes (Fig. 3(E-H)) which are larger in size (long axis ± 4-5 mm compared to 1-2 mm), depicts clear and continuous signal bands in the peripheral zone of the nodal volume. The center of the nodes remains unenhanced which corresponds well with the corresponding photographs of the paraffin blocks where the center of the nodes also lack the presence of carbon particles (red arrows). The average

pixel intensity within the nodal volume is higher compared to the control nodes (approximately 450 to 200) which is mainly caused by the large contribution of lymph node E. If it was left out of the comparison, average pixel intensities are more or less comparable (approximately 150 to 200) which might indicate that the activation of the immune system does not influence the amount of nanoparticle uptake significantly. Histology (Fig. 4(B,E)) reveals clusters of activated B-plasma cells (red arrow) together with an increased total number of lymphocytes (green arrow) corresponding to an activated immune response and a swelling of the node. No metastatic cells were located.

The metastatic nodes (Fig. 3(I-L)) correspond in size with the reactive nodes but reveal an irregular PA response pattern with areas of lower and higher contrast throughout the nodal volume. The PA maps correspond poorly to the homogeneously distributed contrast maps of both the control and the reactive nodes with large areas of contrast absence within the peripheral zone (pink arrows). These irregularities are less distinct in the photoacoustic scan of lymph node I which shows a regular distribution only lacking signal in its lower half (green arrow). The corresponding photographs of the paraffin blocks also show a lack of carbon deposits in several locations for nodes I and J where the paraffin blocks of nodes K

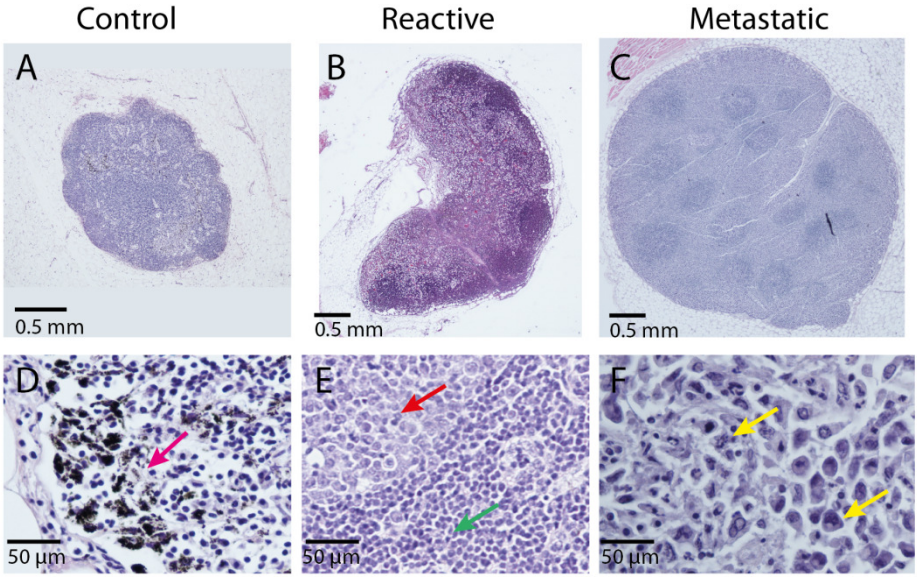

Fig. 4. H&E stainings of the different lymph node groups. The control nodes (A,D) are relatively small and display the presence of carbon nanoparticle deposits in the nodal cortex (pink arrow). These particles are all phagocytosed by nodal macrophages. The nodes are devoid of any large B-cell follicles. The reactive nodes (B,E) display an increased size and the presence of many B-cells (red arrow) together with thickly packed T-cells (green arrow). The metastatic nodes (C,F) also show an increased size and appear to be more rounded. Numerous poorly differentiated metastatic cells can be located throughout the nodal volume, displaying an increased size, multiple mitotic figures and deformed nuclei (yellow arrows).

and L almost show no deposits at all. The amount of PA response is relatively comparable to that generated within the benign and reactive nodes (approximately 150). Histology (Fig. 4(C,F)) depicts numerous metastatic cells especially in the peripheral zone of the nodes. The tissue displays a high number of mitotic figures and the cells are enlarged and poorly differentiated (yellow arrows) corresponding with the characteristics of the MAT-lylu adenocarcinoma. In addition, the nodal outline is more rounded which characterizes metastatic lymph nodes (Fig. 4C).

During *in corpore* photoacoustic imaging of the two euthanized animals using the VEVOLAZR system, lymph nodes could be easily located in the inguinal area. Together with image acquisition, the total scan time did not exceed 15 minutes. The ultrasound overlay enabled the identification of several anatomical structures in the inguinal zone while the nodal outline could be easily tracked due to the hypo intensity of the nodal tissue (Fig. 5(A,B,) white dotted line). Correlation of the PA signal with the anatomical location of the deposits was significantly improved using this overlay. Hybrid imaging shows an inhomogeneous contrast distribution within the nodal volume of the metastatic nodes (Fig. 5(A-B)) with large areas lacking any PA signal generation. Minor PA signal amounts however, can be observed in the upper part of both nodes (pink and green arrows). After resection a slightly similar heterogeneous contrast distribution can be observed (Fig 5(C-D)) where only some areas in the upper regions of both nodes contain PA signal (blue, pink and green arrows). Histological comparison using Vimentin (Fig. 5(E-F)) shows extensive metastatic involvement inside both nodes (brown). More or less unaffected areas (light blue) can also be noted (blue arrow) which could explain the various PA signal still present within the node, however direct correlation between PA and histology remains challenging. In addition, the presence of an afferent vessel (pink arrow) might offer an explanation for the PA signal generated in the right half of the node. PA imaging of the control nodes (Fig. 5(G-H)) does also show an absence of signal in the nodal volume which deviates from earlier observations. Vessel like structures surrounding the nodal volume (orange arrows) can also be noted. *In corpore* results are contradictory to the *ex vivo* results (Fig. 5(I-J)) which show an homogenous distribution throughout the nodes. Histological comparison verifies that no metastatic cells are present inside the nodes and dimensions are comparable to those measured inside the PA images. The presence of a vessel-like structure exiting the first control node (Fig 5I, red arrow) seems to correspond to the presence of the nodal hilus at this location on histology (Fig 5K, red arrow).

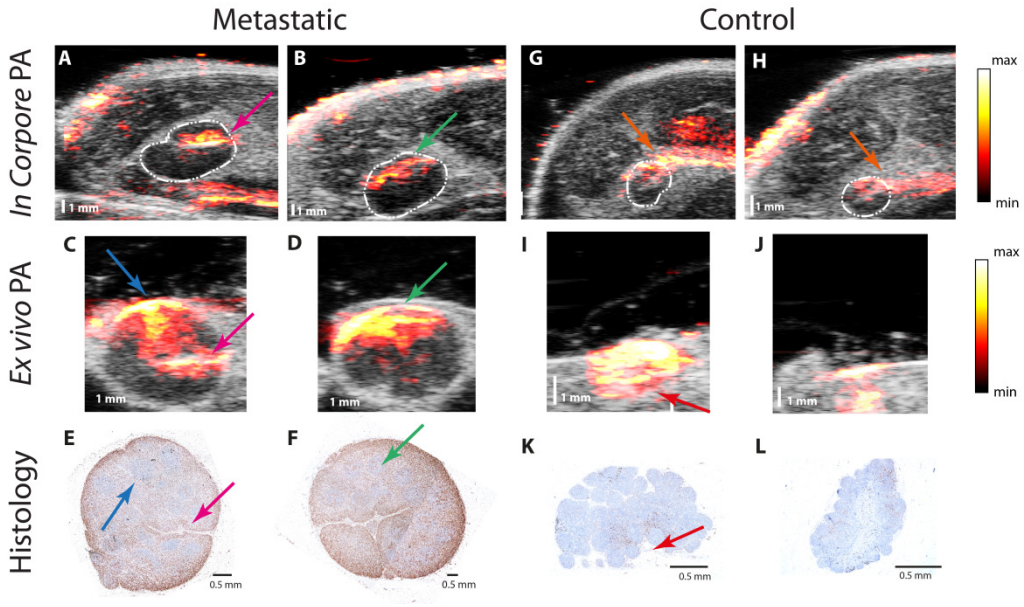

Fig. 5. *In corpore* and *ex vivo* PA lymph nodes scans of two metastatic and two control nodes acquired using the VEVOLAZR system. All images are composed of an overlay of ultrasound (gray) and photoacoustic (red-yellow) scans. Nodal volumes are outlined in white. Metastatic nodes show an irregular contrast distribution both within the animal (A-B) as after resection (C-D) displaying large areas which lack PA signal. Some PA signal can be detected at different locations throughout the nodal volume (pink, blue and green arrows). These areas show some correlation with a decreased presence of metastatic cells (brown) in immunohistochemical Vimentin stained slices (E-F, blue and green arrows). In addition, the presence of a blood vessel (pink arrow) correlates with the PA signal on the right side of the first node. Control nodes show almost no PA signal within the animal (G-H) and are surrounded by vessel like structures, generating large PA responses (orange arrows). After resection the control nodes show up completely enhanced (I-J) and a small vessel-like structure seems to run near the first lymph node (red arrow). Histology reveals no metastatic cells (no brown staining) (K,L) and depicts several small vessels exiting the lower side of the first node (red arrow).

6.4 Discussion

Based on the obtained results we can conclude that there is significant difference between the PA response of resected benign and metastatic lymph nodes after carbon nanoparticle injection. Regular and homogenous intensity bands in the peripheral zone of both control and reactive nodes are replaced by inhomogeneous distributions with larger low contrast areas. These changes are comparable to those seen after injection of SPIO nanoparticles and correspond to the theory of macrophage replacement by metastatic cell involvement, as for example described by Kimura *et al* (28). The resemblance in PA absorption maps between control and immune-reactive nodes demonstrates that any immune reactive response to the tumor may not be of influence on the overall PA response. Based on these observations, the effectiveness of the technique might be independent from the state of the lymphatic system which is beneficial for clinical applicability.

Imaging results obtained with the VEVOLAZR system show that PA information can still be obtained at a depth of 1 cm while maintaining an unimpaired skin barrier . However, a distinction between benign and metastatic nodes proves to be challenging. The absence of PA signal in the volume of the benign nodes could be explained by the lower fluence at these depths or the influence of other anatomical structures which overpower the relatively weak PA signal of the carbon nanoparticles. Especially nearby vessels (Fig 5 (G-H), orange arrows) containing significant amounts of hemoglobin could contribute to this effect. In order to remove the PA signal associated with hemoglobin, PA spectroscopy could be implemented in future setups. The characteristic absorption spectrum of hemoglobin in the near-infrared might be relatively easy distinguished from the flat spectrum of carbon particles which could lead to better non-invasive staging results. The additional PA scans of the excised lymph nodes show that a distinction between benign and metastastic nodes can again be made once the lymph nodes are resected.

Whether metastatic nodes also retain lower amounts of carbon nanoparticles compared to control or reactive nodes remains hard to verify because exact carbon concentrations could not be measured. The PA contrast analysis seems to indicate that this difference is relatively minor as average signal strength is comparable between groups, however because a quantitative analysis technique is unavailable we are unable to validate this. The average mean pixel intensity within the nodes after carbon injection however proves to be higher compared to that detected in the SPIO enhanced nodes of our earlier study (approximately 200 to70) (15). This observations indicates that carbon nanoparticles dispersions might be more potent PA contrast agents than SPIO's with respect to PA signal generation. This aspect might be especially beneficial once a distinction between benign and metastatic nodes has to be produced while low particle concentrations are present within the nodes. Moreover, none of the animals exhibited side-effects of the carbon injections which strengthens its claim for safe subcutaneous use. On the basis of these observations, carbon particles might be preferred above SPIO nanoparticles to enable fast intra-operative lymphatic staging.

In this study we applied two different PA imaging systems. One containing a tomographic approach and one based on a linear geometry. Utilization of a tomographic or linear geometry entails different advantages and disadvantages from a clinical perspective. The clinical benefits of a linear geometry, as applied within the VEVOLAZR system, are more numerous with respect to *in vivo* intra-operative appliances. A B-mode acquisition time of less than 1 second and a hand-held design facilitates rapid nodal scanning within a confined space, as is the case during many nodal resection procedures, and might therefore be especially suited to stage lymph nodes *in vivo*. One might therefore expect that such an approach could be especially applicable during a regional lymphadenectomy in order to verify which lymph nodes contain metastases. Thus providing an option to selectively

remove the involved nodes while maintaining the viability of the benign ones. A tomographic approach on the other hand could offer more advantages once an analytical method is designed for *ex vivo* resected lymph nodes, providing a higher resolution and the possibility of multiple angle illumination. From a clinical perspective, this approach might therefore be more suited to rapidly stage sentinel lymph nodes, allowing for additional nodal resection during the same operational procedure once metastases are located. The results show that nodal staging using carbon nanoparticles might be realized using both geometries although intra-operative use should verify whether a linear geometry is able to accurately stage lymph nodes once inserted through a surgical aperture/inlet inside a hemoglobin-rich environment.

6.5 Conclusions

Overall we conclude that carbon nanoparticles might be a suitable alternative to SPIOs for PA intra-operative nodal staging. Differences between benign and metastatic nodes are visualized by inhomogeneities in the PA contrast distributions especially in the pheripheral zone. Both reactive as normal nodes show a homogeneous contrast distribution which indicates that both can be correctly staged using PA imaging. The distinction between benign and metastatic nodes is most clear in an *ex vivo* setting although additional research should verify whether *in vivo* staging might be possible for superficial lymph nodes. We recognize that carbon nanoparticles dispersion should be fabricated according to good manufacturing practice and tested for subcutaneous applicability before introducing them into a clinical setting, but state that no health or safety restrictions of the particle stand in the way of doing this within a reasonable time-span.

6.6 References

1. Runge VM, Ai T, Hao D, Hu X. The developmental history of the gadolinium chelates as intravenous contrast media for magnetic resonance. Invest Radiol 2011; 46(12):807-816.
2. Swensen SJ, Viggiano RW, Midthun DE, Muller NL, Sherrick A, Yamashita K, Naidich DP, Patz EF, Hartman TE, Muhm JR, Weaver AL. Lung nodule enhancement at CT: multicenter study. Radiology 2000; 214(1):73-80.
3. Yarbro JW, Page DL, Fielding LP, Partridge EE, Murphy GP. American Joint Committee on Cancer prognostic factors consensus conference. Cancer 1999; 86(11):2436-2446.
4. Weissleder R, Elizondo G, Wittenberg J, Lee AS, Josephson L, Brady TJ. Ultrasmall superparamagnetic iron oxide: an intravenous contrast agent for assessing lymph nodes with MR imaging. Radiology 1990; 175(2):494-498.
5. Weissleder R, Elizondo G, Wittenberg J, Rabito CA, Bengele HH, Josephson L. Ultrasmall superparamagnetic iron oxide: characterization of a new class of contrast agents for MR imaging. Radiology 1990; 175(2):489-493.
6. Pieterman RM, van Putten JW, Meuzelaar JJ, Mooyaart EL, Vaalburg W, Koeter GH, Fidler V, Pruim J, Groen HJ. Preoperative staging of non-small-cell lung cancer with positron-emission tomography. N Engl J Med 2000; 343(4):254-261.

7. Lardinois D, Weder W, Hany TF, Kamel EM, Korom S, Seifert B, von Schulthess GK, Steinert HC. Staging of non-small-cell lung cancer with integrated positron-emission tomography and computed tomography. N Engl J Med 2003; 348(25):2500-2507.
8. Oyama N, Akino H, Kanamaru H, Suzuki Y, Muramoto S, Yonekura Y, Sadato N, Yamamoto K, Okada K. 11C-acetate PET imaging of prostate cancer. J Nucl Med 2002; 43(2):181-186.
9. Macapinlac HA, Humm JL, Akhurst T, Osman I, Pentlow K, Shangde C, Yeung HW, Squire O, Finn RD, Scher HI, Larson SM. Differential Metabolism and Pharmacokinetics of L-[1-(11)C]-Methionine and 2-[(18)F] Fluoro-2-deoxy-D-glucose (FDG) in Androgen Independent Prostate Cancer. Clin Positron Imaging 1999; 2(3):173-181.
10. Anzai Y, Piccoli CW, Outwater EK, Stanford W, Bluemke DA, Nurenberg P, Saini S, Maravilla KR, Feldman DE, Schmiedl UP, Brunberg JA, Francis IR, Harms SE, Som PM, Tempany CM. Evaluation of neck and body metastases to nodes with ferumoxtran 10-enhanced MR imaging: phase III safety and efficacy study. Radiology 2003; 228(3):777-788.
11. Bellin MF, Roy C, Kinkel K, Thoumas D, Zaim S, Vanel D, Tuchmann C, Richard F, Jacqmin D, Delcourt A, Challier E, Lebret T, Cluzel P. Lymph node metastases: safety and effectiveness of MR imaging with ultrasmall superparamagnetic iron oxide particles--initial clinical experience. Radiology 1998; 207(3):799-808.
12. Will O, Purkayastha S, Chan C, Athanasiou T, Darzi AW, Gedroyc W, Tekkis PP. Diagnostic precision of nanoparticle-enhanced MRI for lymph-node metastases: a meta-analysis. Lancet Oncol 2006; 7(1):52-60.
13. Motomura K, Ishitobi M, Komoike Y, Koyama H, Noguchi A, Sumino H, Kumatani Y, Inaji H, Horinouchi T, Nakanishi K. SPIO-enhanced magnetic resonance imaging for the detection of metastases in sentinel nodes localized by computed tomography lymphography in patients with breast cancer. Ann Surg Oncol 2011; 18(12):3422-3429.
14. Weissleder R, Elizondo G, Josephson L, Compton CC, Fretz CJ, Stark DD, Ferrucci JT. Experimental lymph node metastases: enhanced detection with MR lymphography. Radiology 1989; 171(3):835-839.
15. Grootendorst DJ, Jose J, Fratila RM, Visscher M, Velders AH, Ten Haken B, Van Leeuwen TG, Steenbergen W, Manohar S, Ruers TJ. Evaluation of superparamagnetic iron oxide nanoparticles (Endorem(R)) as a photoacoustic contrast agent for intra-operative nodal staging. Contrast Media Mol Imaging 2013; 8(1):83-91.
16. Beard P. Biomedical photoacoustic imaging. Interface Focus 2011; 1(4):602-631.
17. Razansky D, Deliolanis NC, Vinegoni C, Ntziachristos V. Deep tissue optical and optoacoustic molecular imaging technologies for pre-clinical research and drug discovery. Curr Pharm Biotechnol 2012; 13(4):504-522.
18. Wang LV, Hu S. Photoacoustic tomography: in vivo imaging from organelles to organs. Science 2012; 335(6075):1458-1462.
19. Kam NW, O'Connell M, Wisdom JA, Dai H. Carbon nanotubes as multifunctional biological transporters and near-infrared agents for selective cancer cell destruction. Proc Natl Acad Sci U S A 2005; 102(33):11600-11605.

20. O'Connell MJ, Bachilo SM, Huffman CB, Moore VC, Strano MS, Haroz EH, Rialon KL, Boul PJ, Noon WH, Kittrell C, Ma J, Hauge RH, Weisman RB, Smalley RE. Band gap fluorescence from individual single-walled carbon nanotubes. Science 2002; 297(5581):593-596.
21. Aboosy N, Mulder CJ, Berends FJ, Meijer JW, Sorge AA. Endoscopic tattoo of the colon might be standardized to locate tumors intraoperatively. Rom J Gastroenterol 2005; 14(3):245-248.
22. Shatz BA, Weinstock LB, Swanson PE, Thyssen EP. Long-term safety of India ink tattoos in the colon. Gastrointest Endosc 1997; 45(2):153-156.
23. Kumashiro R, Sano C, Sakai T, Ugaeri H, Madokoro S, Yamazaki S, Inutsuka S, Takahashi T. Radical lymphadenectomy for rectal cancer facilitated by a carbon particle infusion lymphangiography. Surg Today 1992; 22(6):512-516.
24. Yokota T, Saito T, Narushima Y, Iwamoto K, Iizuka M, Hagiwara A, Sawai K, Kikuchi S, Kunii Y, Yamauchi H. Lymph-node staining with activated carbon CH40: a new method for axillary lymph-node dissection in breast cancer. Can J Surg 2000; 43(3):191-196.
25. Okamoto K, Sawai K, Minato H, Yada H, Shirasu M, Sakakura C, Otsuji E, Kitamura K, Taniguchi H, Hagiwara A, Yamaguchi T, Takahashi T. Number and anatomical extent of lymph node metastases in gastric cancer: analysis using intra-lymph node injection of activated carbon particles (CH40). Jpn J Clin Oncol 1999; 29(2):74-77.
26. Vassallo P, Matei C, Heston WD, McLachlan SJ, Koutcher JA, Castellino RA. Characterization of reactive versus tumor-bearing lymph nodes with interstitial magnetic resonance lymphography in an animal model. Invest Radiol 1995; 30(12):706-711.
27. Jose J, Willemink RG, Resink S, Piras D, van Hespen JC, Slump CH, Steenbergen W, van Leeuwen TG, Manohar S. Passive element enriched photoacoustic computed tomography (PER PACT) for simultaneous imaging of acoustic propagation properties and light absorption. Opt Express 2011; 19(3):2093-2104.
28. Kimura K, Tanigawa N, Matsuki M, Nohara T, Iwamoto M, Sumiyoshi K, Tanaka S, Takahashi Y, Narumi Y. High-resolution MR lymphography using ultrasmall superparamagnetic iron oxide (USPIO) in the evaluation of axillary lymph nodes in patients with early stage breast cancer: preliminary results. Breast Cancer 2010; 17(4):241-246.

CHAPTER 7

COMPARISON BETWEEN I*N VIVO, IN TOTO* AND *EX VIVO* PHOTOACOUSTIC DETECTION OF NODAL METASTASES USING A NEW CLINICAL GRADE SPIO DISPERSION (SIENNA+) *

To determine prognosis and treatment, accurate nodal staging is essential in many tumor types. After injection of clinical grade superparamagnetic iron oxide (SPIO) nanoparticles, it has been shown that metastatic lymph nodes can be distinguished from benign specimens using photoacoustic (PA) imaging, once these nodes have been excised. *In vivo* non-invasive PA imaging of lymph nodes before resection could further expand the scope of the technique and would allow for pre-operative nodal staging. In order to look into the feasibility of such an approach six Mat-lylu inoculated Copenhagen rats were photo acoustically imaged after injection of a new Class IIa medical device SPIO magnetic tracer (Sienna+). Lymph nodes were imaged *in vivo*, *in toto* (after euthanization) and *ex vivo*. Results demonstrate that a non-invasive distinction between metastatic and benign nodes is impeded by the low amount of PA contrast generated by the SPIO particles compared to that of endogeneous absorbers. However, after excision the PA contrast of Sienna+ is able to facilitate a distinction between both groups. These results are verified by MRI, immunohistochemistry and photographs of the sectioned nodes. This comparison between i*n vivo, in toto* and *ex vivo* PA imaging of lymph nodes after SPIO injection demonstrates that the clinical potential of combined PA/SPIO staging should initially be verified in an *ex vivo* setting.

* This chapter will be communicated as: D. J. Grootendorst, R. M. Fratila, M. Visscher, G.C. Langhout, B. Ten Haken, R.J.A. Van Wezel, S. Rottenberg, W. Steenbergen, S. Manohar, T. J. M. Ruers, "Comparison between i*n vivo, in toto* and *ex vivo* photoacoustic detection of nodal metastases using a new clinical grade SPIO dispersion (Sienna+)" to the journal of Lasers in Surgery and Medicine

7.1 Introduction

The detection of lymphatic metastases is related to a worse prognosis in various types of cancer. For melanoma, the 5 year survival rate decreases significantly if nodal involvement is verified (1) while survival in breast cancer patients declines with the number of metastatic deposits detected in the lymphatic system (2). To accurately chart nodal involvement, pre-operative nodal staging has been attempted for most conventional medical imaging techniques with diverging amounts of success. Initially, characteristics as size, shape and several other anatomical markers were utilized to give an indication of probability of metastatic presence in the lymph nodes (3-5). However it was revealed that 10-20% of normal-sized nodes contained tumor deposits and 30% of enlarged nodes only show inflammatory hyperplasia (6,7), making anatomical markers less accurate for nodal staging in many malignancies. In colorectal cancer cases, for example, 90% of the nodal metastases occur in nodes smaller than 1 cm (7,8). These findings initiated a search for a more physiological approach to indentify metastases and resulted in 1989 with the first report on the potential of superparamagnetic iron oxide (SPIO) particles to enhance MR lymphoscintigraphy (9).

Since then, a lot of progress has been made with respect to the clinical evaluation and introduction of iron oxide based nodal contrast dispersions. Not only have the particle components been found safe and effective (10) , but multiple clinical trials have proved that nodal metastases from head and neck, breast, prostate and pelvis can be distinguished with a larger sensitivity and specificity in comparison with unenhanced MRI's (11). Recently a new SPIO magnetic tracer named Sienna+® (EndoMagnetics, Cambridge, United Kingdom), has received CE marking approval as a Class IIa medical device in Europe for use as a sentinel lymph node (SLN) tracer in combination with a magnetic detection system called SentiMag® (12). At the moment, the accuracy of the technique with respect to SLN detection is being evaluated in multiple clinical centers around Europe, preceding its introduction into regular patient care. A SPIO based dispersion Combidex/Resovist® was previously approved for MRI contrast imaging of the liver, but has since been withdrawn from the European market and replaced with Gadolinium based agents. However, because Combidex/Resovist® has been used as a nodal staging agent in a recent clinical study (13) it might also be applicable in the field of lymph node assessment. The magnetic tracer Sienna+ also contains iron oxide nanoparticles and might therefore be useful for the enhancement of nodal metastases in MRI, although the dispersion has not been tested for this purpose. If such an application might prove feasible, clearance from the EMA for this additional application of Sienna+ could be acquired relatively fast, because health and safety issues have already been assessed in earlier approval procedures.

The additional benefit of SPIO dispersions might however not only be exploited by magnetic resonance techniques but also by different optical detection modalities. The optical properties of SPIO nanoparticles, especially the relatively large optical cross-

sections of their iron oxide cores (14), enables them to absorb significant amounts of optical energy, diminishing optical transmission. One of the techniques for mapping the absorption is photoacoustics (PA), a hybrid imaging modality uncoupling signal generation and detection (15,16). Absorption of optical energy following short pulsed optical illumination enables ultrasound wave generation due to thermoelastic expansion. Detection and reconstruction of these ultrasound signals allows for the mapping of chromophores several centimeters deep within biological tissue (17). The fact that, ultrasonic scattering is several magnitudes smaller than optical scattering ensures retention of spatial resolution at larger imaging depths. These characteristics are already being exploited for breast cancer detection (18-20), melanoma imaging (21,22) and tumor visualization in small animals (23,24).

In order to verify whether the applicability of SPIO dispersions could be expanded into the photoacoustic domain, our group has experimented with the clinical agent Endorem® (Guerbet, Villepinte, France) in small animals. Initially we verified whether the distribution of SPIO particles could be mapped in the resected lymph nodes of healthy animals and found out this could be done at amounts as low as approximately 11 µg (25). We then applied this knowledge in a metastatic animal model and visualized differences between metastatic and benign lymph nodes. Differences could be detected in the homogeneity of the SPIO distribution and the amount of PA signal generated within the nodes. Although this demonstrated the nodal staging potential of SPIO enhanced PA imaging for a possible *ex vivo* intra-operative application, it remained to be verified whether a non-invasive *in vivo* visualization could be performed. *In vivo* mapping of SPIO nodal deposits could enable pre-operative staging of superficial nodes or facilitate the staging of deeply embedded nodes during a surgical resection (lymphadenectomy).

In this work we evaluate whether the newly developed SPIO magnetic tracer Sienna+ shows a similar performance with respect to *ex vivo* metastases detection and verify if this approach also allows for lymph nodes to be staged non-invasively, *in vivo.* To this end, we use a hand-held, PA imaging system capable of acquiring real-time hybrid ultrasound and photoacoustic images. Imaging results are compared to high field MR and (immuno)histochemistry. In order to find out what the influence of blood flow and motion is on the accuracy of distinction between metastatic and benign nodes, experiments were performed *in vivo*, *in toto* (in euthanized animals) and on resected lymph nodes (*ex vivo*). Eventually, this information could help in the development of a non-invasive nodal screening method which could be applied both pre- and intra-operative.

7.2 Materials and Methods

7.2.1 Research protocol

To study the possibility of non-invasive photoacoustic lymph node staging using Sienna+, six female Copenhagen rats, weighing 150-200 g were subcutaneously injected with R3327 MAT-lylu cells in their left hindpaw. Mat-lylu cells originate from a highly metastatic prostate adenocarcinoma inducing metastases to the lymph nodes and lungs. Cells were cultured in RPMI-1640 medium, supplemented with 10% fetal calf serum and 100 ml penicillin/streptomycin. All experiments were set up according to the Dutch animal welfare guidelines and approved by the Animal Care Committee of the University Medical Center Utrecht.

At day one, $1x10^6$ MAT-lylu cells were dispersed in 0.1 ml of medium and inoculated subcutaneously in the left paw of each animal. After 8 days of tumor inoculation 0.1 ml of Sienna+ (iron concentration: 28 mg/ml) was subcutaneously injected in both hind paws and 24 hours later, photoacoustic scans of both popliteal areas (around the knee joint) were

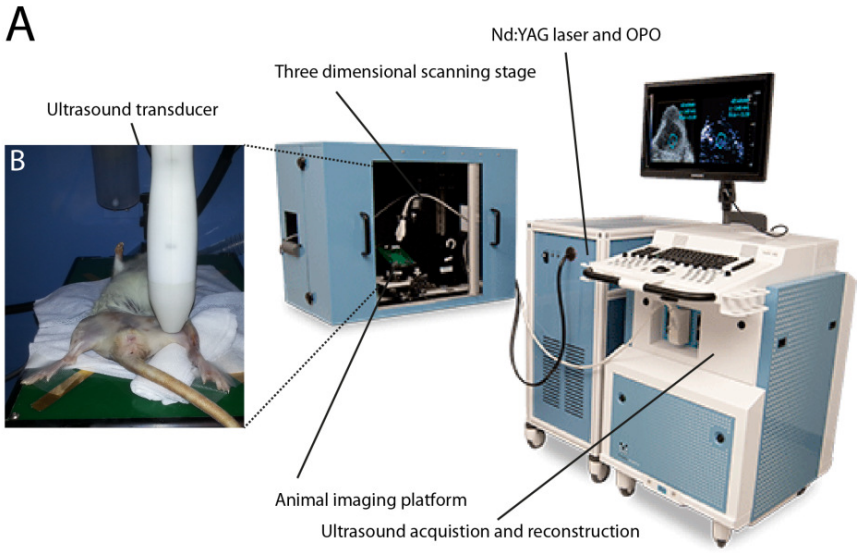

Fig. 1. A. Overview of the VEVOLAZR© PA imaging system consisting of a sealed imaging box and a commercial ultrasound system coupled to a Nd:YAG-laser. B. Inside the scanning box, the animal is mounted on top of an adjustable scanning platform and the transducer is placed into contact with of the skin of the popliteal area.

made in order to image the popliteal node. Sienna+ differs from, for example Endorem®, on the basis of its coating (carboxydextran vs dextran) and hydrodynamic particle size (75 vs 80-150 nm (estimated sizes)). However these differences should have limited influence on its biological use. Inoculation of tumor cells in the left hindpaw resulted in nodal metastases in the left popliteal node while the right side remained unaffected and served as control. PA imaging of both popliteal areas of each animal therefore resulted in an intra-individual comparison of metastatic and benign nodes. Animals were divided into two groups of three animals of which the first underwent PA imaging while alive (*in vivo* group) and the second after euthanization (*in toto* group). *In vivo* animals were anesthetized during all image sequences to minimize motion artefacts and were monitored for body temperature and heart rate. The lower part of the animals was shaven to ensure proper contact between transducer and skin. All animals were placed on top of an adjustable platform (Fig. 1B) and an acoustic connection between animal and transducer was created with warm ultrasound gel. After imaging, both popliteal nodes were resected (left and right) and placed into a waterfilled tank where they were fixed with ultrasound gel to prevent floating. Additional PA scans of all resected lymph nodes were then acquired in order to verify the PA distribution after resection (*ex vivo*) and correlate it to the contrast distribution inside the animal. The total experimental protocol resulted in 6 lymph nodes (3 benign and 3 metastatic) to be scanned *in vivo*, 6 lymph nodes (3 benign and 3 metastatic) *in toto* and 12 lymph nodes (6 benign and 6 metastatic) *ex vivo*.

7.2.2 Additional analysis

Next to the hybrid PA imaging, MR imaging of the resected lymph nodes was performed after 4% formaldehyde fixation using a 14 Tesla MR scanner (Bruker, Ettlingen, Germany). Multi-slice-multi-echo (MSME) imaging sequence was used with an echo time of 7.2 ms and a repetition time of 1000 ms, as described in (25). Furthermore, the iron quantities in the nodes were measured using differential magnetometry, a newly developed measurement technique based on detection of the nonlinear response of SPIOs by subtracting magnetic susceptibilities at different offset fields. The linear susceptibility of tissue (background) does not show modulation for these fields, which provides an unambiguous detection of the SPIO tracer. Compensation for volume differences between the nodes was achieved by dividing iron quantities by the volume of the nodes. Nodal volumes were estimated using an ellipsoid formula in which the dimensions of each node were incorporated. Finally, nodes were histologically processed and stained for both H&E and Vimentin. Vimentin, a type III intermediate filament (IF) protein and mesenchymal marker, was chosen because it is specifically suited to stain highly metastatic cells like the MAT-lylu line. In addition, photographs of the paraffin blocks were made to verify SPIO distribution after embedding. In order to maintain a comparable orientation between the different imaging modalities, specific outlines of all samples were marked with colored dye.

7.2.3 Photoacoustic setup

All PA imaging was performed using the VEVOLAZR© photoacoustic setup (Visualsonics, Ontario, Canada) shown in Figure 1. The system is capable of hybrid PA and ultrasound (US) acquisition enabling a real-time overlay of both modalities. Anatomical information about the position of the node at the popliteal area could therefore be easily verified and the location of the PA response could be correlated within the node. The system consists of a Nd:YAG-laser coupled to a optical parametric oscillator, operating at 20 Hz. A 256 element transducer with a central frequency of 20MHz was utilized for ultrasound acquisition. Optical fibers incorporated into the transducer generate a spot size of 24 mm^2 which corresponds to a fluence of about 20 mJ/cm^2. Image acquisition time of the system proved to be 0.2 s for a 2D image (Image dimensions: 20*23 mm) and 74 seconds for a 3D volume scan of 10 mm (Image dimensions: 20*23*10 mm).

7.2.4 Photoacoustic imaging

Of both the thigh areas of the six animals and the corresponding resected lymph nodes, a 3D volume acquisition was made of 20*20*20 mm in order the capture the entire nodal volume. Of these 3D scans a representative image was selected to display the PA distribution characteristics in each animal and resected node. Images were acquired using an excitation wavelength of 720 nm to compare the results with those obtained within our previous Endorem® study (25). In addition, an hyperspectral slice scan was performed, capturing image frames at 2 nm intervals from 700 to 800 nm. Hyperspectral scans were analyzed by loading the data into Matlab and extracting pixels with a similar spectral response using a spectral clustering algorithm. To compensate for fluence differences the data were normalized for the area under the curve. For clustering an agglomerative hierarchical cluster tree algorithm was used including a Haar wavelet decomposition up to the 12^{th} level. The number of final output clusters was varied. The extracted pixels were color coded and the corresponding spectrum was visualized. The algorithm required no pre-analysis input, except the assignment of the analysis area in the ultrasound image. The image acquisition speed of the system resulted in 3D popliteal scans of around 3 minutes and spectral slices of around 2 minutes for each animal.

7.3 Results

PA imaging results of the *in vivo* group are displayed in Figure 2. Two-dimensional ultrasound image slices of both popliteal areas depict the popliteal nodes as hypo-intensive structures (yellow dotted line) surrounded by hyper-intensive fatty areas (red dotted line). All nodes are located approximately 10-15 mm beneath the US detector and 4-7 mm beneath the skin (blue dotted line). Metastatic nodes depicted a significantly larger size compared to the contra-lateral control nodes which facilitated their localization. For the images of the control nodes the location of the node (yellow dotted line) is magnified in order to facilitate visual analysis of the PA distribution within them.

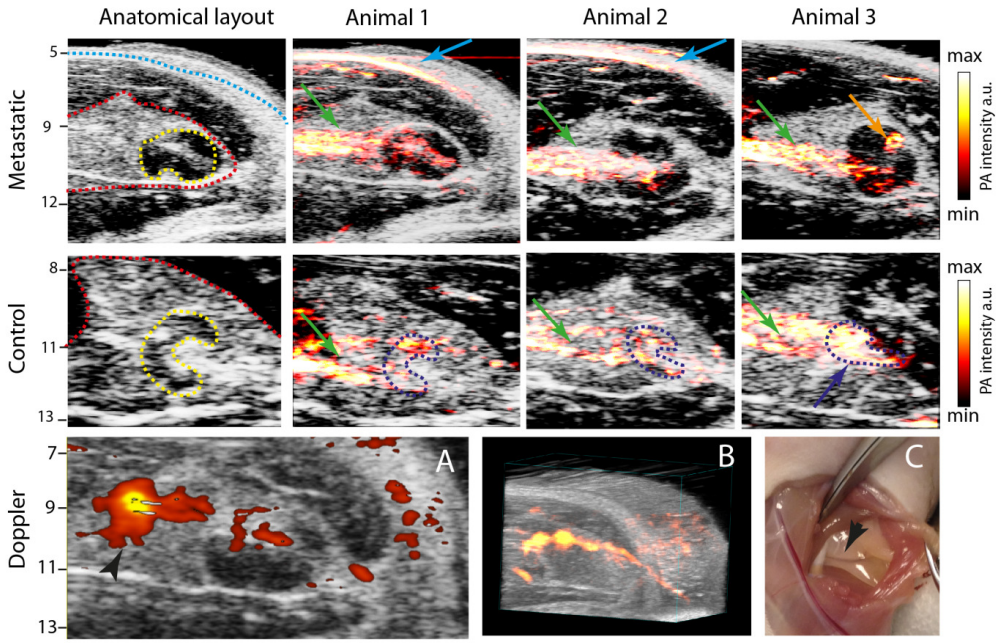

Fig. 2. Top: Hybrid PA and US images of the *in vivo* group. The anatomical layout shows the hypo-intensive lymph node (yellow dotted line) embedded in hyper-intensive fat (red dotted line). Depth in mm from the transducer is displayed on the left. The PA overlays show response from the skin (blue arrow) and a linear structure on the left of the nodal outline (green arrow). Only some PA response can be detected inside the lymph nodes on the metastatic side (orange arrow) while heterogeneous response arise within the volume of the control nodes (blue dotted line). A. Power doppler imaging of the nodal area displays a strong flow at the location of the linear PA structure (black arrow) corresponding with the presence of a blood vessel. B. Three-dimensional reconstruction of the Doppler images shows the layout of the vessel beneath the skin. C. During resection a small vessel can be seen running near the popliteal lymph node (black arrow).

Corresponding PA scans of the popliteal areas show some signal coming from the skin (light blue arrows) and a 1-1.5 mm wide and several mm long highly absorbing structure around 10 mm beneath the detector (green arrows). PA signal generation within the metastatic nodal volume is mostly absent although some can be pinpointed in animal 3 (orange arrow). The control nodes are significantly smaller and to aid visual analysis *in vivo* their outline is indicated with dark blue dotted lines. The control nodes in animal 1 and 2 generate minor PA signals and remain hidden behind the PA response of the absorbing structure running on the left of the nodes (green arrows). The nodal volume of the control node in animal 3 (dark blue arrow) display significantly more PA signal and could be distinguished from the PA response of the surrounding structures. The lack of PA intensity within the control nodes makes it challenging to define the SPIO distribution and impedes a distinction between the metastatic and benign nodes based on their contrast distribution.

High resolution Power Doppler imaging (Fig. 2A-B) shows that the increased PA intensity in the structures pinpointed with the green arrows is caused by the presence of small blood vessels. Most likely a branch of the iliac vessels. Flow can be seen on the left side of the node (Fig. 2A, black arrow) running all the way into the nodal volume. A three-dimensional stack of the Doppler images shows the course of the vessel throughout the imaged volume (Fig. 2B). During nodal resection the vessel could also be seen running inside the extra nodal fat (Fig. 2C, black arrow).

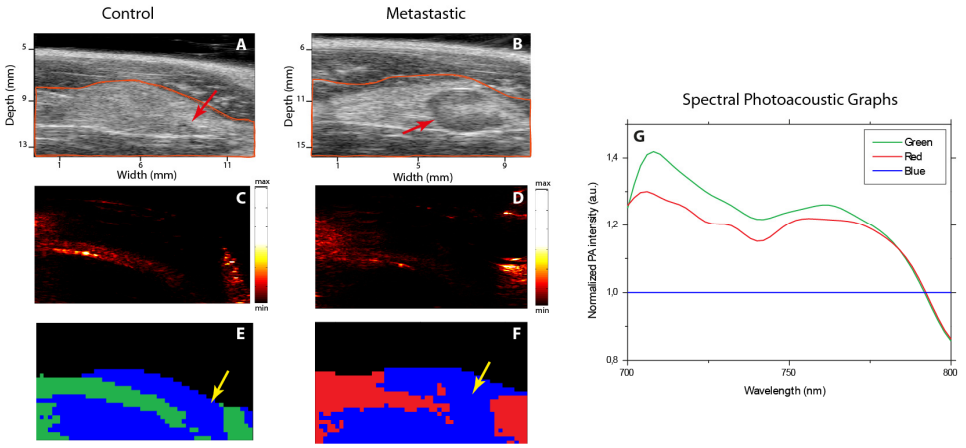

Fig. 3. Hyperspectral analysis of both the control and metastatic popliteal area of animal 1. A-B: Anatomical ultrasound layout if the popliteal zone with both nodes located on the right side (red arrows). The area of spectral analysis is outlined in orange. C-D: Corresponding PA intensity images of both areas. E-F: Spectral clustering maps of both areas after calculation of two final clusters. While the popliteal nodes (yellow arrows) lack spectral information, the absorbing structures in the surrounding tissue show a specific spectral response. G: Spectral graphs of both clustered areas. Both spectra show a small increase around 760 nm corresponding with the presence of hemoglobin.

Hyperspectral PA analysis of both the control and metastatic popliteal regions of the animals (Fig 3A-G) also shows that most of PA intensity is located to the left of the popliteal node corresponding with the suspected location of the blood vessels. The clustermaps obtained after clustering into two final clusters (Fig 3E and F) display an almost uniform spectral response in the area surrounding the node. Almost no PA response is seen at the location of the popliteal node (yellow arrows). Both spectral regions display a fairly similar spectral response (Fig 3G) with a decreasing trend towards higher excitation wavelengths. A small increase can be detected around 760 nm which corresponds with the increased optical absorption of both states of hemoglobin around this wavelength. We note that a larger amount of final clusters results in more spectra to be extracted although these spectra all resemble the spectra in Figure 3G. The results therefore strengthen the claim that this PA response is most likely blood related.

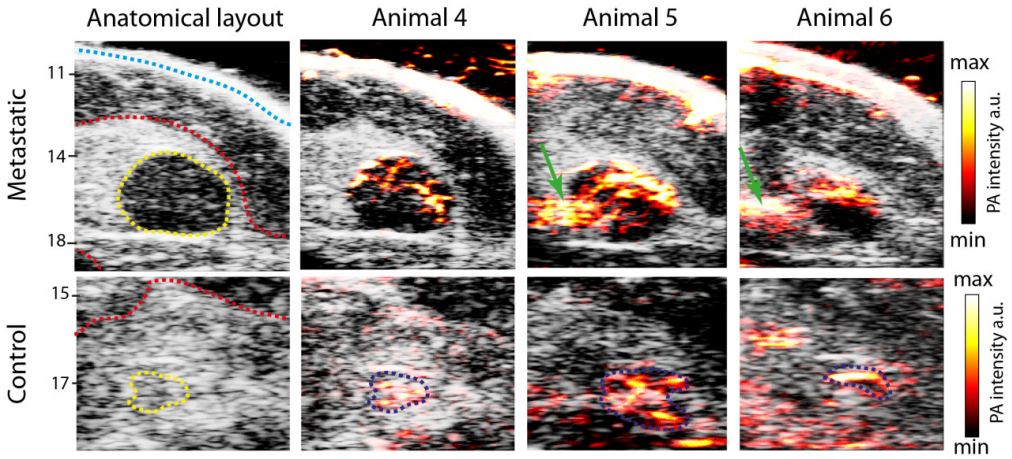

Fig. 4. Hybrid PA and US images of the *in toto* group. The anatomical layout shows the hypo-intensive lymph node (yellow dotted line) embedded in hyper-intensive fat (red dotted line). The depth in mm from the transducer is displayed on the left. The PA overlays show more PA signal coming from within the volumes of the metastatic nodes compared to the *in vivo* situation while the intensities on the left side of the nodes have decreased (green arrows) or cannot be detected. At the locations of the control nodes, more PA signal can be detected although its heterogeneous distribution does not facilitate an more easy differentiation.

Hybrid PA imaging results of the *in toto* group are displayed in Figure 4. Ultrasound shows a similar anatomical layout, with the hypo-intensive nodes (yellow dotted line) surrounded by hyper-intensive fatty areas (red dotted line). The corresponding PA overlay shows absorption by the skin and some areas within the popliteal nodes. Overall more PA response can be detected within the nodal volumes of the *in toto* group than the *in vivo* group. PA signals related to the nearby blood vessel seem to be less prominent and could only be detected on the metastatic side of animal 5 and 6 (green arrows). Due to the small size of the control nodes their location could not always be pinpointed with ultrasound, however after PA overlay small regions of PA contrast were seen which corresponded with the locations of the nodes (dark blue dotted lines). PA distribution inside the control nodes did not prove to be uniform which made it difficult to distinguish them from the metastastic nodes on basis of their contrast distribution.

PA imaging, MR imaging and photographs of the sectioned nodes (Fig 5 and 6) show that a distinction between the metastatic and control nodes based on the PA contrast distribution can be made after resection (*ex vivo*). All control nodes display a homogeneous contrast distribution within their volume (Fig. 5, upper row) which corresponds with the overall SPIO related blackening inside the MR images (Fig. 5, middle row). In addition, photographs of the paraffin blocks (Fig 5. bottom row) also show a homogenous SPIO distribution which confirms these imaging results. All the metastatic nodes on the other hand, lack PA response at specific locations within their outline (Fig. 6, upper row) corresponding with an inhomogeneous SPIO distribution. Similar locations, lacking SPIO related blackening, can be seen in the MR images (Fig. 6, middle row) and their locations (red arrows) grossly match those detected in the PA images. Corresponding photographs of the paraffin blocks also show that several locations within the nodal periphery lack SPIO deposition (green arrows) and that the SPIO deposition layout resemblances that detected by hybrid PA/US and MR imaging.

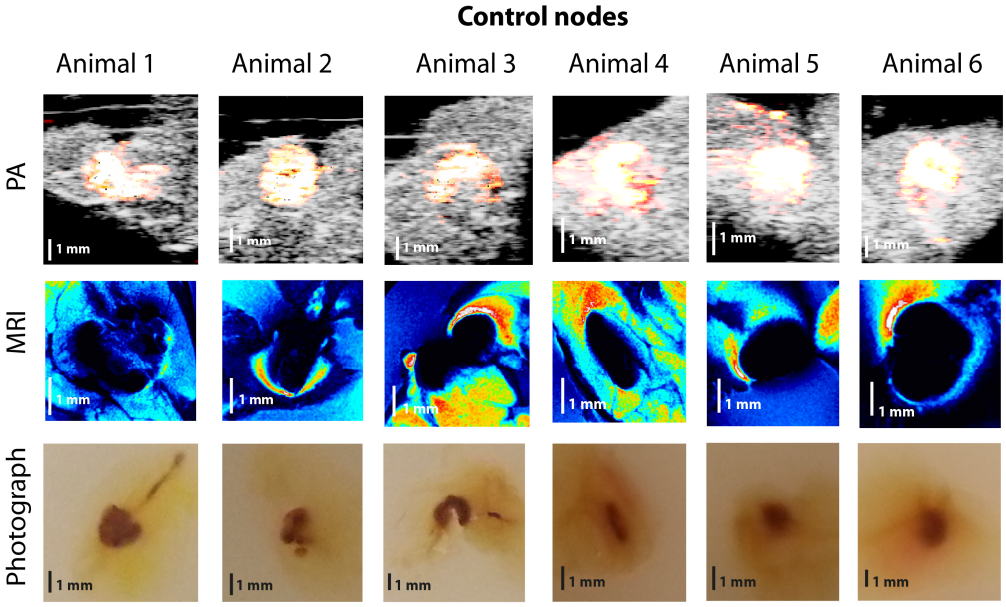

Fig. 5. Hybrid PA/US and MR images of the resected (*ex vivo*) control nodes and the photographs of the corresponding paraffin sections. It can be noted that the entire volume of the nodes displays a PA response which correlates with the inclusion of SPIO particles throughout the nodal volume. SPIO related blackening can also be noted in MR images covering the entire nodal volume. In addition, the photographs of paraffin sections show that the SPIOs are homogeneously distributed throughout the sections.

These locations of signal absence grossly correlate with the presence of metastatic deposits in these regions as displayed in Figure 7. The Vimentin staining (brown) for animal 1 shows that MAT-lylu cells are prominently located in the lower part of the node (black triangles) which corresponds to the area of signal absence in the PA images. Higher H&E magnifications confirm the deposition of MAT-lylu cells and the photograph of the paraffin sections shows an absence of SPIOs at the same location. The control node mostly stains negative for Vimentin and H&E magnifications show that the brownish discoloring in some places is caused by the extensive presence of SPIO depositions (black triangles) instead of metastatic cell involvement.

Quantitative iron measurements show iron concentrations fluctuate between 6 µg and 50 µg (Table 1). Individual variation between the different nodes is relatively large, although there is an average difference of ± 10 µg between the benign and metastatic group indicating a lower uptake for the metastatic group. Calculation of the iron concentration by dividing the iron amounts by the volume of each node results in an even larger average difference (9.5 vs 0.7) of approximately a factor 10. These results suggest that the overall SPIO concentration inside metastatic lymph nodes could be lower compared to benign nodes.

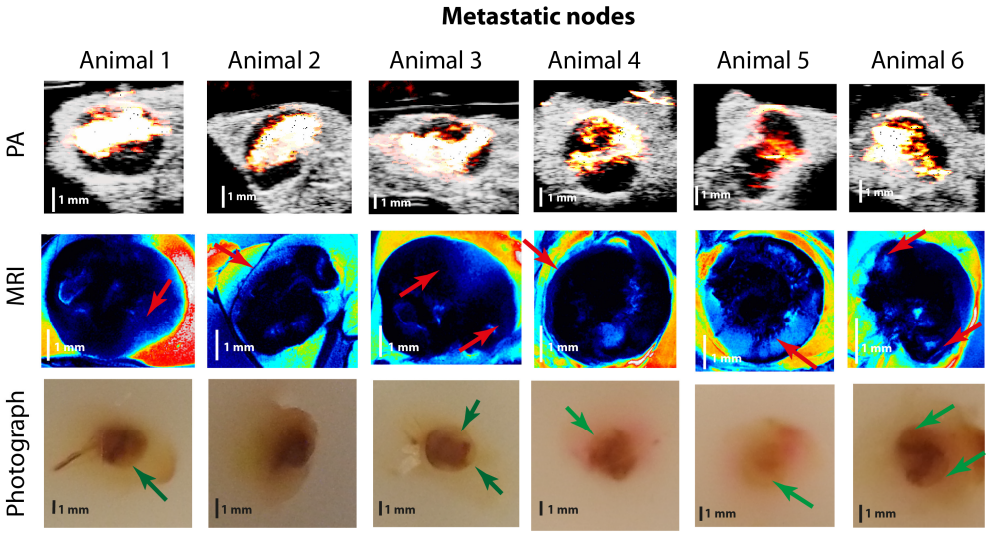

Fig. 6. Hybrid PA/US and MR images of the resected (*ex vivo*) metastatic nodes and the photographs of the corresponding paraffin sections. It can be noted that the PA images of all nodes show areas which do not generate PA signals most probably indicating a lack of SPIO nanoparticles at these locations. Areas without SPIO related blackening can also be noted in MR images (red arrows) and their locations show some correspondence with the signal-poor locations in the PA images. In addition, the photographs of paraffin sections show that the SPIOs are not homogeneously distributed throughout the volume of the metastatic nodes and that areas lacking brown discoloring (green arrows) grossly correspond with the areas identified by both MRI and PA.

Table 1. Measured iron quantities and concentrations within the resected lymph nodes

Animal Number	Control Iron quantity (µg)	Metastatic Iron quantity (µg)	Control Iron concentration (µg/mm^3)	Metastatic Iron concentration (µg/mm^3)
In vivo				
1	36.2 (± 0.3)	29.8 (± 0.3)	5.0 (± 0.5)	0.9 (± 0.1)
2	24.3 (± 0.2)	35.4 (± 0.2)	8.1 (± 0.5)	1.1 (± 0.1)
3	49.7 (±0.3)	22.6 (± 0.2)	21.6 (± 0.7)	0.9 (± 0.1)
In toto				
1	24.8 (± 0.2)	23.6 (± 0.2)	7.3 (± 0.5)	0.6 (± 0.1)
2	27.1 (± 0.2)	5.8 (± 0.2)	7.8 (± 0.5)	0.1 (± 0.1)
3	27.2 (± 0.2)	9.6 (± 0.1)	7.4 (± 0.5)	0.4 (± 0.1)
Average	31.5	21.1	9.5	0.7

7.4 Discussion and conclusions

Comparison between hybrid photoacoustic imaging of metastatic and benign lymph nodes *in vivo*, *in toto* and *ex vivo* shows that there are significant differences in distinctive power between the three approaches. The results show that *in vivo* PA imaging of the popliteal region is possible and absorbing structures can be visualized non-invasively at a depth of around 1 cm. However, the distinctive capabilities of the *in vivo* approach are limited and an indication of metastatic involvement could only be produced on the basis of nodal size. To our understanding this is mostly caused by the limited optical absorption of the SPIO nanoparticle deposits compared to endogenous absorbers like hemoglobin and melanin. The optical absorption of vessels running close to the node therefore transcend the PA response of the deposits within the nodal volume, disabling the visualization of the SPIO distribution and impeding an accurate distinction. In the future, these effects could possibly be limited by expanding the applicability of PA spectroscopy. The distinctive absorption spectrum of hemoglobin could for example enable the removal of hemoglobin related PA signals once it could be identified after multiple wavelength illumination. Residual PA intensity could then be increased to enable a clearer visualization of the SPIO deposition *in vivo*.

The results show that the PA intensity of the surrounding vasculature is less prominent once blood flow and oxygenation are stopped and more PA intensity can be detected within the nodal volume of both benign and metastatic nodes. However, a clear distinction in PA distribution between both groups still cannot be visualized, mainly due to the heterogeneous signal distribution present within the control nodes. It has to be noticed that the high frequency 20 Mhz transducer favors the visualization of sub-millimeter structures which might be a drawback for detecting lower ultrasound frequencies produced by larger structures like lymph nodes. The availability of a range of transducers might therefore facilitate *in vivo* staging using SPIO nanoparticles.

Recently, Xi *et al* used antigen coupled SPIO nanoparticles to visualize breast tumors inside an animal model (26). They verified that antigen coupled SPIOs are able to achieve a

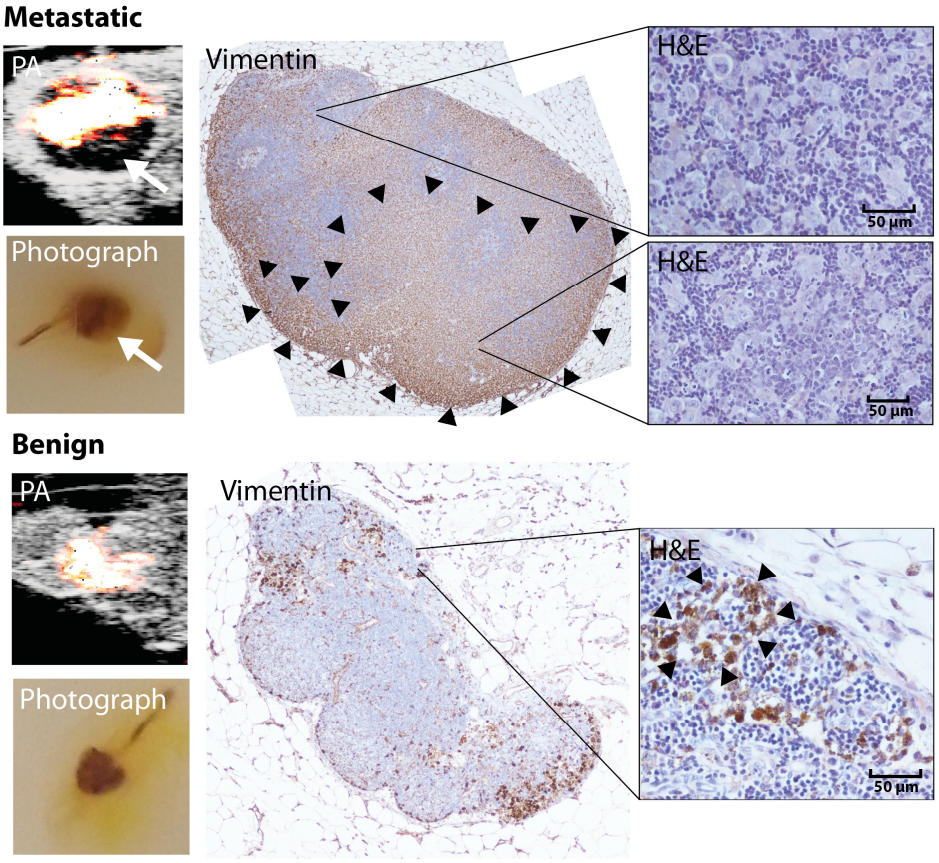

Fig. 7. Hybrid PA imaging, paraffin section and (immuno)histochemical staining of the metastatic and benign node of animal 1. Metastatic: Absence of PA intensity can be seen in the upper and especially lower parts of the node (white arrow). Photographs of the paraffin section also show an absence of discoloring at this location (white arrow) corresponding with a lack of SPIO particles. Vimentin staining shows prominent metastatic involvement especially in the lower part of the node (black triangles). Magnified H&E stainings clearly show the large poorly differentiated carcinoma cells embedded between the different sorts of lymphocytes throughout the nodal volume. Benign: PA intensity is present throughout the nodal volume which corresponds with the SPIO deposition in the photograph. Vimentin staining shows the absence of metastatic cells. Brown discoloring is mostly caused by the presence of SPIO deposits throughout the nodal section (black triangles).

PA contrast which is three times higher compared to uncoupled SPIOs which suggests that targeting of SPIO particles might also be a useful way to increase the particle concentration inside the lymph nodes. Such an approach might therefore also facilitate non-invasive staging.

In order to validate the *in vivo* intra-operative application of the technique, we recognize that PA nodal staging could also have been verified after skin incision, to mimic a regional lymph node resection procedure. However, due to the large size of the transducer compared to the animal, as shown in figure 1B, an incision large enough to include the transducer would have resulted in severe mutilation of the animal. Verification of this potential using a larger animal model or small patient study would therefore come highly recommended.

Ex vivo, a clear distinction between the PA images of benign and metastatic nodes can be produced and the results show that a staging decision, primarily based on their PA distribution, can be made for all lymph nodes. These data therefore suggest that the SPIO magnetic tracer, Sienna+, may be applied for nodal staging with photoacoustics in an *ex vivo* setting, and as such may be helpful in fast analysis of, for example, the sentinel lymph node. The applicability of this new SPIO magnetic tracer ensures that an *ex vivo* approach is not limited to the availability of a single clinical SPIO magnetic tracer. Histological correlation shows that absence of PA contrast grossly correlates with the presence of metastatic cells in that part of the lymph node which shows that PA mapping is also able to give an indication of the underlying physiological situation.

Because of the almost real-time image acquisition of the system, physiological information can be obtained within minutes after resection which might make this approach very suitable for intra-operative decision making. Quantitative iron measurements confirm the underlying change in particle uptake between the two different types of nodes and show that the iron quantity to volume ratio is especially distinctive. Detected iron quantities are comparable with our previous study in healthy rodents (25) demonstrating that lymphatic drainage is most likely not affected by the primary tumor. Moreover, swelling of the lymph nodes due to immunoreactive responses does not significantly alter the nanoparticle uptake but might be of influence on its concentration.

Overall we can conclude that non-invasive hybrid PA imaging of the popliteal zone can be performed *in vivo* and within a limited time frame (3 minutes). Non-invasive nodal staging on the basis of SPIO distribution however remains challenging due to the limited absorption of the particle deposits and the influence of endogenous chromophores, such as hemoglobin, in the surrounding vasculature. *In toto* imaging shows higher contrast ratios, although a clear distinction cannot be made on the basis of PA signal distribution. Only after resection (*ex vivo*) of the lymph nodes, PA signal distribution allows for a clear distinction between benign and metastatic nodes. Absence of PA response within the nodal volume correlates with the presence of metastatic cell deposits which demonstrates that the distinction is based on physiological alterations. Introduction of the technique on a small scale within the operation theatre might be able to verify whether the use of SPIO particles could be beneficial for intra-operative (sentinel) lymph node staging during a resection.

7.5 References

1. Balch CM, Soong SJ, Gershenwald JE, Thompson JF, Reintgen DS, Cascinelli N, Urist M, McMasters KM, Ross MI, Kirkwood JM, Atkins MB, Thompson JA, Coit DG, Byrd D, Desmond R, Zhang Y, Liu PY, Lyman GH, Morabito A. Prognostic factors analysis of 17,600 melanoma patients: validation of the American Joint Committee on Cancer melanoma staging system. J Clin Oncol 2001; 19(16):3622-3634.
2. Krag DN, Single RM. Breast cancer survival according to number of nodes removed. Ann Surg Oncol 2003; 10(10):1152-1159.
3. Ahuja AT, Ying M. Sonographic evaluation of cervical lymph nodes. AJR Am J Roentgenol 2005; 184(5):1691-1699.
4. Murata Y, Ohta M, Hayashi K, Ide H, Takasaki K. Preoperative evaluation of lymph node metastasis in esophageal cancer. Ann Thorac Cardiovasc Surg 2003; 9(2):88-92.
5. Einstein DM, Singer AA, Chilcote WA, Desai RK. Abdominal lymphadenopathy: spectrum of CT findings. Radiographics 1991; 11(3):457-472.
6. Gross BH, Glazer GM, Orringer MB, Spizarny DL, Flint A. Bronchogenic carcinoma metastatic to normal-sized lymph nodes: frequency and significance. Radiology 1988; 166(1 Pt 1):71-74.
7. Kayser K, Bach S, Bulzebruck H, Vogt-Moykopf I, Probst G. Site, size, and tumour involvement of resected extrapulmonary lymph nodes in lung cancer. J Surg Oncol 1990; 43(1):45-49.
8. McLoud TC, Bourgouin PM, Greenberg RW, Kosiuk JP, Templeton PA, Shepard JA, Moore EH, Wain JC, Mathisen DJ, Grillo HC. Bronchogenic carcinoma: analysis of staging in the mediastinum with CT by correlative lymph node mapping and sampling. Radiology 1992; 182(2):319-323.
9. Weissleder R, Elizondo G, Josephson L, Compton CC, Fretz CJ, Stark DD, Ferrucci JT. Experimental lymph node metastases: enhanced detection with MR lymphography. Radiology 1989; 171(3):835-839.
10. Bellin MF, Roy C, Kinkel K, Thoumas D, Zaim S, Vanel D, Tuchmann C, Richard F, Jacqmin D, Delcourt A, Challier E, Lebret T, Cluzel P. Lymph node metastases: safety and effectiveness of MR imaging with ultrasmall superparamagnetic iron oxide particles--initial clinical experience. Radiology 1998; 207(3):799-808.
11. Will O, Purkayastha S, Chan C, Athanasiou T, Darzi AW, Gedroyc W, Tekkis PP. Diagnostic precision of nanoparticle-enhanced MRI for lymph-node metastases: a meta-analysis. Lancet Oncol 2006; 7(1):52-60.
12. Aeppli G, Pankhurst Q. Launch of the London Centre for Nanotechnology. Nanomedicine (Lond) 2006; 1(4):393-398.
13. Kimura K, Tanigawa N, Matsuki M, Nohara T, Iwamoto M, Sumiyoshi K, Tanaka S, Takahashi Y, Narumi Y. High-resolution MR lymphography using ultrasmall superparamagnetic iron oxide (USPIO) in the evaluation of axillary lymph nodes in patients with early stage breast cancer: preliminary results. Breast Cancer 2010; 17(4):241-246.
14. Schlegel A, Alvarado SF, Wachter P. Optical-Properties of Magnetite (Fe3o4). J Phys C Solid State 1979; 12(6):1157-1164.
15. Wang LV, Hu S. Photoacoustic tomography: in vivo imaging from organelles to organs. Science 2012; 335(6075):1458-1462.

16. Razansky D, Deliolanis NC, Vinegoni C, Ntziachristos V. Deep tissue optical and optoacoustic molecular imaging technologies for pre-clinical research and drug discovery. Curr Pharm Biotechnol 2012; 13(4):504-522.
17. Beard P. Biomedical photoacoustic imaging. Interface Focus 2011; 1(4):602-631.
18. Ermilov SA, Khamapirad T, Conjusteau A, Leonard MH, Lacewell R, Mehta K, Miller T, Oraevsky AA. Laser optoacoustic imaging system for detection of breast cancer. J Biomed Opt 2009; 14(2):024007.
19. Kruger RA, Lam RB, Reinecke DR, Del Rio SP, Doyle RP. Photoacoustic angiography of the breast. Med Phys 2010; 37(11):6096-6100.
20. Heijblom M, Piras D, Xia W, van Hespen JC, Klaase JM, van den Engh FM, van Leeuwen TG, Steenbergen W, Manohar S. Visualizing breast cancer using the Twente photoacoustic mammoscope: What do we learn from twelve new patient measurements? Opt Express 2012; 20(11):11582-11597.
21. Jose J, Grootendorst DJ, Vijn TW, Wouters M, van Boven H, van Leeuwen TG, Steenbergen W, Ruers TJ, Manohar S. Initial results of imaging melanoma metastasis in resected human lymph nodes using photoacoustic computed tomography. J Biomed Opt 2011; 16(9):096021.
22. Grootendorst DJ, Jose J, Wouters MW, van Boven H, Van der Hage J, Van Leeuwen TG, Steenbergen W, Manohar S, Ruers TJ. First experiences of photoacoustic imaging for detection of melanoma metastases in resected human lymph nodes. Lasers Surg Med 2012.
23. Laufer J, Johnson P, Zhang E, Treeby B, Cox B, Pedley B, Beard P. In vivo preclinical photoacoustic imaging of tumor vasculature development and therapy. J Biomed Opt 2012; 17(5):056016.
24. Xi L, Grobmyer SR, Wu L, Chen R, Zhou G, Gutwein LG, Sun J, Liao W, Zhou Q, Xie H, Jiang H. Evaluation of breast tumor margins in vivo with intraoperative photoacoustic imaging. Opt Express 2012; 20(8):8726-8731.
25. Grootendorst DJ, Jose J, Fratila RM, Visscher M, Velders AH, Ten Haken B, Van Leeuwen TG, Steenbergen W, Manohar S, Ruers TJ. Evaluation of superparamagnetic iron oxide nanoparticles (Endorem(R)) as a photoacoustic contrast agent for intra-operative nodal staging. Contrast Media Mol Imaging 2013; 8(1):83-91.
26. Xi L, Grobmyer SR, Zhou G, Qian W, Yang L, Jiang H. Molecular photoacoustic tomography of breast cancer using receptor targeted magnetic iron oxide nanoparticles as contrast agents. J Biophotonics 2012.

CHAPTER 8

CONCLUSIONS AND OUTLOOK

The previous chapters provide an overview of our scientific achievements which were aimed at exploring the applicability of photoacoustic imaging for the staging of lymph nodes during surgical procedures. We aimed to look into the feasibility of this approach by detecting metastases in clinical samples using endogenous chromophores while also exploring the possible potential of clinical exogeneous contrast enhancers in animal models.

With respect to the results of our scientific work on human lymph node samples from melanoma patients we can conclude that the detection of smaller metastases inside medium sized resected nodes can be done with photoacoustic (PA) imaging. We show that an increase in photoacoustic response within these nodes correlates to the presence of melanin-rich metastatic deposits and verify that PA imaging is capable of providing a map of the absorbing components within these nodes (Chapter 2). Furthermore, by applying anatomical criteria a distinction between benign and metastatic nodes can be obtained (Chapter 3). The results also show that this can be done within a limited time frame and without any physical damage to the lymph node which makes the approach applicable during surgical interventions. The technical difficulty of the current embodiment is centered around its current accuracy with respect to metastases detection. The detection of hypomelanotic or amelanotic lesions could, in theory, be further optimized by superparamagnetic iron oxide (SPIO) nanoparticle addition, however this would not remove the limitation of being unable to resolve the different endogenous absorbers. As proposed in Chapter 3, we suggest to technically resolve this limitation by making use of the spectroscopic possibilities of photoacoustics. By including the option of multiple wavelength excitation into a future PA setup a depiction of the absorption characteristics of each absorber can be obtained, enabling a distinction on physiological properties. Especially, the highly characteristic absorption spectrum of hemoglobin in the near infra-red region, might make such a distinction method highly sensitive. One has to keep in mind however that the inclusion of a fluence compensating algorithm, together with a

highly stable laser have to be considered to make these measurements quantitative and therefore more reliable. All in all, this might require a prolonged cooperation between biomedical PA researchers and algorithmic specialists to come up with a tailor-made imager, optimized for lymph node metastases detection. At the moment, we aim to publish the results of our first attempt towards the use of such a PA spectroscopic approach for the staging of human lymph nodes.

With respect to our pre-clinical results on the use of SPIO nanoparticles, our research provides insight into the clinical applicability and sensitivity of these particles for the detection of non-absorbing lymph node metastases. We demonstrate that SPIOs contain a clearly detectable PA response within excised lymph nodes after *in vivo* transport from the injection site and show that their distribution within lymph nodes can be accurately mapped (Chapter 4). Additionally, we tested their potential inside an animal model and demonstrated that an *ex vivo* distinction between benign and metastatic nodes can be made on the basis of the PA contrast distribution (Chapter 5). These results suggest that such a distinction can most likely also be made for human lymph nodes and together with the fact that SPIO dispersions have been found safe to use within clinical practice, a rapid translation of this pre-clinical approach could be performed. Possible future improvements can be made with respect to the sensitivity of the technique by coupling the dextran coated particles with tumor specific antigens, a concept most recently explored by Xi *et al*. As discussed in Chapter 6, we stress that all these applications might also be pursued with the help of biologically safe carbon nanoparticles dispersions.

In order to look into the possibilities of expanding the scope to non-invasive nodal staging, we also attempted to stage SPIO enhanced popliteal lymph nodes *in vivo* using a handheld linear array PA modality (Chapter 7). These results demonstrate that a fused combination of PA and ultrasound provides valuable extra information on the expected source of the PA signals which to our understanding is vital to perform *in vivo* staging. With this in mind we therefore stress the importance of including such a hybrid imaging option, once non-invasive nodal staging is attempted with or without exogeneous agents in the possible near-future.

The additional insights gained from these experiments, learn us that presence of endogeneous absorbers limits the *in vivo* staging potential of the SPIO nanoparticles. In order to circumnavigate these limitations for future appliances, we again expect that PA spectroscopy might prove to be a valuable addition which could identify the SPIO related PA signal and specifically extract them. This would however also require the implementation of optimized soft- and hardware.

Finally, the application of different imaging geometries shows that both a tomographic or hand held linear array PA approach could be valuable depending on the use of the imager and the surgical procedure it has to improve. For assessment of excised sentinel lymph

nodes a tomographic approach could be more useful, providing a homogeneous illumination inside a light-tight modality. For *in vivo* nodal assessment during for example a lymphadenectomy a hand held linear array approach could be more beneficial due to its hand-held capabilities and limited size.

All in all, the clinical and pre-clinical feasibility evaluation of PA nodal staging in this thesis brings us a bit closer to the possible eventual implementation of photoacoustics in a clinical setting, as a non-ionizing, safe and real-time imaging solution. The near-future will most likely tell us in what area these advantages can be most optimally applied to serve the need of the medical profession and the patient.

ACKNOWLEDGEMENTS

Now I have come to the end of my thesis I would like to thank a large number of people from both the NKI and the MIRA institute for their help during the realization of my research. Not only could I not have performed my experiments without their contributions but their uplifting feedback and energy kept me on my feet during the ups and downs of the entire process.

First and most importantly, I would like to thank my promoter Prof. Ruers for giving me the opportunity to continue my Masters research under his supervision and believing in a successful outcome during the entire process. Although the available research time was limited, your supervision and clinical feedback enabled me set up and perform my experiments both within the NKI and the MIRA institute within the available time-span while maintaining its academic content. For the same reasons my gratitude goes to Dr. Manohar, who also gave up so much of his valuable time to go over my journal submissions and helped me get to the bottom of my acquired data. The fact that your door was always open helped me enormously!

I thank my graduation committee members for their time and effort reviewing this thesis and Prof. Steenbergen for allowing me to work within his group and providing me with valuable comments during my writing. Also, a special thanks to dr. Jose for helping me get experience with his sophisticated photoacoustic setups both within the BMPI group as at the VisualSonics labs in Amsterdam. All additional employees of VisualSonics, including Katrin and Dieter, are of course also entitled to my thanks, especially for helping me set up and plan the all animal experiments in their lab.

Naturally, a lot of thanks to all my colleagues at the BMPI group for their feedback and laughs during work time which put me back on my feet if some of my experiments failed. With respect to setting up and performing my animal experiments my thanks go to Prof. Van Wezel and Ms. Klomphaar. I thank dr. Velders and dr. Van Haken for facilitating our magnetic experiments and dr. Fratila and dr. Visscher for helping me perform them. Also. many thanks to Endomagnetics for supplying us with their Sienna+ dispersion. In addition, a special thanks to the master students Niels and Sanne for working with me on the different topics and helping me acquire a lot of valuable samples and insights.

With regard to the staff of the NKI-AVL my thanks especially goes to all members of the surgical oncology department, dr. Wouters, dr. Van der Hage and dr. Nieweg for their help in obtaining all the human lymph node samples. In addition, special thanks to dr. Van Boven for her time and expertise in reviewing all samples histologically. Next to all clinical

personnel Í would like to thank dr. Rottenberg for his time in explaining the histological findings of our animal experiments.

Of course, a lot of thanks goes to my dad, brothers and family for providing me with all the mental support a PhD could need. Special thanks to my father for providing many useful medical insights and Maarten for continuously overwhelming me with information and questions about his clinical lymphatic trial at the MST. It really helped me getting my goals right while keeping the medical (dis)advantages of our technique in to mind.

Finally, I want to express my gratitude to my friends and fraternity for laughing my difficulties away by continuously telling me my PhD was only an extension of my student life and real-life problems would only come with a normal job. Now that I have arrived at that point I hope you will continue to support me!

If I forgot to mention anyone who feels he or she should have been mentioned, please forgive me for doing so and just blame it on my forgetfulness and the limited time available for completing my thesis. This leaves me to finish with the small, although famous Latin saying: “Dixi”!

ABOUT THE AUTHOR

Diederik Johannes Grootendorst was born on the 1ste of October 1985 in Amsterdam, The Netherlands. He obtained his Master of Science degree in Technical Medicine from the University of Twente in 2011. His specialization was in the area of intra-operative imaging. His master thesis work was done at the Biomedical Photonic Imaging (BMPI) group of the University of Twente in combination with the surgical oncology department of the Netherlands Cancer Institute – Antoni van Leeuwenhoek (NKI-AVL) where he investigated the use of photoacoustics for intra-operative nodal staging.

From October 2011 until March 2013 he performed research towards his PhD thesis at both the BMPI group as the NKI-AVL under the supervision of Prof. Dr. T.J.M. Ruers and Dr. Manohar. During his research he investigated the clinical applicability of photoacoustic imaging with respect to fast intra-operative nodal staging for various malignancies.

LIST OF PUBLICATIONS

JOURNAL ARTICLES

1. **D.J. Grootendorst**, R.M. Fratila, M. Visscher, B. Ten Haken, R.J. Van Wezel, S. Rottenberg, W. Steenbergen, S. Manohar, T.J.M. Ruers, Intra-operative ex vivo photoacoustic nodal staging in a rat model using a clinical superparamagnetic iron oxide nanoparticle dispersion, J Biophotonics, [Ahead of print] (2013)
2. **D.J. Grootendorst**, J. Jose, R.M. Fratila, M. Visscher, A.H. Velders, B. Ten Haken, T.G. Van Leeuwen, W. Steenbergen, S. Manohar, T.J.M. Ruers, Evaluation of superparamagnetic iron oxide nanoparticles (Endorem(®)) as a photoacoustic contrast agent for intra-operative nodal staging. Contrast Media Mol Imaging 8(1), pp 83-91 (2013).
3. **D.J. Grootendorst**, J. Jose, M.W. Wouters, H. Van Boven, J. Van der Hage, T.G. Van Leeuwen, W. Steenbergen, S. Manohar, T.J.M. Ruers, First experiences of photoacoustic imaging for detection of melanoma metastases in resected human lymph nodes. Lasers Surg Med 44(7), pp 541-549 (2012)
4. J. Jose, **D.J. Grootendorst**, T.W. Vijn, M. Wouters, H. Van Boven, T.G. Van Leeuwen, W. Steenbergen, T.J.M. Ruers, S. Manohar, Initial results of imaging melanoma metastasis in resected human lymph nodes using photoacoustic computed tomography, J Biomed Opt 16(9), pp 096021 (2011)

PROCEEDING ARTICLES

1. **D.J. Grootendorst**, J. Jose, P. Van der Jagt, W. Van der Weg, K. Nagel, M.W. Wouters, H. Van Boven, T.G. Van Leeuwen, W. Steenbergen, T.J.M. Ruers, S. Manohar, Initial experiences in the photoacoustic detection of melanoma metastases in resected lymph nodes, Photons Plus Ultrasound: Imaging and Sensing, pp 7899, (2011)
2. **D.J. Grootendorst**, Raluca .M. Fratila, Martijn Visscher, Bennie Ten Haken, Richard van Wezel, Wiendelt Steenbergen, Srirang Manohar and Theo J. M. Ruers, Photoacoustic intra-operative nodal staging using clinically approved superparamagnetic iron oxide nanoparticles, Photonics West, Photons Plus Ultrasound: Imaging and Sensing (2013)

CONFERENCE CONTRIBUTIONS

1. G. Langhout, **D.J. Grootendorst**, D. Fuchs, J. Jose, W. Steenbergen, S. Manohar, T.J.M. Ruers, Demarcation of Melanoma Metastasis in Photoacoustic Spectral Imaging of Human Lymph Nodes. European Journal of Surgical Oncology (EJSO) 38(9), 862-863 (2012).
2. **D.J. Grootendorst**, R.M. Fratila, M. Visscher, B. Ten Haken, A.H. Velders, R. Van Wezel, W. Steenbergen, S. Manohar, T.J.M. Ruers, Photoacoustic Nodal Metastases Detection in a Rat Model Using a Clinical Superparamagnetic Iron

Oxide Nanoparticle Dispersion. European Journal of Surgical Oncology (EJSO) 38(9), 844-845 (2012).

3. **D.J. Grootendorst**, R.M. Fratila, M. Visscher, B. Ten Haken, A.H. Velders, R. Van Wezel, W. Steenbergen, S. Manohar, T.J.M. Ruers, Photoacoustic Nodal Metastases Detection in a Rat Model Using a Clinical Superparamagnetic Iron Oxide Nanoparticle Dispersion. Nederlandse Vereniging voor Technische Geneeskunde Congres, Arnhem, October (2012).
4. **D.J. Grootendorst**, R.M. Fratila, M. Visscher, A.H. Velders, B. Ten Haken, W. Steenbergen, S. Manohar, T.J.M. Ruers, Photoacoustic Metastases Detection using Clinically Approved SPIO dispersions, Optical Society of America (OSA), Miami, United States (2012)
5. J. Jose, T. W. Vijn, **D. J. Grootendorst**, W. Steenbergen, T. G. van Leeuwen, T. J. M. Ruers and S. Manohar, Imaging melanoma metastases in resected human lymph nodes using photoacoustic computed tomography, Fotonica Evenement , Nieuwegein, The Netherlands (2011)